

# Laser Powder Bed Fusion of a New Inconel Superalloy Via *In-Situ* *Alloying*



Master Degree in Materials Engineering

Politecnico di Torino

DISAT

Italy

*Dr.* Abdollah Saboori  
*Dr.* Giulio Marchese

Abbà Erik  
s255112

Academic Year 2020/2021



## Abstract

Laser Powder Bed Fusion (L-PBF) technology was used to manufacture a new alloy by means of the new approach of in-situ alloying. Rather than use a pre-alloyed powder, the study involved the creation of a blend of Ti and Inconel 718 powders mixed in 1:99 ratio (1%<sub>wt</sub> Ti and 99%<sub>wt</sub> Inconel 718). The aim of the study was first, to increase the mechanical properties of the new alloy compared to the reference Inconel 718 in its range of application temperatures (up to 600°C). Second, to study the feasibility of the situ-alloying as an alternative method to achieve desired alloy compositions, contrary to the more common use of pre-alloyed powders. The former relied on the Ti tendency to enhance  $\gamma'$  precipitation, while the latter exploited the metallographic characterization as a powerful means to study how differences in chemical composition, mass fraction, and size distribution of the powders affected the outcomes of the printing process. After the first step of printing parameters optimization, a metallographic characterization was carried out on both pure Inconel 718 and the in-situ alloyed version, Inconel 718 + Ti. Two different heat-treated conditions were analysed in addition to the as-built (ab) condition - solution treated (ST), and solution treated and double aged (SDAG). The thermal treatment followed the AMS 5667, a common process usually performed on Inconel 718. Investigations on the microstructure were carried out by scanning electron microscopy (SEM) and optical microscopy (OM) along with microhardness measurements. As a result, Ti-segregations were discovered in Inconel 718 + Ti in both the as-built and heat-treated conditions. These segregations caused a significant effect on the microstructure evolution under heat treatment. It caused the precipitation of (Nb,Ti)-rich needle-like secondary phases, mainly in the regions with the higher concentration gradient. The latter caused the microhardness of the new alloy to be higher than Inconel 718 in the ST-condition, while lower when in the SDAG-condition. Through a cross-analysis of morphology, mechanical data, and literature review these needle-like precipitates seemed to be to the  $\eta$ -phase. However, by and large, the in-situ alloying did not affect the weldability of the powder, allowing to achieve densities comparable to the reference Inconel 718. Although this process still requires further studies, it seems a significantly faster and cost-effective alternative to the conventional pre-alloyed routes.

**Keywords:** *Additive Manufacturing, Laser Powder Bed Fusion, Inconel 718, In-Situ Alloying, Heat Treatments*

## Acknowledgements

Before starting this thesis, I would like to spend some words on the people who have helped me throughout my journey.

First and foremost, all my gratitude goes to my supervisors Abdollah Saboori and Giulio Marchese. Your support, motivation and guidance steered me through this research allowing me to sharpen my thinking. Not only has this brought my dissertation to a higher level but it has paved the way for my upcoming challenges.

I am also thankful to my tutor and friend Francesco Viola who helped me during all the analyses and was always committed to making the most of my work.

A special thank goes to my family, my parents Mariano and Antonella, my sister Marika, my grandma Elena, my uncles Arturo and Riccardo, and my aunts Bruna and Lucia. You have been a support all these years and you have provided me with everything I needed to reach goals I did not even know to be able to reach. In particular in the last year, despite many hardships, you have always backed me up without hesitation.

I cannot help but thank my international family that I met during my Erasmus experience. Witty, cheerful, and unique people I have been in contact with ever since. I would like to thank in a special way Pablo and Clara. Two fantastic and invaluable friends who have been a part of my life for the past year and I am sure they will be in it for a long time to come. By spending time together cooking, studying, and travelling you have provided me with so much strength and hope that I will always be grateful to have met you.

Furthermore, I am extremely grateful to Ludovico, Chiara, Manuel, Sara, and Serena whose undeniable support and friendship throughout my career at the Politecnico of Turin are part of what I have accomplished and who I am.

Special mention to Maurizio, Pietro, Cedu, Alberto e Tiago, my travel companions with whom I shared unforgettable experiences. Thank you for always supporting and believing in me. Your endless trust makes every challenge so much easier.

I cannot forget to thank Giulia. You are a special person, we have shared good and bad moments and nothing would have been possible without you.

I am also grateful to Giorda, Matthieu and Stefano, my amazing flatmates with whom I spent meaningful and fun moments, stocking up with memories and useful skills.

To conclude, I would like to thank one of my earliest friends, Domenico, who has been a constant presence since my childhood and on whom I can always count.

My Deepest Thanks!

# Contents

<b>Summary</b>	<b>i</b>
<b>List of Abbreviations</b>	<b>xviii</b>
<b>List of Figures</b>	<b>xxii</b>
<b>List of Tables</b>	<b>xxiii</b>
<b>1 Introduction</b>	<b>1</b>
1.1 Background . . . . .	1
1.2 Research Aims . . . . .	1
1.3 Structure of the Thesis . . . . .	2
<b>2 Additive manufacturing</b>	<b>3</b>
2.1 <i>Historical Development</i> . . . . .	3
2.2 <i>Concept</i> . . . . .	5
2.3 <i>Laser Powder Bed Fusion</i> . . . . .	8
2.3.1 Powder Feedstock . . . . .	9
2.3.2 Parameters . . . . .	10
2.3.3 Protective Gas . . . . .	14
2.3.4 Scanning strategy . . . . .	14
2.3.5 Possible Drawbacks . . . . .	16
<b>3 Ni-base superalloys for 3D printing</b>	<b>22</b>
3.1 <i>Inconel 718</i> . . . . .	24
3.1.1 Gamma Prime, Gamma Double Prime, and Delta Phase . . . . .	28
3.1.2 Laves Phases . . . . .	30
3.1.3 Eta Phase . . . . .	31
<b>4 In-situ Alloying</b>	<b>33</b>
4.1 Inconel 718 Development . . . . .	35
4.1.1 Allvac 718Plus . . . . .	37
4.1.2 VDM 780 Premium . . . . .	41
4.1.3 K4750 . . . . .	45
4.1.4 Inconel 718 + Ti . . . . .	48
<b>5 Material and Methodology</b>	<b>49</b>
5.1 L-PBF . . . . .	50
5.2 Heat Treatments . . . . .	52
5.3 Metallographic Preparation . . . . .	53
5.4 Optical Microscopy . . . . .	53
5.5 Scanning Electron Microscopy . . . . .	54
5.5.1 Energy Dispersive Spectroscopy . . . . .	55
5.6 ImageJ and Archimede's Density . . . . .	56
5.7 Hardness Measurements . . . . .	57
5.7.1 Vickers Microhardness . . . . .	57
5.7.2 Brinell Hardness . . . . .	58

<b>6</b>	<b><i>Result Discussion</i></b>	<b>59</b>
6.1	<i>Job 1</i> . . . . .	59
6.2	<i>Job 2</i> . . . . .	63
6.3	<i>Job 3</i> . . . . .	66
6.3.1	As-Built Condition . . . . .	66
6.3.2	Solution Heat Treated Condition . . . . .	70
6.3.3	Double Aged Condition . . . . .	74
6.3.4	Microhardness . . . . .	78
<b>7</b>	<b>Conclusion</b>	<b>83</b>
7.1	Results and Highlights . . . . .	83
7.2	Future Works . . . . .	84
	<b>References</b>	<b>86</b>

## Summary

This section provides the summary of the dissertation in the Italian language as required by the Materials Engineering degree program. In the following sections, statements will refer to images and tables. The latter are always to be found in the data available in the English-version of the dissertation.

## Introduzione

### Background

La tecnologia *Laser Powder Bed Fusion* (L-PBF) appartiene alle tecniche di fusione a letto di polvere, sottogruppo dei processi di stampa 3D. Essi permettono l'ottenimento di prodotti altamente complessi attraverso l'utilizzo di una tecnica additiva nota come *layer-by-layer*. Il concetto di additive manufacturing (AM) si pone come concetto opposto ai più tradizionali metodi basati sulla rimozione di materiale.

La possibilità di ridurre il peso di un componente attraverso l'utilizzo di strutture complesse senza incidere sulle proprietà meccaniche del prodotto finito, ha permesso un'ampia diffusione delle tecniche L-PBF nel settore dell'aeronautica. Questo, data la loro necessità di avere strutture leggere e capaci di sostenere importanti carichi in condizioni critiche sotto il punto di vista termico e chimico, caratteristiche dei motori aeronautici. Negli anni, le superleghe di nichel si sono rivelate materiali eccellenti per questo tipo di applicazione, arrivando oggi a coprire il 50% del peso totale del motore. In particolare, Inconel 718 possiede il primato di superlega più diffusa. Essa racchiude in se incredibili proprietà meccaniche ad alta temperatura, resistenza a creep, a fatica, resilienza e una notevole saldabilità. Proprietà che ne hanno reso il materiale ideale per l'utilizzo in componenti quali dischi e pale di turbina, così come casings di sezioni del compressore ad alta temperatura. La sua grande saldabilità ne ha permesso un rapido inserimento nel settore dell'additive manufacturing. Qui sta la principale innovazione portata da questo lavoro di ricerca. Tradizionalmente i processi L-PBF si basano su polveri pre-alligate. Questo lavoro è stato invece direzionato sull'ottenimento della composizione chimica desiderata attraverso alligazione in loco attraverso la miscelazione di due polveri, noto come *situ-alloying*. Una volta perfezionata, questa tecnica permetterebbe la produzione di volumi ridotti di polveri, partendo da polveri già in possesso nei singoli centri di ricerca. La possibilità di ottenere la composizione desiderata e la possibilità di evitare l'acquisto di inutili grandi stock di polveri, porterebbe ad un'importante riduzione di costi e tempi richiesti al processo di produzione.

### Obiettivi della Ricerca

Nonostante l'eccellente saldabilità sia la ragione del successo in AM della lega Inconel 718, essa è dovuta alla presenza della fase  $\gamma''$  che ne limita la massima temperatura di applicazione. Essendo comunemente utilizzata in motori aeronautici ad alta temperatura, negli ultimi anni molti ricercatori hanno cercato di limitare la precipitazione di questa fase a favore di maggiori temperature di lavoro e mantenendo inalterate le sue proprietà meccaniche. Mentre sono meno numerosi gli studi relativi

al semplice incremento delle prestazioni meccaniche del Inconel 718, non sono invece presenti studi che verifichino la possibilità di farlo attraverso *situ-alloying*. Lo scopo di questa ricerca era perciò di colmare questo gap investigando il possibile incremento delle proprietà meccaniche di questa lega attraverso l'aggiunta di polveri di titanio al fine di incrementare lo sviluppo della fase  $\gamma'$ . Questo senza alcun interesse ad un possibile incremento della temperatura di applicazione della lega. Al contrario, particolare attenzione è stata volta allo studio degli effetti che le polveri di titanio come - variazioni nella saldabilità, omogeneità della lega e possibili variazioni microstrutturali. La prima fase della ricerca ha richiesto la definizione di opportuni parametri su misura. Necessari data la diversa interazione laser-materiale dovuta all'intrinseca inomogeneità di un blend di polveri. Dopo l'ottimizzazione dei parametri di stampa il lavoro si è concentrato sulla caratterizzazione metallografica di tre differenti condizioni di trattamento termico - as-built, solubilizzata, solubilizzata e invecchiata. Questo al fine di stabilire importanti inter-relazioni del tipo materiale-processo-proprietà meccaniche.

## Additive Manufacturing

Secondo la definizione ASTM (Standard, 2012), additive manufacturing è...

*”un processo di unione di materiali per l’ottenimento di componenti a partire da un modello 3D, solitamente strato dopo strato, in contrapposizione alle tecnologie di produzione sottrattiva”.*

Tutte le tecnologie di additive hanno infatti un comune punto di partenza quale un modello CAD o una scultura digitale. Tale modello deve essere convertito in formato .stl che ne assicura la lettura da parte degli hardware di stampa. In aggiunta, rende possibile l’approssimazione della superficie del modello attraverso l’utilizzo di semplici figure geometriche (triangoli) non sovrapposte. Questo metodo non favorisce solo un’efficiente approssimazione della superficie ma permette anche la successiva divisione del componente in strati, noti come *”layers”* (Antero, 2018; Chakravorty, 2020).

Mentre le tecnologie di stampa 3D polimerica sono ormai ampiamente diffuse e poco costose, il settore dell’additive manufacturing dei metalli ancora rappresenta una nicchia. L’elevato costo e la minore precisione ne hanno reso inizialmente comune l’utilizzo mirato a prototipi. Ad oggi, la maggiore affidabilità ne ha però permesso lo sviluppo in settori più di avanguardia come il biomedico e l’aeronautico, dove viene utilizzata per la produzione di *near-net-shape components*, adatti ad operare in macchina. Il particolare vantaggio di questa tecnologia sta nell’intensa riduzione di scarti di processo, ridotti per la maggior parte alle sole parti di sostegno. Quest’ultime sono necessarie al fine di stampare superfici molto inclinate (*overhanging surfaces*) altrimenti soggette a possibile rottura o generazione di difetti. Inoltre, la loro presenza ha una forte influenza sui flussi termici di raffreddamento delle pozze di fusione (*melt pools*) fungendo da *”pozze termiche”* (Calignano, 2014).

Le tecnologie di stampa dei metalli sono diverse. Le più comuni tuttavia appartengono a due famiglie - tecniche di deposizione e a letto di polvere. Alla prima appartengono la deposizione laser (LMD) e il Wire and Arc Additive Manufacturing (WAAM). Le principali tecnologie a letto di polvere sono invece la tecnica di fusione a fascio di elettroni (Electron Beam Melting, EBM) e la fusione selettiva a fascio laser (Selective Laser Melting, SLM anche nota come L-PBF) (Uriondo, Esperon-Miguez, & Perinpanayagam, 2015).

### Laser Powder Bed Fusion

*Laser Powder Bed Fusion*, nota anche come *Selective Laser Melting*, è una tecnologia di stampa 3D che permette l’ottenimento di complesse strutture attraverso l’utilizzo di strati successivi di polvere. Senza tener conto di possibili cariche inserite nella polvere, quest’ultima è solitamente caratterizzata da una geometria sferica per assicurarne una elevata *flowability*. Il processo fa uso di un fascio laser ad alta energia il quale, seguendo un modello CAD, scalda la polvere in modo selettivo fino a raggiungerne il punto di fusione. Il processo si basa sulla stesura di successivi strati di polvere al di sopra ad una piattaforma, nota come *building platform*. Quest’ultima può essere scaldata fino a qualche centinaia di gradi al fine di ridurre le cinetiche di raffreddamento coinvolte nel processo (solitamente  $10^6\text{K/s}$ ) (Sun, Brandt, & Easton, 2017). La stesura delle polveri avviene

attraverso l'utilizzo di un rullo contro-rotante o un sistema di rastrellamento che permettono di livellare la polvere con spessori nell'ordine di decine di  $\mu m$ . Un'altro strato verrà poi depositato dopo che il laser avrà scansionato il precedente, da qui la nomenclatura di tecnologia *layer-by-layer*.

L-PBF è un processo altamente complesso, che coinvolge un numero elevato di parametri. I principali sono quattro - potenza del laser (P), velocità di scansione (v), distanza di hatching (h) e spessore del layer (t). Quest'ultimi sono solitamente relazionati sotto un generico parametro detto "Densità Volumetrica di Energia" (VED) espressa come rapporto tra la potenza e il prodotto dei restanti tre parametri, **Eq.2**. Tale valore da informazioni per quanto riguarda la densità di energia fornita al letto di polvere. Questa informazione è infatti molto importante dato che i parametri hanno una forte influenza sulle prestazioni del componente stampato. Tipologia di *feed*, scelta del tipo e portata di gas protettivo nella camera di stampa e strategia di scansione permettono di influire su proprietà fisico-meccaniche del materiale, come:

- Orientamento dei grani cristallini;
- Texture cristallina;
- Presenza di fasi rinforzanti;
- Presenza di fasi deleterie;
- Distribuzione granulometrica dei grani;
- Grado di porosità.

In particolare, le alte cinetiche di raffreddamento causano lo sviluppo di una microstruttura caratteristica nelle superleghe di nichel. Tipico è lo sviluppo di una struttura dendritico/cellulare con taglia spesso inferiore al  $\mu m$ . Tali cinetiche di riscaldamento e raffreddamento sviluppano condizioni di sovra-riscaldamento e sotto-raffreddamento che favoriscono la nucleazione a scapito della crescita del grano cristallino. Di conseguenza il risultato è una microstruttura molto fine e orientata lungo la direzione di processo, o *building direction* (asse z). Questo è dovuto al fatto che i grani cristallini si dispongono lungo le linee di maggiore flusso termico, le quali sono orientate in tale direzione causando così lo sviluppo di una microstruttura direzionale (Sun et al., 2017).

L'alto numero di variabili porta inevitabilmente allo sviluppo di condizioni non ideali alla stampa. Di conseguenza il processo può essere colpito da diverse problematiche che, in modo più o meno intenso, alterano le proprietà meccaniche del componente finale. Condizioni quali balling, keyholing, lack of fusion sono le più frequenti.

Se viene fornito il livello di energia ideale alla polvere per arrivare a fusione, si parla di *conduction-mode*. Al contrario, quando l'energia non è sufficiente si parla di *lack-of-fusion*, fenomeno che genera porosità di forma irregolare con taglia di alcune decine di  $\mu m$ . Se la densità di energia è troppo alta si attiva invece il *keyhole-mode*. In tal caso, l'energia fornita è tale da causare l'evaporazione del metallo causando la generazione di plasma. Quest'ultimo incrementa l'assorbimento dell'energia fornita dal laser favorendo l'ulteriore penetrazione del laser nel materiale. Una volta che il laser lascia tale zona, l'incompleto collasso delle cavità generate dal plasma, lascia nel materiale piccole porosità di forma sferica e alcuni micron di diametro. Tali porosità

può talvolta essere confusa con l'inglobamento nella pozza di fusione di sacche di gas protettivo, o porosità derivata direttamente dal feedstock del processo.

Il *balling* è invece solitamente associato ad alte velocità di scansione e/o bassi valori di potenza del laser. In entrambi i casi sono coinvolti bassi valori di VED. Nonostante molti aspetti giochino un ruolo nel suo sviluppo, il *balling* è più spesso associato ad instabilità della pozza di fusione. L'alta velocità di scansione genera il restringimento della pozza di fusione dovuto alla riduzione dell'energia libera del sistema. Quando tale processo non permette un'ulteriore riduzione di energia libera, la pozza di fusione tende a dividersi in simil-sfere, geometria associata ad inferiore energia superficiale. Il *balling* solitamente causa sviluppo di rugosità superficiale e possibile generazione di porosità tra le particelle sferiche generate. Tale fenomeno è dovuto al fatto che la generata irregolarità superficiale ostacola un'omogenea stesura del successivo strato di polvere.

Forse il fenomeno più comune è lo sviluppo di una struttura anisotropica. Nella condizione as-built, è infatti tipico avere differenti proprietà meccaniche. Principalmente, si hanno variazioni in UTS, resistenza allo snervamento e duttilità. Solitamente, carico di snervamento e UTS sono maggiori lungo la direzione perpendicolare alla *building direction*. Al contrario, la duttilità è solitamente maggiore lungo l'asse verticale al piano di costruzione. Questo comportamento può essere associato al *texturing* cristallino. Essendo strutture FCC (Cubico Facce Centrate), le superleghe di nichel tendono a orientare i piani cristallini lungo direzioni parallele a  $\langle 100 \rangle$ . Tuttavia, in fusione della tecnica di scansione, tale fenomeno può essere ridotto fino a quasi eliminarlo. La letteratura dimostra però che tale anisotropia si verifica in ambo i casi, con o senza la presenza di particolari orientamenti preferenziali dei piani cristallini. Diversi studi confermano infatti che tale fenomeno è dovuto allo sviluppo di stress interni al materiale, diversi in funzione della direzione considerata. Quando si genera una pozza di fusione, il materiale solidificando tende a contrarre in tutte le direzioni. Essendo un processo che si sviluppa verticalmente tale fenomeno non è vincolato lungo l'asse z mentre lo è nel piano parallelo alla *building platform*. Questi vincoli si traducono nella generazione di stress residui di tensione maggiori nella direzione parallela al piano di stampa. Tali discrepanze nei valori di tensioni residue causano l'anisotropia delle proprietà meccaniche (Deng, Peng, Brodin, & Moverare, 2018).

## Superleghe Base Ni per Applicazioni in AM

Le superleghe di nichel sono materiali che racchiudono in essi un'eccezionale combinazione di resistenza alla corrosione, tenacità e resistenza meccanica ad alta temperatura. Caratteristiche essenziali per quanto riguarda applicazioni in turbine ad alta pressione (HPT) o all'interno di motori di razzi. In questi settori, questi materiali sono stati usati per dischi, blisk, palette di turbina, condotti criogenici e molte altri componenti i quali devo sottostare condizioni estreme in ambienti molto spesso corrosivi o ossidanti.

Il difetto di queste leghe è il loro peso, hanno infatti una densità tra gli 8 g/cm<sup>3</sup> e i 9 g/cm<sup>3</sup> (Perrut, Caron, Thomas, & Couret, 2018). L'additive manufacturing permette l'ottenimento di geometrie molto complesse come sezioni con pareti sottili, difficili o impossibili da ottenere attraverso le tecnologie più tradizionali. Quest'ultime hanno infatti forti difficoltà a lavorare questi materiali date la bassa conducibilità termica loro caratteristica.

Requisito fondamentale per l'utilizzo in additive manufacturing di una lega è la sua saldabilità. Motivo per cui, ad oggi poche superleghe di nichel sono fruibili per stampaggio 3D. Le principali sono Inconel 718, Waspalloy, Inconel 625, Hastelloy-X e CM 247LC. Sono quattro in particolare gli elementi che influiscono su questa proprietà, Al, Ti, Cr, Co (Henderson, Arrell, Larsson, Heobel, & Marchant, 2004; Catchpole-Smith et al., 2017). Da qui nasce la loro distinzione in funzione della saldabilità, come espresso in **Fig.9** (Attallah, Jennings, Wang, & Carter, 2016). Leghe saldabili (Readily Weldable) e abbastanza saldabili (Fairly Weldable) sono già ampiamente diffuse in AM. Le leghe difficili da saldare (Difficult to Weld) sono invece per lo più in via di sviluppo. Quest'ultime soffrono delle problematiche tipiche delle "non saldabili". Aspetti comuni alla più convenzionale saldatura come - hot tearing, ductility dip cracking e liquation cracking. In generale, il fenomeno però più comune in AM è lo Strain Age Cracking (SAC). Questo fenomeno si basa sullo sviluppo nelle zone termicamente alterate (HAZ, Heat Affected Zones) di fasi rinforzanti che irrigidiscono il materiale a scapito della sua tenacità, sottoponendolo a rischio di cricatura. Ogni qualvolta il laser scansiona un nuovo layer, allo stesso tempo riscalda ad alte temperature gli strati successivi. L'energia così fornita può favorire la generazione di fasi indurenti, l'accumulo di stress interni e, nei casi più critici, la rottura del componente in stampa (Carter, Attallah, & Reed, 2012; Bourell et al., 2017).

### Inconel 718

Inconel 718 è una lega austenitica ( $\gamma$ ) base Ni-Cr-Fe rinforzato attraverso soluzione solida o precipitazioni di fasi indurenti coerenti -  $\gamma'$ ,  $\gamma''$  - o di altre fasi quali carburi e nitruri. La precipitazione di fasi coerenti è la scelta principale quando si richiede un incremento di proprietà meccaniche. Questa si ottiene attraverso trattamenti di invecchiamento che ne causano la loro precipitazione.  $\gamma'$  e  $\gamma''$  contribuiscono intensamente al rinforzo della matrice  $\gamma$  grazie a:

- Resistenza intrinseca delle fasi;
- Differenza nelle costanti di cella tra fasi e matrice (*misfit*);
- Anti-phase boundary energy (APB) delle fasi, proporzionale all'energia utile alle dislocazioni attraversare  $\gamma'$  e  $\gamma''$ .

$\gamma''$  ( $\text{Ni}_3\text{Nb}$ ) è la principale fase rinforzante caratterizzata da una struttura ordinata tetragonale a corpo centrato,  $D0_{22}$  coerente alla matrice. Tipicamente si presenta sotto forma discoidale dispersa nella matrice. Rispetto a  $\gamma'$  ha un maggiore misfit e contribuisce maggiormente al rinforzo della lega. In aggiunta, l'alta concentrazione di Nb ne favorisce cinetiche di precipitazione molto più lente riducendo così la tendenza a SAC e incrementando la saldabilità della lega stessa. L'aspetto negativo di questa fase riguarda la sua stabilità termica.  $\gamma''$  è una fase metastabile, a temperature intorno ai  $650^\circ\text{C}$  tende a trasformarsi in  $\delta$  (Mignanelli et al., 2017). Quest'ultima avente struttura ortorombica del tipo  $D0_a$  è incoerente con la matrice e non fornisce alcun rinforzo meccanico al materiale (S. Li, Wei, Shi, Zhu, & Zhang, 2015).

Al contrario,  $\gamma'$  è una fase stabile, presente in Inconel 718 in una frazione di circa 3% in volume, inferiore rispetto al 20% di  $\gamma''$ . Come quest'ultima anche  $\gamma'$  è coerente e presenta una struttura ordinata cubica a facce centrate  $L1_2$ . Contrariamente a  $\gamma''$ , questa fase si può presentare sotto forma cuboidale o simil-sferica in funzione del misfit con la matrice. Alto misfit ne causano forma cubica, mentre bassi valori una forma sferoidale, tale variazione è funzione della composizione della lega che gioca un ruolo fondamentale sul controllo di questo parametro (Shao et al., 2019). Data la sua stabilità, questa fase è spesso associata a leghe per applicazioni ad alta temperatura (fino a  $1000^\circ\text{C}$ ) ma non prodotte per via AM. Questo perchè a differenza di  $\gamma''$ , essa soffre di alte cinetiche di precipitazione che sottopongono le leghe di Ni a rischio SAC quando presente in alte frazioni in volume.

Come tutte le leghe metalliche, anche Inconel 718 è caratterizzata dalla possibile presenza di fasi deleterie. Tra le forse più note e comuni sono le *fasi di Laves*. Quest'ultime si generano a causa dell'elevato contenuto di elementi pesanti in lega. Infatti, la loro composizione chimica è del tipo  $(\text{Ni,Fe,Cr})_2(\text{Nb,Mo,Ti})$ , con struttura esagonale compatta (hexagonal  $C_{14}$ ) incoerente con la matrice (Deng et al., 2018). Questa fase secondaria si crea a causa dei ridotti coefficienti di diffusione degli elementi interessati. Questo aspetto spiega il perchè la sua presenza in strutture processate in L-PBF è inevitabile. Le veloci cinetiche di raffreddamento impediscono a tali elementi di diffondere propriamente arricchendone le regioni interdendritiche. Tale situazione porta alla formazione di Laves, che tuttavia è indesiderato data la sua natura fragile e propensa a criccheggio. In aggiunta, l'alta concentrazione in Nb riduce sensibilmente la concentrazione libera di questo importante elemento, formatore della principale fase rinforzante  $\gamma''$ .

Un'altra fase, tuttavia meno tipica, è  $\eta$ . Questa è caratterizzata da una struttura ordinata esagonale compatta del tipo  $D0_{24}$ . Questa fase condivide la composizione chimica con la fase  $\gamma'$  ( $\text{Ni}_3\text{Ti}$ ) sebbene studi più recenti ne abbiano identificato una possibile differente composizione. La parziale solubilità per elementi quali Co, Al, Cr e Nb sono alla base di queste assunzioni che ne citano una stechiometria del tipo  $(\text{Ni,Co})_3(\text{Ti,Al,Nb})$  o  $\text{Ni}_3\text{Al}_{0.5}\text{Nb}_{0.5}$  (Antonov, Detrois, Helmink, & Tin, 2015; Fedorova, Rösler, & Gehrman, 2014).

Questa fase si presenta per lo più con una morfologia aciculare o a lamelle fini, morfologicamente molto simile alla fase  $\delta$ . Tali strutture sono solitamente associate a lunghe esposizioni ad alta temperatura della lega, o ad alte concentrazioni di elementi quali Ti e Co. Il primo ha però un maggiore effetto nella stabilizzazione di questa fase.

Generalmente, dato il rapido raffreddamento tipico dei processi L-PBF fasi come  $\gamma'$ ,  $\gamma''$ ,  $\delta$  e  $\eta$  non sono in grado di precipitare. Come visibile in **Fig.12** (Lippold, Kiser, & DuPont, 2011), nella condizione as-built tali fasi non possono essere presenti, lo saranno solo carburi e le fasi di Laves.

## ***In-situ Alloying***

*In-situ alloying* si riferisce a un processo utile all'ottenimento di una composizione desiderata, il quale si pone in diretto contrasto con l'utilizzo delle più tradizionali polveri pre-alligate. A differenza di queste ultime, si basa infatti sulla miscelazione di diverse polveri.

La necessità di studiare tale processo nasce da problematiche relative ai più tradizionali processi di casting. Il lento raffreddamento può portare allo sviluppo di fasi indesiderate, talvolta difficilmente removibili attraverso trattamenti termici successivi. Le cinetiche di raffreddamento coinvolte nel processo L-PBF risolve tale problematica, non dando tempo a tali fasi secondarie di nucleare nella pozza di fusione.

Negli ultimi anni, le tecnologie di fusione a letto di polvere sono state provate efficaci (Krakhmalev, Yadroitsev, Yadroitsava, & De Smidt, 2017) nella produzione di leghe quali Ti6Al4V, Ti-Nb e Al-Si partendo da polveri madre (Vora, Mumtaz, Todd, & Hopkinson, 2015; Fischer, Joguet, Robin, Peltier, & Laheurte, 2016). In particolare, nel caso della lega Ti-Nb, le alte temperature di fusione della lega rendono molto costosa la via della pre-alligazione rendendo al contrario conveniente il *situ-alloying*.

Tuttavia, l'alligazione in loco non è un processo privo di problematiche, maggiormente quando è coinvolto un processo di AM. La creazione di un blend mette in gioco il rischio di segregazione delle polveri, particolarmente importante nel caso in cui si considerano polveri con diversa distribuzione granulometrica. Inoltre, quest'ultimo aspetto gioca un importante ruolo sulla *flowability* delle polveri e su una loro efficace stesura da parte del sistema di deposizione del letto di polvere. Polveri diverse sono caratterizzate da diversa interazione laser-materia, aspetto che influenza la termodinamica della pozza di fusione generata dal sistema ottico. In aggiunta, la termodinamica del processo è influenzata anche dalla sintesi istantanea della lega. Essa è infatti associata ad un'entalpia negativa (Simonelli et al., 2018) che altera i processi termodinamici durante la stampa (Yadroitsev, Krakhmalev, & Yadroitsava, 2017).

Tutti questi fattori devono essere considerati simultaneamente e rendono i parametri di stampa tipicamente usati nelle polveri pre-alligate non idonei. Ogni sistema di polveri necessita perciò un processo di ottimizzazione dei parametri ad-hoc. Questo in modo da fornire alle polveri una quantità di energia utile all'ottenimento di una viscosità tale da permettere un'efficace miscelazione dei componenti in gioco. Inoltre, la velocità di scansione dev'essere idonea ad evitare *lack-of-fusion* di entrambi le polveri e favorirne la migliore inter-diffusione possibile.

Sarà tuttavia difficile evitare, anche se in ridotta entità, la presenza di segregazione o zone con gradienti chimici percepibili. E' perciò necessario favorire lo studio di adeguati trattamenti termici che, uniti ad adeguate tecniche di miscelazione delle polveri e la scelta delle opportune distribuzioni granulometriche, permettano di rendere il processo ripetibile e il più possibile simile all'ideale condizione pre-alligata.

## **Stato dell'Arte dell' Inconel 718**

Nonostante l'ampio utilizzo dell' Inconel 718 sia dovuto alla presenza di  $\gamma''$ , la sua sostituzione a favore di una maggiore abbondanza di  $\gamma'$  è stata il principale obiettivo di molti recenti lavori di

ricerca. Lo sviluppo dei motori aeronautici va sempre più nella direzione di temperature di lavoro maggiori, che mettono a rischio l'utilizzo di questa lega. Tuttavia, non è possibile incrementare sensibilmente la massima temperatura di applicazione finché  $\gamma''$  rappresenta la principale fase rinforzante. Sulla base di ciò diversi studi hanno iniziato a tentare di sostituire  $\gamma''$  con  $\gamma'$ . Ciò presenta la solita problematica relativa alla rapida precipitazione di quest'ultima che deteriora la saldabilità della lega, sottoponendola a SAC. Vennero perciò investigate le cause sorgenti di tale comportamento. Si scoprì che agendo sulla temperatura di solvus di  $\gamma'$ , era possibile ridurre le cinetiche di precipitazione a livelli non di molto superiori a  $\gamma''$ . Ciò rese così possibile associare la presenza della fase  $\gamma'$  a buoni valori di saldabilità (Rösler, Hentrich, & Gehrman, 2019; Xie et al., 2019).

Sulla base di queste scoperte negli ultimi due decenni sono state sviluppate principalmente tre 718-derivati - Allvac 718Plus, VDM 780 Premium e K4750. Tutti questi hanno in comune la modificazione della composizione chimica al fine di ridurre la temperatura di solvus di  $\gamma'$ . Questo al fine di ottenere un sostanziale incremento della temperatura di applicazione della lega attraverso la sostituzione di  $\gamma''$  da parte di  $\gamma'$ , senza ridurre le eccezionali prestazioni meccaniche delle leghe in questione.

Allvac 718Plus è una lega base Ni-Cr-Co-Fe con una temperatura massima di applicazione 100F (55°C) superiore all'Inconel 718 (W.-D. Cao, Kennedy, Antony, & Smythe, 2013). A differenza di quest'ultima, la lega 718Plus è rinforzata prevalentemente da  $\gamma'$ . Caratteristica che tuttavia non ne riduce la saldabilità. Le modifiche alla sua composizione chimica la rendono infatti *readily weldable*, addirittura più saldabile della lega Waspalloy (già usata in AM) (ATI, 2013). Le principali differenze con l'Inconel 718 stanno nel maggiore contenuto di Al ( $\gamma'$ -stabilizzatore), minore contenuto di Fe (favorisce la generazione di fasi di Laves) e di Ti ( $\gamma'$ - e  $\eta$ -stabilizzatore) e all'aggiunta di W e Co. Questi ultimi non sono presenti nell'Inconel 718. Co in particolare contribuisce ad una maggiore presenza di  $\gamma'$  attraverso la riduzione della solubilità di Ti e Al nella matrice. Il W invece venne aggiunto al fine di incrementare la stabilità ad alta temperatura. Tale ruolo è coadiuvato dal mantenimento di alte concentrazioni di Nb. La sua parziale solubilità nella fase  $\gamma'$ , unita al suo basso coefficiente di diffusione termica, contribuisce a ridurre le cinetiche di precipitazione di  $\gamma'$ . Tutti questi aspetti permisero a questa lega di incrementare  $\gamma'$  senza ridurre la lavorabilità della lega (Kennedy, 2005; Tsang et al., 2010; Löhnert & Pyczak, 2010; Kienl, 2019).

VDM 780 Premium è stata creata al fine di incrementare i limiti termici e le proprietà meccaniche dell'Inconel 718. Questa lega vede infatti la completa assenza di  $\gamma''$  a favore di  $\gamma'$ , la quale raggiunge frazioni in volume pari al 35% (Bergner, Rösler, Gehrman, & Klöwer, 2018; Rösler et al., 2019). Tale elevato contenuto di  $\gamma'$  non solo permette di ottenere elevate prestazioni meccaniche ma ne garantisce un incremento di 180F (100°C) rispetto all'Inconel 718. Per quanto riguarda la composizione chimica, le principali differenze riguardano un maggiore contenuto di Al, minore di Ti e la sostituzione del Fe con 25%<sub>wt</sub> di Co. Anche in questo caso il Co ha avuto un ruolo essenziale. Nonostante l'elevato contenuto di Al che conferisce il 35% in volume di fase  $\gamma'$ , la lega risulta eccezionalmente saldabile secondo **Fig.9**. Tale aspetto è dovuto al fatto che il Co, oltre a ridurre la solubilità di Ti e Al nella matrice come precedentemente detto, esso riduce anche intensamente  $\gamma'_{solvus}$  (Fu, Dong, Zhang, & Xie, 2009; Fedorova et al., 2014). Così facendo, la temperatura di solvus della fase  $\gamma'$  nella lega 780 Premium è di 950°C, soli +20°C rispetto al valore tipico della fase  $\gamma''$  nella lega Inconel 718. Ciò ne garantisce un'elevata saldabilità a fianco di ottime proprietà meccaniche date dall'alto contenuto di fase rinforzante. Tuttavia, l'alto contenuto di Co incrementa il prezzo della lega, riducendo uno degli aspetti più concorrenziali dell'Inconel 718, il fatto di essere una superlega relativamente poco costosa.

K4750 è una lega cast sviluppata per applicazioni aeronautiche, ancora non utilizzata nel settore AM. Anch'essa si basa sull'assenza della fase  $\gamma''$  a favore della principale fase rinforzante  $\gamma'$  (Xie et al., 2019). Le principali differenze rispetto all'Inconel 718 sono il ridotto contenuto di Nb e Fe, e l'aggiunta di W e Ti (3%<sub>wt</sub>). L'aggiunta di un così alto contenuto di Ti senza la presenza di Co (presente nelle precedenti leghe), causa problematiche per quanto riguarda la saldabilità. Seppur questa lega sia riuscita a ottenere maggiori prestazioni meccaniche con un guadagno termico di 180F (100°C) (Ou et al., 2019), secondo la **Fig.21** essa ricade nella categoria "*Difficult to Weld*". Seppure con delle problematiche, l'attuale studio di leghe come la CM 247LC, aventi anche maggiori difficoltà di lavorazione, fa ben sperare nella sua possibile futura applicazione nel settore AM.

La lega sotto studio durante questo progetto di tesi, nominata Inconel 718 + Ti, mira sotto certi punti di vista a scopi diversi rispetto alle ricerche appena descritte. Infatti, mentre questi studi sono focalizzati sull'incremento della capacità termica, minori sforzi sono stati fatti per quanto riguarda l'incremento delle proprietà meccaniche nel range di applicazione della 718 per via additive. In particolare vi è una lacuna riguardante il processo di alligazione in loco e i suoi possibili effetti sulle proprietà finali del componente. L'aggiunta di Ti può avere infatti diversi effetti, positivi o negativi. Da un lato, incrementa la durezza e i carichi di snervamento dopo trattamento termico. Fenomeno dovuto al maggiore sviluppo di fase  $\gamma'$ , la quale si aspetta porti ad una riduzione di duttilità. Allo stesso tempo, come detto precedentemente, una maggiore presenza di titanio incremento può portare al peggioramento della saldabilità, alla generazione di cricche e una maggiore porosità. In aggiunta, la presenza di un feedstock sotto forma di blend di polveri diverse, nasconde un'intrinseca inomogeneità che si rifletterà nella microstruttura della lega. Probabili segregazioni saranno sorgente di possibile creazione di fasi secondarie, quali intermetallici. In particolare, l'alta concentrazione locale di Ti potrebbe favorire la precipitazione dopo trattamento termico della fase intermetallica  $\eta$ .

## Materiali e Metodi

Lo studio ha coinvolto un blend di due polveri utilizzate come feed nel processo di L-PBF (Mlab Cusing R ,Concept Laser). In particolare, sono state miscelate polveri di titanio e Inconel 718 in rapporto 1:99 (1%<sub>wt</sub> Ti e 99%<sub>wt</sub> Inconel 718) tramite l'utilizzo di cilindri rotanti per un tempo di 24h. Le polveri provenivano in parte dal riutilizzo di polveri già processate, motivo che giustifica la forte presenza di protuberanze adese a particelle madri (satelliti). In particolare, il precedente utilizzo di parte della polvere e il processo di miscelazione hanno causato la parziale adesione termica o meccanica della polvere di titanio alla polvere di Inconel 718, **Fig.22**. Tale aspetto non è tuttavia da considerarsi negativo. Sebbene la presenza di satelliti riduce la *flowability* della polvere, la presenza di queste escrescenze fisicamente o meccanicamente adese ad altre particelle, permette in un qual modo di incrementare l'omogeneità del feedstock.

Come visibile in **Fig.23**, il processo ha coinvolto una prima fase (Job1) di ottimizzazione dei parametri. Questa è necessaria, in quanto la risposta laser-materia cambia in funzione della composizione della polvere. In questo caso, questa prima fase ha riguardato la modifica dei parametri tipici dell'Inconel 718 utilizzati come valori di riferimento e punto di partenza del metodo. Durante tale fase, diversi campioni sono stati stampati utilizzando una metodologia DoE (Design of Experiment) che permette la gestione di sistemi ad elevato numero di variabili. In tal modo è stato possibile capire l'influenza del singolo parametro sul componente stampato. Ogni serie di campioni dopo essere stata rimossa dalla *building platform* attraverso EDM (Electro Discharge Machining), ha subito un processo di preparazione metallografica, 5.3. L'efficacia dei parametri utilizzati è stata definita attraverso analisi metallografica di porosità e durezza dei singoli campioni. Una volta ottenuti risultati soddisfacenti per quanto riguarda tali proprietà, i parametri ottimizzati vennero usati per lo stampaggio dei campioni utili a proseguire in modo più dettagliato il processo di caratterizzazione.

Quest'ultimo ha coinvolto la caratterizzazione dei campioni nella condizione as-built (ab) e a seguito di due trattamenti termici - semplice solubilizzazione, solubilizzazione (ST) e doppio invecchiamento (SDAG). Tali trattamenti seguirono lo standard AMS 5667 visibile in 5.2, tipico trattamento termico eseguito su campioni in Inconel 718. La caratterizzazione coinvolse l'analisi di immagine con software ImageJ, analisi con microscopio elettronico a scansione (SEM) e ottico (OM), mappatura degli elementi tramite analisi a dispersione di energia (EDX) e analisi meccaniche di microdurezza (Vickers, Brinell).

Quest'ultima fase ha coinvolto la stampa e l'analisi sia di campioni di *situ-alloying* che di puro Inconel 718. Quest'ultimo è stato usato come riferimento di controllo per avere un'idea chiara del contributo del Ti su ogni step del processo.

La porosità di ogni singolo campione è stata misurata grazie all'analisi delle immagini attraverso il software ImageJ delle immagini acquisite con il microscopio ottico. L'analisi di Archimede venne utilizzata come analisi di conferma dei valori ottenuti via ImageJ.

Lo studio ha coinvolto due stampe di ottimizzazione (Job1 e Job2) che hanno permesso l'ottenimento di parametri di stampa idonei all'ottenimento di una densità elevata. La terza stampa (Job3) si è invece focalizzata sulla caratterizzazione metallografica dei campioni di Inconel 718 puro e di Inconel 718+Ti.

## Discussione dei Risultati

### Job1

Lo scopo di questa prima fase è stato l'ottimizzazione dei parametri di processo al fine di ottenere prodotti densi al pari dei tipici valori ottenibili con l'Inconel 718. In particolare, partendo dai parametri tipicamente coinvolti nello stampaggio dell'Inconel 718 è stato eseguito un DoE (Design of Experiment). Tale metodo ha coinvolto la variazione di hatching distance (HD), scanning speed (SS) e scanning strategy (Stripe/67°, Island/Meander) mantenendo costanti la potenza del laser e lo spessore del layer. Data la sola necessità di ottenere alte densità, il processo di preparazione metallografica nella sezione 5.3, non ha coinvolto l'attacco acido con reagente Kalling n° 2.

Il processo di stampa ha portato alla produzione di 16 campioni cubici (1cm di lato), i quali a seguito della misurazione della porosità tramite ImageJ e densità di Archimede hanno chiarito la necessità di modificare ulteriormente tali parametri di processo. In **Tabella 8** sono visualizzati i valori di porosità in funzione del VED coinvolto, poi plottati in **Fig.31**. In **Fig.32** sono visibili diverse morfologie tipicamente presenti nel caso di un non corretto settaggio dei parametri di processo. Nella figura in basso a destra sono infatti presenti porosità di due tipologie, piccole e sferiche o di forma irregolare. Le seconde sono collegabili al fenomeno di *lack-of-fusion*. Tale immagine è infatti relativa a bassi valori di VED, intorno ai 130 J/mm<sup>3</sup>. Le piccole porosità sferiche possono solitamente essere relative all'attivazione del *keyhole-mode* o alla presenza di gas di processo intrappolato nella pozza di fusione. Gas che può provenire sia dal processo di stampa 3D o direttamente dal processo di atomizzazione delle polveri. Dati i valori di VED coinvolti nella produzione di tale campione, la prima ipotesi relativa al keyholing è da escludere. Tipica è anche la condizione delle due figure sulla sinistra (197 J/mm<sup>3</sup> e 226 J/mm<sup>3</sup>). In tali figure, pur essendo ad alti valori di VED, la morfologia è simile al fenomeno di *lack-of-fusion*. Ciò non è possibile dati gli alti valori di densità energetica. Questo fenomeno assume invece il nome di *over-heating* (OH), **Fig.33**. L'eccessivo surriscaldamento causa la generazione di stress superficiali nel materiale che causano lo sviluppo di rugosità. Tale irregolarità causa difficoltà nella deposizione del successivo layer e un assorbimento inhomogeneo dell'energia fornita dal laser. Di conseguenza si ha la generazione di porosità irregolari di grande dimensione, caratterizzate dalla presenza di particelle parzialmente fuse.

Osservando tali dati è possibile notare la tendenza dei campioni a mostrare ridotti valori di porosità per valori inferiori tra i 158 J/mm<sup>3</sup> e i 174 J/mm<sup>3</sup> (minimo del trend). Considerando tale tendenza e i massimi di densità ottenuti nel caso di 158 J/mm<sup>3</sup>, si optò per un secondo DoE lavorando su range minori di VED.

### Job2

Il secondo Job ha coinvolto la stampa di 5 campioni aventi la stessa taglia dei precedenti. In aggiunta, dato l'ottenimento di migliori densità nei campioni stampati durante il Job1 con strategia "Stripe/67°", tutti i campioni di questo Job utilizzarono tale tecnica di stampa. Come visibile in **Tabella 9**, la principale differenza in confronto al Job1, oltre alla singola strategia di scansione, è il diverso spessore del layer, dai precedenti 20  $\mu m$  a 15  $\mu m$ . Il Job2 ha portato all'ottenimento di valori di densità mediamente superiori alla precedente stampa, **Tabella 10**. In particolare,

il campione 02 ha portato all'ottenimento di una densità pari a circa 99,8%. Tale valore venne considerato soddisfacente e adatto alla continuazione del processo di caratterizzazione. Non solo rappresenta un buon valore di densità, ma conferma che l'aggiunta di polveri di Ti non ha in realtà influito sulla saldabilità della lega.

### Job3

**As-Built** Questo step ha coinvolto l'analisi di 20 campioni cubici, con le stesse caratteristiche geometriche dei precedenti. Tuttavia, tutti loro sono stati stampati con i parametri ottimizzati (campione 02, Job2), **Table 11**. Dei 20 campioni, 10 vennero prodotti con puro Inconel 718 (IN718) e i restanti con Inconel 718 + Ti (IN718+Ti). Per ogni categoria, 1 campione venne lasciato nella condizione as-built (ab), 6 vennero solubilizzati (ST) e 3 sia solubilizzati che invecchiati (SDAG).

Dall'analisi ottica dei campioni as-built attaccati con reagente Kalling n° 2, è possibile vedere la tipica struttura "ad arco" delle pozze di fusione che riflette la distribuzione gaussiana dell'energia fornita dal laser. L'aggiunta di Ti ha rivelato una leggera influenza sulla geometria delle pozze di fusione portandone ad un incremento del 10% nella profondità e dell' 8.5% nella larghezza. In **Fig.36** destra, sono apprezzabili zone di colore nero. Tali aree sono relative a segregazioni di Ti, o zone in cui le particelle sono parzialmente fuse, visibile anche in **Fig.37**. Le zone ricche di Ti vengono infatti corrose maggiormente dall'attacco chimico risultando in una colorazione oscurata durante l'analisi ottica.

Dall'analisi al microscopio ottico a scansione è possibile avere maggiori informazioni riguardo alla microstruttura e alle fasi generate. In particolare, in **Fig.38** si nota la microstruttura direzionale tipica del processo L-PBF. Allo stesso tempo sono presenti in entrambi i materiali strutture cellulari/dendritiche ricche in fasi di Laves. Mentre le cinetiche di raffreddamento inibiscono la formazione di fasi indurenti, le zone interdendritiche sono ricche in fasi di Laves, alcuni carburi ricchi in Nb e probabilmente alcuni elementi segregati. Durante il raffreddamento tali zone si arricchiscono in Nb, Mo e C. Alte concentrazioni di questi elementi permettono l'attivazione di due reazioni eutettiche. La formazione della matrice  $\gamma$  arricchisce le zone interdendritiche di Nb e C che attivano la prima reazione eutettica,  $L \rightarrow (\gamma + NbC)$ . Tale reazione riduce il contenuto di C causando l'attivazione della seconda reazione eutettica,  $L \rightarrow (\gamma + Laves)$  (Tucho, Cuvillier, Sjolyst-Kverneland, & Hansen, 2017). Quest'ultima fase, essendo ricca in metalli dall'elevato peso atomico, risulta bianca durante l'analisi agli elettroni retrodiffusi (BSE) nel processo SEM.

**Condizione Solubilizzata** Il trattamento di solubilizzazione mira ad incrementare l'omogeneità della lega attraverso la diffusione termica in zone ad alto gradiente chimico. Cioè, mira ad eliminare segregazioni ed eventuali fasi secondarie al fine di omogenizzare la composizione chimica della lega rendendo la matrice il più ricca possibile in elementi formatore delle fasi rinforzanti che verranno precipitate nel successivo trattamento di invecchiamento.

La temperatura utilizzata, 1080°C, è tuttavia non abbastanza elevata per la completa rimozione della fase di Laves che, seppur in piccoli nuclei, potrebbe ancora essere presente nella matrice. Al contrario, tale temperatura supera la temperatura di solvus della fase  $\delta$  impedendone la formazione. Tale trattamento però porta alla rimozione delle microstrutture tipiche dell'interfaccia tra layers (pozze di fusione) e incrementa l'isotropia della lega in confronto alla condizione as-built.

Durante il trattamento di solubilizzazione si ha una forte riduzione delle tensioni residue interne al materiale e la precipitazione di carburi. L'analisi SEM-EDX ha permesso l'identificazione in entrambi i materiali di carburi ricchi in (Nb,Ti) del tipo MC e carburi ricchi in (Mo,Nb) del tipo  $M_6C$ , visibili in **Fig.39** e **Fig.42**. In generale può essere notato che i campioni IN718+Ti presentano una maggiore attività nelle zone vicine alle segregazioni di Ti. L'elevato disordine di tali zone incrementa localmente l'energia libera del sistema favorendone i meccanismi di diffusione termica durante i trattamenti termici. Ciò si nota dal fatto che tali zone sono ricche di carburi e fasi secondarie mentre il resto della matrice ne appare relativamente libero. In aggiunta, confrontando IN718+Ti con il riferimento IN718 si nota come la taglia di questi precipitati sia maggiore nel primo materiale.

Forse l'aspetto più distintivo del IN718+Ti è la presenza di fasi aciculari. Tale morfologia è solitamente associata in letteratura alla fase  $\delta$ , o alla fase  $\eta$ . Un'analisi approfondita con SEM-EDX ha permesso di chiarire la possibile natura di tale fasi. In **Fig.41** è possibile notarne l'elevata concentrazione in Ti, Nb e Ni. In particolare, una presenza così alta di Ti rende non possibile l'associazione di tale fase con la fase  $\delta$ , rendendo più fattibile la possibilità che si tratti in realtà di fase  $\eta$  ( $Ni_3Ti_{0.5}Nb_{0.5}$ ).

**Condizione di Invecchiamento Termico** Il trattamento di invecchiamento, eseguito su campioni precedentemente solubilizzati, serve a favorire la precipitazione controllata delle fasi rinforzanti  $\gamma'$  e  $\gamma''$ . Esso si compone di due fasi -  $720^\circ C \times 8h$ /raffreddamento in forno (FC)+  $620^\circ C \times 8h$ /raffreddamento ad aria (AC). Sebbene presenti, queste fasi non sono tuttavia osservabili attraverso microscopia a scansione elettronica date le dimensioni nel range della nanoscala. Al fine di caratterizzarle in modo opportuno e di calcolarne la frazione in volume sarebbe necessario l'utilizzo di tecnologie quali la microscopia a trasmissione elettronica (TEM).

In **Fig.43** è visibile l'effetto del trattamento di invecchiamento, in combinazione al trattamento di solubilizzazione. Mentre tali trattamenti non portano alla rimozione dell'orientamento dei grani cristallini lungo *building direction* nei campioni IN718, sembrano esserlo per quanto riguarda IN718+Ti. Sebbene questo fenomeno necessiterebbe ulteriori analisi con EBSD per essere confermato, potrebbe essere giustificabile osservando **Fig.44**. Mentre in IN718 si ha un'omogenea distribuzione di precipitati a bordo grano, nell'IN718+Ti tali fase si concentrano attorno alle segregazioni di Ti diminuendo l'effetto di pinning sui bordi grano nel resto della matrice.

Il trattamento termico si mostra però efficace seppur non sufficiente, per quanto riguarda la diffusione di Ti. Le segregazioni diminuiscono in concentrazione e dimensione. Tramite analisi di immagine è stato infatti possibile stabilirne una riduzione della dimensione del 26% nel solo trattamento di invecchiamento.

Tale trattamento ha contribuito anche all'incremento della concentrazione di fasi secondarie quali principalmente carburi di tipo  $M_6C$  ed  $M_{23}C_6$ , **Fig.47**. In quest'ultima figura si notano inoltre delle fasi aciculari di piccola dimensione. Apparentemente simili a  $\gamma''$ , sono in realtà di altra natura. La loro dimensione è infatti molto superiore alle decine di nanometri tipiche della fase  $\gamma''$  dopo trattamento di invecchiamento (AMS 5667). Dall'analisi lineare dei carburi in **Fig.47** è possibile notare come il Ti picchi nelle regioni in cui le suddette fasi aciculari attraversano la sezione del carburo. Tale comportamento potrebbe significare che tali fasi sono in realtà fase  $\eta$  nucleata in un secondo momento, senza aver avuto il tempo necessario a crescere come le fasi in **Fig.43f**.

**Microdurezza** La valutazione della microdurezza è stata eseguita su tutti i campioni e valutata attraverso la media di 5 valori presi in siti differenti. In generale, per entrambi i materiali il valore maggiore di durezza riguarda i campioni SDAG. Questo è dovuto alla presenza di fasi rinforzanti, assenti nelle altre condizioni. Nella condizione SDAG, i due campioni di IN718 e IN718+Ti mostrano durezza di  $425 \pm 5$  HB<sub>10</sub> e  $393 \pm 6$  HB<sub>10</sub>, rispettivamente. Un guadagno rispettivamente del 44% e 33% rispetto alle relative condizioni as-built. Per quanto riguarda la condizione ST, IN718+Ti presenta un comportamento insolito. Spesso la condizione ST presenta in IN718 una durezza inferiore alla condizione as-built (-17%). Questo si spiega grazie al fatto che gli intensi stress residui interni al materiale dopo il processo di stampa causano un irrigimento del materiale. Inoltre parte di queste tensioni portano alla deformazione plastica del materiale e al suo relativo incrudimento. L'alta densità di dislocazioni fa sì che interagiscano tra di loro, favorendo un ulteriore indurimento del materiale as-built. Tali stress vengono però rilasciati durante il trattamento di solubilizzazione che ne riduce così la durezza rispetto alla condizione non trattata. Al contrario IN718+Ti presenta un valore maggiore di durezza (+8%). Il fatto che non mostri tale tipico comportamento può essere solamente connesso all'aggiunta di Ti dato che tali fenomeni avvengono comunque anche all'interno di tale materiale. Se le fasi aciculari fossero realmente fase  $\eta$ , questo fenomeno potrebbe trovare una spiegazione. In letteratura, la fase  $\eta$  viene infatti descritta come capace di contribuire in modo maggiore alla durezza rispetto a  $\gamma'$ . La prima ha infatti una durezza di 450 kg/mm<sup>2</sup> confronto ai 220 kg/mm<sup>2</sup> della seconda. Tuttavia ciò viene descritto non valere nel caso in cui la fase  $\gamma'$  sia dispersa in dimensione nanometrica. Secondo tali teorie, la condizione ST-IN718+Ti ha una durezza maggiore perchè come verificato, la solubilizzazione favorisce la precipitazione della fase  $\eta$ . Tale fase, non solo contribuisce in modo intenso alla durezza della lega ma è assente nell' IN718. Nel caso di SDAG-IN718+Ti, la presenza di tali intermetallici e di fasi secondarie (quali carburi) di maggiori dimensioni depauperava la matrice di Nb e Ti, stabilizzanti delle principali fasi rinforzanti. Ciò porterebbe a una ridotta precipitazione di  $\gamma'$  e  $\gamma''$  causando minori valori di durezza rispetto all'IN718. In quest'ultimo, la saturazione della matrice di elementi quali Nb e Ti, porta a un'intensa precipitazione di fasi indurenti e quindi ad maggiori valori di durezza.

## Conclusioni

### Risultati e Punti Salienti

I risultati ottenuti mettono alla luce la fattibilità del *situ-alloying* come percorso alternativo per operare modifiche sulla Inconel 718 seppure provino la necessità di ulteriori studi. Il processo è riuscito tuttavia a fornire campioni quasi completamente densi, confrontabili con i valori tipici ottenuti dall'Inconel 718. Tuttavia, i parametri di processo hanno richiesto di essere modificati, in quanto l'utilizzo dei parametri di stampa tipici della lega di riferimento hanno causato lo sviluppo di molta porosità.

Come previsto, alti valori di densità non significano necessariamente omogeneità. La presenza di polveri di Ti ha causato la generazione di numerose segregazioni, zone caratterizzate da alto gradiente chimico. Questo si dimostra essere una delle principali problematiche relative al *situ-alloying*. Tuttavia i trattamenti termici si sono dimostrati efficaci nel ridurre la taglia, circa del 26% dopo solo invecchiamento. In ogni caso, questi ultimi non sono sufficienti dato che nella condizione SDAG tali segregazioni hanno ancora una taglia pari a  $31\mu\text{m}$ .

In tali regioni caratterizzate da maggiore disordine atomico, i processi di diffusione sono favoriti e portano allo sviluppo di seconde fasi, come carburi. Fenomeno che ha diverse conseguenze sia sulla microstruttura che sulle prestazioni meccaniche della nuova lega. Primo, la precipitazione di carburi ricchi in Nb nelle aree ad alta concentrazione di Ti, ostacola una precipitazione omogenea di carburi a bordo grano, comune invece in IN718. Questo comporta durante i trattamenti termici a un effetto maggiore sull'orientamento cristallino, causa del ridotto pinning sui bordi grano. Secondo, la microdurezza mostra un comportamento inusuale nel caso di IN718+Ti. Stando alla letteratura, un incremento del contenuto di Ti dovrebbe portare a un maggiore sviluppo di  $\gamma'$  e quindi a una maggiore durezza. Al contrario, dopo invecchiamento la durezza di era minore in IN718+Ti che in IN718. Unendo la revisione di paper scientifici e i risultati dell'analisi microstrutturale, è stato possibile collegare la differenza nel comportamento meccanico allo sviluppo di fasi aciculari e micrometriche ricche in (Nb,Ti), non presenti in IN718. Nonostante la necessità di investigare il fenomeno attraverso tecnologie più precise, queste fasi aciculari potrebbero trattarsi di fase  $\eta$ . Infatti, essendo ricche in Nb e Ti, questa fase riduce la concentrazione di elementi formatori delle fasi rinforzanti e una ridotta precipitazione di  $\gamma'$  e  $\gamma''$ . La formazione di tale fase spiegherebbe il picco di durezza nella condizione solubilizzata (ST). Mentre, il suo sovra-invecchiamento supportato dalla ridotta precipitazione di fasi indurenti, spiegherebbe la riduzione del 7.5% della durezza di SDAG-IN718+Ti a confronto della lega di riferimento SDAG-IN718.

Lo sviluppo della fase  $\eta$  e la sua conseguenza sulla fase  $\gamma'$  dimostrano che l'aggiunta di polveri di Ti all'IN718 ha fallito per quanto riguarda l'obiettivo di realizzare una lega con maggiori prestazioni meccaniche. Chiarisce infatti la necessità di ulteriori studi al fine di ridurre l'inomogeneità della lega, sorgente dei problemi menzionati. Tuttavia, è probabile che con un'opportuno trattamento di omogenizzazione a temperature maggiori per tempi più lunghi permetterebbe l'ottenimento di una maggiore presenza di  $\gamma'$ , riuscendo così nell'intento. In ogni caso, la possibilità di ottenere un materiale quasi completamente denso apparentemente senza maggiori difficoltà del convenzionale IN718, suggerisce ci siano buone chances di implementare l'*in-situ* alloying come efficace e conveniente via per la produzione di composizioni desiderate su piccole scale di volume.

## Futuri Lavori

Al fine di completare la caratterizzazione microstrutturale sarebbe interessante effettuare ulteriori analisi attraverso un microscopio a trasmissione elettronica (TEM) e analisi ad elettroni retro-diffusi (EBSD). In particolare, l'unione di tali analisi permetterebbe la completa identificazione della fase  $\eta$ .

L'*in-situ* alloying diverrà un'alternativa efficace e conveniente ai convenzionali processi via pre-alligazione solo quando sarà caratterizzato completamente. L'ottenimento di valori di omogeneità paragonabili a tale condizione, richiede infatti lo studio di trattamenti termici su misura al fine di rimuovere completamente le segregazioni di Ti. Questo richiederebbe la definizione di un trattamento di omogenizzazione opportuno. E' infatti risaputo che l'omogeneità della lega dopo invecchiamento è strettamente legata al processo di omogenizzazione a cui la lega stata sottoposta.

In aggiunta, sarebbe interessante indagare l'effetto che la distribuzione granulometrica delle due polveri ha sul materiale dopo trattamento termico. Questo in modo da riuscire a definire la distribuzione granulometrica più adatta all'ottenimento di condizioni il più possibile assimilabili alla pre-alligazione. L'unione di questo e del precedente punto permetterebbero di trovare una soluzione alle problematiche relative all'omogeneità e di realizzare il massimo potenziale del *in-situ* alloying.

Infine, potrebbe essere interessante processare la stessa polvere sia con L-PBF che con EBM. Quest'ultimo infatti è caratterizzato da una temperatura di processo maggiore che potrebbe portare ad una riduzione della dimensione delle segregazioni di Ti. Investigazioni approfondite sulla relazione tra processo-microstruttura-proprietà permetterebbe l'utilizzo di tale tecnica nella tecnologia EBM, che come il L-PBF è ampiamente diffusa per quanto riguarda lo stampaggio 3D di materiali metallici.

## List of Abbreviations

ABD	Alloy-By-Design Modelling-Based Approach
AC	Air Cooling
AFRL	Air Force Research Lab
AM	Additive Manufacturing
AMS	Aerospace Material Specifications
ASTM	American Society for Testing and Materials
ATI	Allegheny Technologies Incorporated
BD	Building Direction
BHN	Brinell Hardness Number
BSE	Back Scattered Electrons
CAD	Computer-Aided Design
CHRT	Controlled Heating Rate Test
DoE	Design of Experiment
EBM	Electron Beam Melting
EDS	Electro-Discharge Machining
EDX	Energy Dispersive X-Ray Spectroscopy
EIGA	Electrode Induction Melting Gas Atomization
FC	Furnace Cooling
FC	Furnace Cooling
FCC	Face Centered Cubic
FDM	Fusion Deposition Modelling
FESEM	Field Emission Scanning Electron Microscopy
GA	Gas Atomization
HCP	High-Pressure Compressor
HPT	High-Pressure Turbine
IoT	Internet of Things
ISO	International Organization for Standardization
L-DED	Laser Direct Energy Deposition

## List of Abbreviations

---

L-PBF	Laser Powder Bed Fusion
LED	Linear Energy Density
LMD	Laser Metal Deposition
LOF	Lack-of-Fusion
LPT	Low-Pressure Turbine
MCP	Multi-layer Concurrent Printing
OBJ	Wavefront OBJect
OM	Optical Microscopy
PA	Plasma Atomization
PREP	Plasma Rotating Electro Process
PSD	Powder Size Distribution
PWA	Plasma Wire Atomization
PWHT	Post Welding Heat Treatment
RMT	Rapid Manufacturing Technology
RP	Rapid Prototyping
RT	Rapid Tooling
RTMH	Room Temperature Micro-Hardness
SAC	Strain Age Cracking
SE	Secondary Electrons
SEM	Scanning Electron Microscopy
SLA	Stereolithography Apparatus
SLM	Selective Laser Melting
SLS	Selective Laser Sintering
SM-L-PBF	Single Multi-mode Laser Power Bed Fusion
STL	Standard Triangle Language
TCP	Tetrahedrally Close Packed
TEM	Transmission Electron Microscopy
UTS	Ultimate Tensile Strength
VDM	Vereinigte Deutsche Metallwerke

## List of Abbreviations

---

VED	Volumetric Energy Density
VIM	Vacuum Induction Melting
WAAM	Wire Arc Additive Manufacturing
WC	Water Cooling
XRD	X-Ray Diffraction
YS	Yield Strength

## List of Figures

1	Design Process for AM . . . . .	5
2	Cube and Sphere Tessellation . . . . .	6
3	Classification of AM Processes Based on Energy Source and Delivery System for Metallic Components . . . . .	7
4	Layer-by-layer SLM Concept . . . . .	8
5	Development of Powder Defects After SLM Processing of a Ti6Al4V Powder Feedstock. . . . .	10
6	L-PBF process parameters. . . . .	12
7	By-Products Typical of SLM Processing. . . . .	14
8	Scanning Strategies . . . . .	15
9	Weldability Assessment Diagrams for Ni-base Superalloys Depending on the Chemical Composition . . . . .	22
10	Alloying Elements used in Ni-based Superalloys . . . . .	26
11	$\eta$ Phase and $\delta$ Phase Morphology . . . . .	32
12	Time-Temperature-Transformation Diagram Inconel 718 . . . . .	33
13	Sensibility to Strain Age Cracking via CHRT . . . . .	38
14	Stress Rupture Life and Thermal Stability Function of ATI 718Plus Chemical Composition . . . . .	39
15	Tensile YS and Elongation for ATI 718Plus, IN718 and Waspalloy Function of Temperature . . . . .	40
16	Influence of Chemical Composition on $\gamma'$ Solvus Temperature . . . . .	42
17	Quasi Binary Ni-Co Diagram Based on Inconel 718 with Co Replacing Fe and Partially Ni. . . . .	43
18	ThermoCalc Simulation of Isothermal Sections of the Quasi-ternary Ni–Al–Ti System at 800°C. The Composition of the other alloying elements is kept constant at 17% <sub>wt</sub> Co, 5.4% <sub>wt</sub> Nb, 18.7% <sub>wt</sub> Cr and 2.96% <sub>wt</sub> Mo. A constant Ti/Al ratio line is highlighted in red. . . . .	44
19	K4750 Thermodynamic Phase Diagram in <b>(a)</b> total and <b>(b)</b> partial version. . . . .	45
20	Precipitation Temperature of Equilibrium Phases (left) and their Weight Fractions (right) Depending on Ti Content. . . . .	46
21	Weldability Assessment Diagram for ATI 718Plus, VDM 780 Premium and K4750. . . . .	47
22	Morphology of inconel 718 Situ-Alloyed Powder. . . . .	49
23	Flow Chart of the Process Steps. . . . .	50
24	Mlab Cusing R L-PBF Printing Machine. . . . .	51
25	CONCEPT Mlab Cusing R Technical Sheet. . . . .	51
26	AMS5667 Heat Treatment for Inconel 718. . . . .	52
27	Optical Microscopy Leica DMI5000 M. . . . .	54
28	SEM-EDS Analysis. . . . .	56
29	LEICA VMHT-001 Microhardness Instrument . . . . .	58
30	Specimens out of the L-PBF process . . . . .	60
31	Porosity vs VED Referred to Job 1 . . . . .	62
32	Sample Cross-Sections with Scanning Parameters 95 W, 0.015 mm Respectively Power and Layer Thickness. OM Porosity and VED Are Shown Below Each Picture. Sample 07, 08, 09 at the Top; Samples 04, 15, 06 at the Bottom. . . . .	62
33	Process window for L-PBF . . . . .	63
34	Porosity vs VED Referred to Job 2 . . . . .	65

35	Sample Cross-Sections with Scanning Parameters 95 W, 0.02 mm Respectively Power and Layer Thickness. OM Porosity and VED Are Shown Below Each Picture. Sample 03 and 04 at the Top; Samples 01 and 02 at the Bottom. . . . .	65
36	Melt Pools Comparison of Optical Microscopy Images of IN718 and IN718 + Ti Samples at Magnification 100X . . . . .	67
37	SEM-EDX Analysis of a Non-Fully Melted Titanium Particle in the As-Buil Condition	68
38	Scanning Electron Microscopy on an As-Built Microstructure of IN718 and IN718+Ti Samples . . . . .	69
39	Linear EDX Scanning Electron Microscopy on Carbides Particles in a Solution Treated Microstructure of IN718 . . . . .	70
40	Scanning Electron Microscopy on a Solution Treated Microstructure of IN718 and IN718+Ti Samples . . . . .	71
41	EDX Maps by Scanning Electron Microscopy of a Solution Treated Microstructure of IN718+Ti . . . . .	72
42	Linear EDX Scanning Electron Microscopy of a Solution Treated Microstructure of IN718+Ti . . . . .	73
43	Scanning Electron Microscopy on a Solution Treated and Double Aged Microstructure of IN718 and IN718+Ti Samples . . . . .	75
44	Optical Microscopy on a Solution Treated and Double Aged Microstructure of IN718 and IN718+Ti Samples . . . . .	76
45	Size Distribution of Ti Segregations in IN718+Ti in Solution Treated and Solution treated+ Double Aged condition Through Image Analysis by ImageJ Software. . . . .	76
46	SEM-EDX analysis of a Ti-segregated area. . . . .	77
47	Linear SEM-EDX analysis of the Ti-segregated area in an Aged IN718+Ti at 900X magnification. . . . .	77
48	Brinell Hardness of IN718 and IN718+Ti Samples in As-Built (ab), Solution Treated (ST) and Solution Treated and Double Aged (SDAG) Condition. . . . .	79
49	Optical Microscopy of a solution treated IN718+Ti Sample Showing the Presence of Annealing Twins and Activated Recrystallization. . . . .	80

## List of Tables

1	Inconel 718 Chemical Composition . . . . .	25
2	Inconel 718 Principal Phases . . . . .	25
3	Elements Influence . . . . .	27
4	Allvac 718Plus Chemical Composition . . . . .	37
5	VDM Alloy 780 Premium Chemical Composition. . . . .	41
6	K4750 Chemical Composition (*Inconel 718 does not contain W) . . . . .	45
7	Printing Parameters Adopted for the Job 1 . . . . .	59
8	Porosity Percentage Values First DoE . . . . .	61
9	Printing Parameters Adopted for the Job 2 . . . . .	64
10	Porosity Percentage Values Second DoE . . . . .	64
11	Optimized Process Parameters Adopted in Job 3 . . . . .	66
12	Brinell Microharness Test Result of IN718+Ti and IN718 in the as-built (ab), Solution Treated (ST), Solution Treated and Double Aged (SDAG) Condition . . . . .	79
13	Common Microhardness Values for Cast, Wrought, L-PBF, EBM, and L-DED Processed Inconel 718 . . . . .	81

# 1 Introduction

## 1.1 Background

Laser powder bed fusion (L-PBF) technology, is part of the family of the 3D printing manufacturing processes able to build components layer-by-layer up to near net shape three-dimensional objects. Essentially, this process offers a high degree of freedom to the design of highly-complex structures. Based on additive manufacturing (AM), it stands as the opposite concept to conventional processes which instead rely on material removal.

The possibility of exploiting more complex structures and therefore reducing the final weight of the components paved the way for L-PBF in the aerospace sector. The interest in accessing this new technology lies in their need for lightweight structures and materials able to stand severe mechanical stresses in harsh environments at high temperatures. The Ni-based superalloys are the most common material when it comes to aero-engines, covering 50% of their total weight. Inconel 718 is the workhorse of this family of alloys and the predominant superalloy. It has been used for years as material for blades, discs, casing for high-pressure section of compressors (HPC), and as material for blades in the low-pressure turbine (LPT). Not only it owns excellent mechanical properties at high temperature, creep, rupture, and fatigue strength typical of the Ni-base superalloys but it is characterized by good weldability. Features that have allowed this alloy to widely spread in the additive manufacturing sector. When it comes to the L-PBF process, usually the feed of the process is a pre-alloyed powder. In this work, a different approach was used, namely the mixing of two powders in order to achieve the desired final chemical composition, also known as *in-situ* alloying. Once optimized, this new system would allow the production of smaller batches, particularly important in the first stages of research. The possibility to blend different powders would lead then to important cost and time savings. Indeed, it would no longer require the purchase of unnecessary large stocks of pre-alloyed powders. Research centers and small producers would be able to create their blend with the powder already present in their warehouse, thus reducing in the meantime the supplier's delivery times.

## 1.2 Research Aims

Despite being the reason for its success in the AM sector, the good weldability of Inconel 718 is linked to the  $\gamma''$ -phase which reduces its temperature capability. In recent years, researchers have worked on possible alloy modifications, mainly aiming to improve the maximum application temperature of the alloy while keeping excellent its mechanical performance. Less work has been carried out on room temperature improvements, and more importantly, there is a lack of knowledge as regards the *in-situ* alloying of Inconel 718 by L-PBF technology. The aim of the research was hence to fill this gap in the literature by *in-situ* alloying Inconel 718 with titanium powder in order to enhance the  $\gamma'$  development. Consequently, the research aimed to ascertain the effect which Ti-powder has on the alloy weldability and its homogeneity by characterizing the microstructure and mechanical properties of IN718+Ti. Moreover, unlike the pre-alloyed powders, a blend is intrinsically inhomogeneous and its answer to the laser differs from the former. Therefore, in the first stage of the work, there was the need to create bespoke parameters able to provide samples as dense as in the conventional pre-alloyed condition. Once optimized the printing parameters the

characterization process involved the analysis of pure Inconel 718 and the in-situ alloyed version in three different treated conditions - as-built, solution treated, and both solution treated and double aged. This was necessary to establish the effect that the alloying process had on the microstructure and mechanical properties of the alloy.

### **1.3 Structure of the Thesis**

This thesis is divided into several sections. Chapters 2 and 3 provide a theoretical description of the background of this research work as regards the material characteristic properties and phases, as well as the principles behind the L-PBF process and its possible defects.

Chapter 4 addresses the state-of-the-art of Inconel 718 alloy-modifications to help the reader to get a picture of the possible influence that alloy modifications have on this common alloy.

Chapters 5 and 6 go deeper in the discussion of the method employed and the result achieved. Eventually, in the last section, the conclusion summarizes the work done with a look at the future possibilities linked to this research topic.

## 2 Additive manufacturing

### 2.1 Historical Development

Over the past two centuries, the world has witnessed the birth and the development of the industry. It has passed from the so-called - *Industry 1.0*, through the *2.0*, *3.0* getting to the *4.0* considered the current industrial revolution.

Currently, we are living in a transition period through *Industry 3.0*, characterized by three "dimensions" - volume, variety and, delivery time - towards *Industry 4.0*. In the latter, additive manufacturing has proven to have huge potential. *Industry 4.0* has been leading to technological innovations such as *Internet of Things* (IoT), big data, cloud computing, cyber-physical systems, artificial intelligence, electric vehicles and, 3D-printing.

In a more and more connected world, the interactions among customers, service providers and, suppliers are stronger and more frequent than before. Additive manufacturing may easily fit in this system allowing customers to print their product in closer locations reducing delivery time and warehousing costs. These are the reasons why this technology has the potential to revolutionize traditional manufacturing processes (Yin, Stecke, & Li, 2018).

Additive manufacturing was not the first denomination. It was first denominated *Rapid Prototyping*. The actual first concept of 3D-printing was the *Stereolithography*, concept dated back to the 1970s. Notwithstanding the foregoing, the first attempt will be a few years later when the Japanese Dr. Kodama introduced the layer-by-layer methodology patenting the first rapid prototyping technique and setting the stage for the following SLA. Even though Kodama had already discovered stereolithography, he did not file the patent requirement before the deadline. This is the reason why the visible origins of it will be in 1984 when Charles Hull filed his patent for the *Stereolithography Apparatus* (SLA). In 1986, he co-founded 3D Systems, the first 3D printing company that in 1987 started selling the first SLA printer (Systems, 2020).

Meanwhile, at the University of Texas, Carl Deckard had come up with the idea of using a direct energy beam to melt polymer powders together trying to automate the process. With the help of Dr. Joe Beaman, they developed one of the earliest and most famous forms of 3D printing known as *Selective Laser Sintering* (SLS). The University of Texas at Austin licensed their new technology in 1988 while they launched a startup known as Nova Automation then renamed DTM (Lindstrom, 2020).

During the same years, Dr. Scott Crump filed his patent for *Fusion Deposition Modelling* (FDM) then issued to Stratays Inc. in 1992, of which he was a co-founder.

It was only in the late 90's that the *Selective Laser Melting* (SLM) concept, which can be considered based on the SLS technology, was born.

In about ten years the basis for the main 3D printing technologies was created. Anyway, the gradual expiration of these patents has allowed many newborn companies to improve the technology reducing the production costs. Indeed, 3D printing of real products is still most of the time expensive. Consequently, the technology is mostly used to easily generate prototypes or mock-ups (Rathee, Srivastava, Maheshwari, Kundra, & Siddiquee, 2018; Attaran, 2017; Bensoussan, 2016).

The following years will likely show a strong development in these innovative technologies and a big impact on the whole manufacturing sector and its economy.

While AM is still many times not the most convenient production route, the higher flexibility and design freedom offered by AM has allowed to simplify the industrial supply chain in case of single unit or low-volume production of highly complex components (Pereira, Kennedy, & Potgieter, 2019; Conner et al., 2014).

The future sees Additive Manufacturing evolving more and more from a rapid prototyping condition towards an increasingly reliable *Direct Manufacturing Technology* (Gausemeier, Echterhoff, Kokoschka, & Wall, 2011).

## 2.2 Concept

According to the ASTM definition (Standard, 2012), additive manufacturing is...

*"a process joining materials to make objects from 3D model data, usually layer upon layer, as opposed to subtractive manufacturing technologies".*

Additive manufacturing had long been associated with rapid prototyping (RP). The connection between them stems from the role 3D printing played early on. At that time, additive manufacturing was supposed to reduce the creation time of prototypes. At the beginning of additive manufacturing in the '80s, they were small, in plastic, and non-functional, namely useful just to validate the concept of an idea. The technology has been evolving allowing the production of functional prototypes, semi-finished, and finished products, or even molds and tools for large-scale production. In particular, this latter is called *Rapid Tooling* (Radi & El Hami, 2016).

Nowadays, many materials can be printed. Unlike the beginning, when the feed was only polymeric, today it is possible to print ceramics, glasses, metals and, composites to a certain extent.

All of them have in common the concept - layer upon layer manufacturing. Whether starting from an object or a technical drawing, the process always requires a CAD model for printing, **Fig.1**.

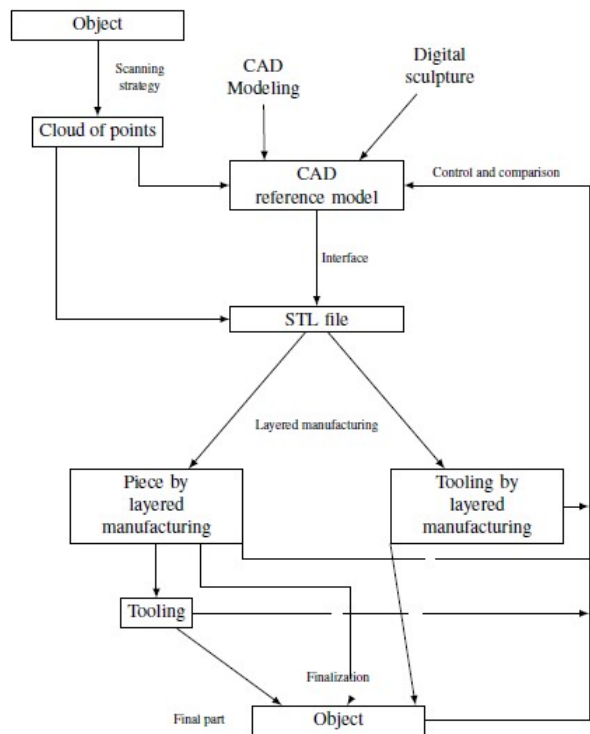


**Figure 1:** Design Process for AM

Once the CAD model is obtained, it has to be transformed in the .stl extension, the most common format for 3D printing. This format derives directly from the stereolithography process although it is often labeled as either *Standard Triangle Language* or *Standard Tessellation Language*.

This format describes the surface of a 3D object without using color and texture. For this reason, if more than one material is about to be used, this format is not advisable. Unlike it, Wavefront Technologies' OBJ (Wavefront OBJect) format allows instead to store other information such as – material and color.

The use of .stl goes hand in hand with the use of a slicer program that allows to communicate with the 3D printing hardware. The .stl format is based on the use of tessellation as in **Fig.2**, which represents the process of tiling the surface with geometrical shapes without overlaps. This method has proved to be a good way to approximate a three-dimensional CAD model in order to transfer it to the printing machine.

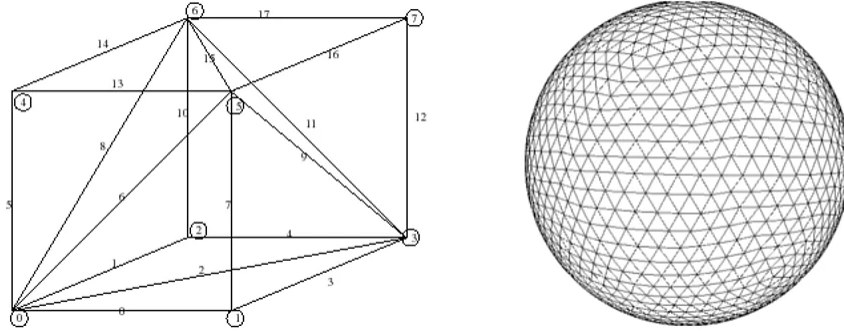


**Figure 2:** Cube and Sphere Tessellation

In the .stl file two main pieces of information about each triangle are saved:

- direction of the normal vector to the triangle surface;
- coordinates of the vertices.

The vector of any triangle always has to point outwards. The more the triangles are, the bigger the file size. This is the reason why during this process any details smaller than the powder bed thickness is removed. Not only would those features be impossible to print, but their presence in the .stl file would make the code uselessly big (Antero, 2018).

Adopting this format, some rules must be followed (Chakravorty, 2020), such as:

<b>Vertex rule</b>	Each triangle must share two vertices with the neighboring triangles
<b>Orientation rule</b>	Each facet orientation must be identified in two ways (right-hand rule)
<b>All positive octant rule</b>	The coordination of the triangle vertices must be all positive

Some programs have been created to check the file looking for possible errors that could make the model not printable. Once the file is checked it can be layered according to the given accuracy.

As far as the metallic components are concerned, not all of the many 3D printing techniques are exploitable. Metallic components share with polymers and ceramics mainly the SLS technology. The four most common AM technologies for metallic production are listed in **Fig. 3**.

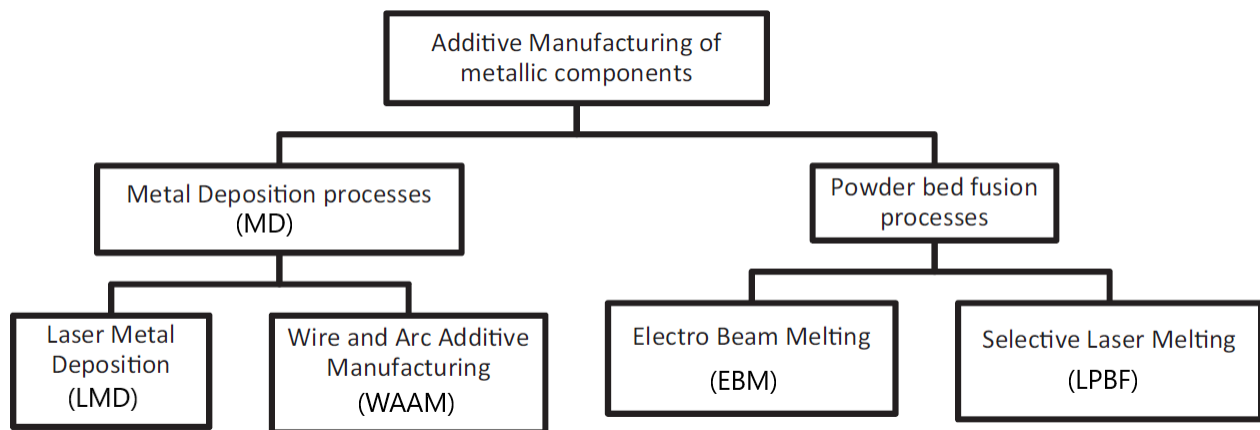


**Figure 3:** Classification of AM Processes Based on Energy Source and Delivery System for Metallic Components (Uriondo et al. (2015))

Despite many advantages, AM owns many constrains. Among them, the impossibility to print overhanging structure without the utilization of adequate supports is perhaps one of the most challenging. Because of this, the literature is full of research projects aiming to reduce the impact of these structures on the printing process.

Supports help to minimize the distortions that would be otherwise generated by the internal stresses induced by the process. Moreover, acting as heat sinks, they increase the overall cooling capacity of the system.

Their presence increases though the waste of material since they have to be removed to get the final component. The need for post processing steps and an increase in material waste make these additional structure not desired. Since they are necessary, during the design of the project a correct orientation of the component must be chosen in order to find a trade-off among costs, production time, and accuracy (Calignano, 2014).

### 2.3 Laser Powder Bed Fusion

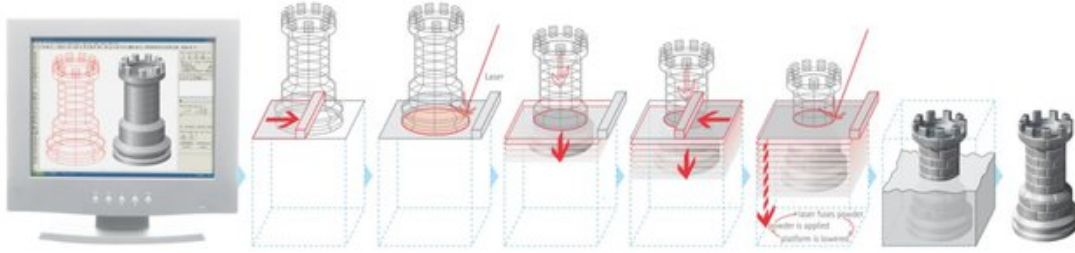


**Figure 4:** Layer-by-layer SLM Concept

*Laser Powder Bed Fusion*, also known as SLM which stands for *Selective Laser Melting*, is a 3D printing technology that enables the creation of complex metallic 3D structures otherwise not achievable through the traditional manufacturing routes.

The process uses a high-energy laser beam to heat the powder to its melting point. It starts layering the powder over a plane known as the *build platform*. By means of a rake or a count-rotating powder leveling roller, the powder is raked across the build area fed from a powder container. Every time a layer is printed, the build platform is lowered by one layer thickness allowing the spreading of new powder.

When it comes to laser additive manufacturing processes, the control of the laser spot takes place through galvanometers. This is a "simple" mechanical control that involves mirrors to deflect the laser over the powder bed. On the contrary, EBM uses magnetic fields to control the electron beam positioning.

Laser Powder Bed Fusion is characterized by a complex system owing to its numerous parameters and based on them the final properties of the printed component change.

The latter may be influenced by:

- Directional or equiaxial grain shape;
- Crystalline texture (cell orientation);
- Presence of hardening phases;
- Presence of deleterious phases;
- Grain size;
- Porosity.

Usually, an LPBF-processed component has yield strength and ultimate tensile strength values higher than the conventional processes. The reason behind it has to be looked for in the cooling

rate of the process. Usually, it can get up to  $10^6$  K/s leading in the Ni-based superalloys to a very fine dendritic/cellular structure often under  $1\mu m$  in size.

As regards those high heating and cooling rates, they induce the so-called super-heating and under-cooling. Consequently, the nucleation rate is enhanced and the grain growth is suppressed leading to the refined microstructure typical of SLM processes (Sun et al., 2017).

Furthermore, a non-equilibrium supersaturated solid solution is created during the formation of the fine microstructure. These two aspects, together with the remaining residual stresses, usually ensure high mechanical properties of the as-built component.

The heat removal follows a direction parallel to the z-axis. This stands from the fact that the heat conductivity of the bulk material is greater than both the powder feedstock and the gas in the printing chamber. Therefore, most of the heat is dissipated along the building direction by the underneath just-printed material. This mechanism brings a columnar structure and is also one of the reason behind the anisotropy of LPBF-processed structures.

This structure might not be recommendable for some applications that may require isotropy. In this case, heat treatments have to be considered, not only in order to get a more equiaxial structure but to homogenize the entire composition.

Even though the additive process has many advantages, it is far from being free of downsides. In some cases, the aforementioned anisotropy and the segregation may be considered two of them. The bigger the atom the slower its thermal diffusion. This phenomenon is described by the coefficient of segregation typical of each element and that help to predict the more or less high tendency of each atom to segregate.

The LPBF-processed sample in the as-built condition are indeed characterized by segregation mostly of the heaviest elements among the branches of the dendrites causing several issues such as the nucleation of deleterious phases.

### **2.3.1 Powder Feedstock**

As the process name says, the powder bed fusion processes is part of the family of powder bed processes. The layer-by-layer methodology sees the continuous laying of powder layers then selectively melted and re-covered by another powder layer up to the end of the printing step.

All those processes usually have a feedstock made by spherical powders derived from several fabrication processes. Rough classifications of these powders are gas atomized (GA), plasma rotating electro processed (PREP), plasma wire atomized (PWA), electrode induction melting gas atomized (EIGA) and plasma atomized (PA). Yet, powders are classified based on morphology, size distribution, and as regards the gas atomized, even based on the gas used during the atomization process - argon or nitrogen atomized.

PBF processes can rely on all these aforementioned sources of feedstock. All of them provide spherical powders but with different characteristics. Different fabrication routes might have slightly different outcomes concerning, for instance, satellites or gas porosity. The former refers to fine particles stuck to large ones, which cause a reduction in flowability of the considered powder. As

regards the latter, it is a common belief that gas porosity in the powder is transferred to the final component. Therefore, the feedstock has to be carefully chosen taking into consideration these crucial aspects.

One of the biggest advantages of additive manufacturing is the utilization of powder feedstocks. They allow to highly reduce the waste of material and the costs for complex components. Powder reuse is a key factor to establish a cost-effective business but it has some drawbacks.

The powder reuse is sensible to some troubles such as contamination from laser exposure or variations in PSD (Powder Size Distribution), powder chemistry, morphology, apparent density, and flowability. Recycling powders leads to an increase in average size. It is probably due to some ejecta that are smaller than the sieve mesh but larger in average size. They can be by-products of phenomena such as melt pool ejection over not welded powder (Ott et al., 2018).

In the figure below, some of these aspects are highlighted such as the fusion of several particles, their breakup as well as the development of superficial cracks. These phenomena are caused by the thermal cycling to which the powders have to undergo during the printing process. They represent a general framework that must be particularly taken into account when considering the reuse of powders in highly regulated AM applications such as medical devices and aerospace sectors.

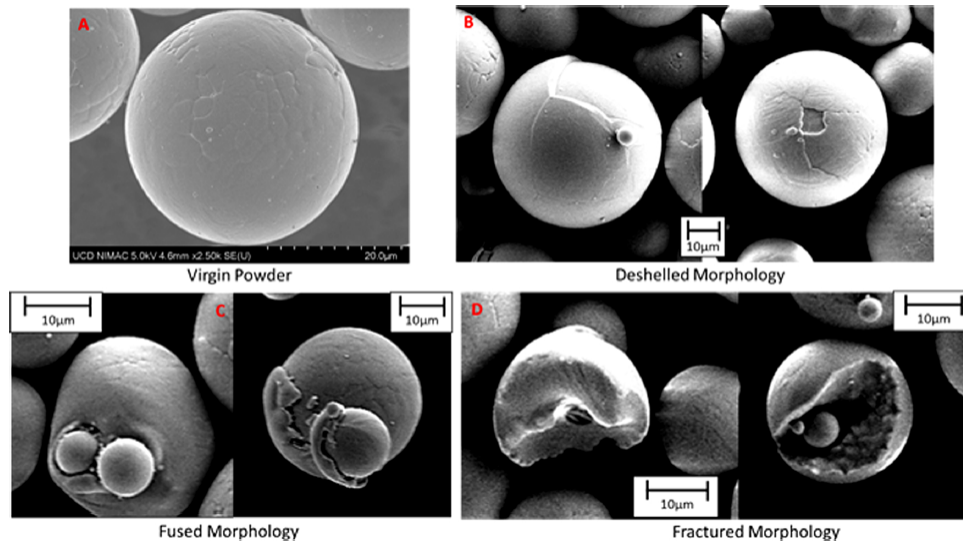


**Figure 5:** Development of Powder Defects After SLM Processing of a Ti6Al4V Powder Feedstock (Keaveney et al. (2020)).

### 2.3.2 Parameters

This technology has been characterized by mainly a series of parameters such as laser power, scanning rate, hatching space, and layer thickness. Considering these parameters, it is typically investigated how they impact surface quality, internal porosity and mechanical properties of the

final component.

These studies have allowed the comprehension of the influence that the energy density provided to the powder bed has on the melt pool geometry and, consequently on the final structure.

**Energy Density** This parameter is often used to calculate the amount of energy provided to the powder bed. There are several definitions of it, some of them referring to a unit volume (VED), others either to unit surface or line energy density (LED). As shown by equation (1), it connects scanning speed, hatching distance, layer thickness, and laser power.

$$E_d = \frac{P}{v \cdot h} \quad (1)$$

$$VED = \frac{P}{v \cdot h \cdot t} \quad (2)$$

$$LED = \frac{P}{v} \quad (3)$$

$E_d$ ,  $P$ ,  $v$ ,  $h$ , and  $t$  respectively surface energy density, laser power, scanning rate, hatching distance, and layer thickness. Parameters help to consolidate a printing process, for instance when the printing machine has to work with a new powder composition. In this case, it is useful to relate the amount of energy supplied to the powder bed, with the porosity of the final component as a function of the parameters set.

**Hatch Spacing** All of them play an important role in the process outcomes. For instance, increasing the power or decreasing the scanning rate are two ways useful to achieve more significant melt pool widths and depths.

Hatching distance can be considered as the distance between the center of two consequent scanned stripes.

As part of the Energy Density in **eq.2**, the hatching spacing can influence the amount of energy provided to the powder bed (Metelkova et al., 2018). In order to achieve a proper metallic bonding among two consequent stripes, each time the laser scans a new line it has to melt both new powder and part of the previous line. This is ensured by the setting of a proper hatching distance which has to be smaller than the generated melt pool.

The chosen value can strongly affect the final mechanical properties of the component. Too wide hatching distance causes the generation of porosity because part of the powder does not absorb enough energy to melt. This is visible in **Fig.6b**, the blue regions are the volume of powder supplied with enough energy to melt. Unlike them, the regions indicated as "pore" are not directly affected

by the laser. In those regions the heat will be provided only by the thermal diffusion coming from the melt pools. Likely, this latter will not be enough to cause a complete melting of the powder and therefore generating *inter-track porosity* (Pei et al., 2017).

A proper hatching spacing generates overlap among consequent scanned lines allowing each line to absorb part of the heat of the following track. This enable its partial remelting which fills the inter-track space providing a fully dense product.

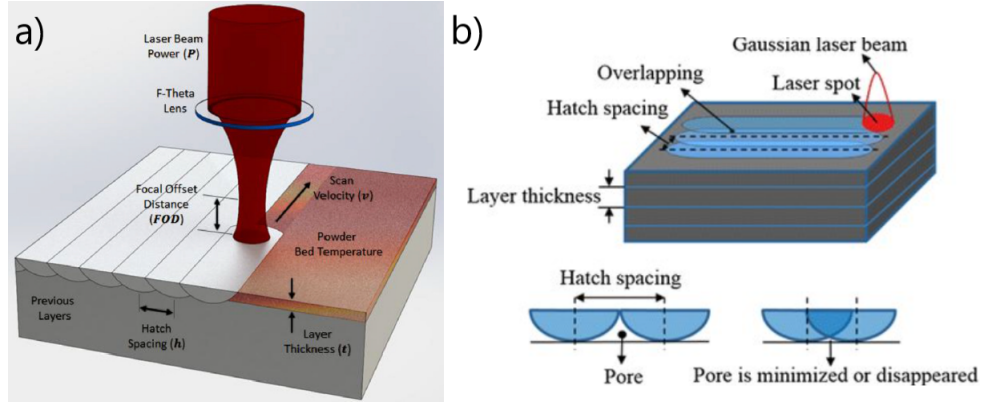


**Figure 6:** L-PBF process parameters (Shipley et al. (2018); Pei et al. (2017)).

**Layer Thickness** According to **eq.2**, the layer thickness directly affects the energy density provided to the powder bed. An increase in layer thickness reduces the volumetric energy density. This causes the molten pool peak temperature to be lower as well as its viscosity (and therefore weak flowability). Furthermore, a thicker layer thickness will bring to enlargement of the tracks while reducing the contact area of the molten pool with the underlying substrate. Without the necessary contact surface between the molten pool and the underlying substrate, the surface tension on the molten metal will cause it to break up into balls causing balling (R. Li, Liu, Shi, Wang, & Jiang, 2012). Lower molten pool temperature, lower viscosity, and smaller contact area increase the likelihood of balling and to develop porosity in the final component.

As far as the laser powder bed melting of metals is concerned, the typical layer thickness ranges from  $20\mu\text{m}$  up to  $50\mu\text{m}$  (Shi et al., 2016; Nguyen et al., 2018).

**Laser Spot size** These last years a new strategy has been implemented, the *Laser Defocusing*.

By defocusing is meant the relative vertical position of the laser focus with respect to the powder surface. It can be considered as a parameter to change the energy density at which the surface will be exposed, equation (4).

$$E_d = \frac{P}{v \cdot d_{spot}} \quad (4)$$

Keeping constant laser power and layer thickness, working at the laser focus means to have the smallest spot size ( $d_{spot}$ ) and the highest energy density with all the associated advantages and disadvantages.

The defocusing is generally achieved by moving the printing platform either upwards or downwards. Either way, it causes the spot size to increase and the surface energy density to decrease according to equation (4) (Metelkova et al., 2018).

While printing, it is important to be able to find the correct trade-off between productivity and good surface quality of the final component. The former can be achieved working with a larger spot size which increases the scanned surface per unit time. However, increasing the spot size causes surface quality to decrease.

Some studies propose the adoption of two lasers using the so-called *hull-core* strategy that makes use of two different laser setups. One for the skin using smaller spot size and another one with bigger spot size and consequently bigger productivity. The advantage of this is to allow increasing productivity while keeping under control the surface quality constraints.

So far, a few are the machines having more than one laser. Defocusing is a good solution which allows to get the same result without requiring two lasers. In this case, variations in spot size can be then accomplished by focal shift (Metelkova et al., 2018).

Equation (5) shows the dependence of the spot size by the building surface position along the z-axis.

$$\sigma = \sigma_0 \sqrt{1 + \left(\frac{z - z_0}{z_r}\right)^2} \quad (5)$$

Where  $\sigma$  is the spot size,  $\sigma_0$  the waist (minimum beam spot size),  $z_r$  the Rayleigh length,  $z$  and  $z_0$  the powder bed and the laser focal point positions along the z-axis, respectively.

The Rayleigh length represents the distance from the laser focal point on the z-axis in which the spot surface is twice the surface in the laser focus.

The defocusing can play a role in the final achievable microstructure. Keeping constant the hatching space and varying the laser spot size (defocusing) changes the overlap between consecutive lines and therefore the remelting process as well. Less overlap leads to less remelting of the previous stripe and fewer opportunities for epitaxial growth. This is directly connected with a final structure more "equiaxed" (Kantzios et al., 2019).

### 2.3.3 Protective Gas

All the L-PBF processes requires a protective gas to be used. The protective gas has many essential functions. Among them, it reduces the powder oxidation and removes airborne by-products due to the melting process.

The amount of oxygen in the chamber has to be carefully kept under control. Reacting with the melt pool, it causes the creation of oxides that then act as inclusions in the final component. Nitrogen, argon or helium can be used as shielding gas. Despite of that, the different size of their atoms provides them with different heat conductivity which can lead to different cooling rates and microstructures. The most common shield gas is though argon with maximum oxygen partial pressure of 0.10% (Bean, Witkin, McLouth, & Zaldivar, 2020).

The influence of the protective gas on the printing process is not negligible mainly when considering the defocusing process. Variation in the platform position may bring with it some issues such as the not complete removal of the by-products derived from the laser melting. Those by-products if not thoroughly removed can interact with the laser or re-condensate on the surface becoming a problem for the layer that will be printed above, **Fig.7**. These condensed by-products can indeed reduce the remelting of the layer, carried out by the scanning of the layers above. Airborne by-products might indeed absorb the laser energy and scatter the beam (Bean, Witkin, McLouth, Patel, & Zaldivar, 2018; Keaveney et al., 2020).

The consequence can be a higher level of porosity as well as worse mechanical properties of the as-manufactured item.

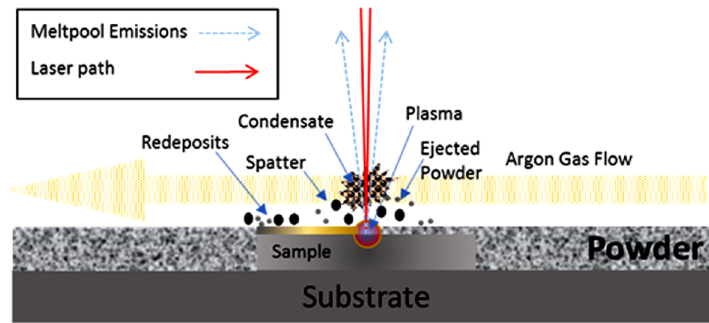


**Figure 7:** By-Products Typical of SLM Processing (Keaveney et al. (2020))

### 2.3.4 Scanning strategy

The scanning strategy has a substantial impact on densification and internal stress distribution in the as-manufactured component. As well known, the SLM process is characterized by anisotropic outcomes. It stems from the direction of heat removal which is preferentially oriented along the building direction. The internal stresses in the building direction are much lower than the ones in the scanning direction. In turn, the longer the scan track, the greater the stresses in the latter direction. Consequently, shortening the scanning track and adopting a proper hatching angle between consecutive layers can be a good solution to increase the isotropy and alleviate the internal stresses.

In order to "tune" texture, isotropy and internal stresses, several scanning strategies can be adopted such as - island/checkerboard, stripes (paintbrush), meander or spiral scanning (Rajendran et al., 2020; Jhabvala, Boillat, Antignac, & Glardon, 2010).

All of these patterns have both advantages and drawbacks. Since many defects are caused by inhomogeneous thermal gradients developed inside the component while printing, the aim is to decrease them as much as possible.

Scanning strategy strongly affects microstructure orientation, pore distribution and crack formation, the choice of which one to use is not accidental. Depending on the cross-section characteristics of the component, one may be better than others. As previously said, longer the scan track, the higher the internal stresses. Hence, the meander mode is ideal for thin walls while stripe pattern might be better for thicker parts.

Regarding checkerboard and island patterns, they are actually the same thing with the exception that the latter is a random version of the former. In the island pattern, the surface area is divided in squares then printed randomly without particular order.

As shown in **Fig.8**, checkerboard and paintbrush can be seen as a scaling down of the common parallel strategy. Temperature inhomogeneities such as overheating and thermal gradients are mitigated because of the different thermal dynamics.

In both cases the areas to consolidate are smaller and this improves the temperature homogeneity (Jhabvala et al., 2010).

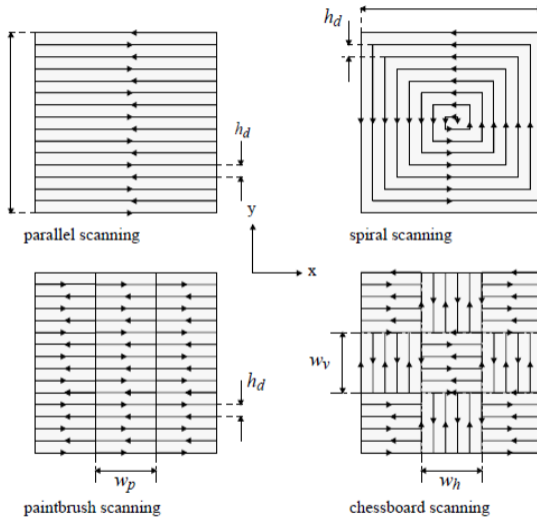


**Figure 8:** Scanning Strategies

Anyway, the machine user is not forced to use only one of them. Hull-core strategies may be adopted. For instance, the contour might be scanned with the use of a continuous line, then the core of the cross-section with a stripe pattern. This can be useful if the user has to satisfy particular surface smoothness constrains.

### 2.3.5 Possible Drawbacks

Selective laser melting has proved to be a challenging process as far as its many parameters are concerned. This so high number of variables causes many problems to arise but it can be solved working on the interaction among those parameters.

Whether for an incorrect configuration or for other reasons, it is difficult to get a process free of defects. This section aims to clarify the basis behind those defects, trying to highlight how they affect the process outcomes.

**Balling and Keyhole modes** They are deleterious conditions that may occur if the parameters are not set correctly. They are commonly related to incorrect scanning rate or energy density on the powder bed.

As far as the *keyhole mode* is concerned, it can generate porosity in the final component when the scanning rate scanning rate is low and the laser power is high, hence for high VED values. Several researchers have highlighted the reliability of the *Normalized Enthalpy* as a method to predict the keyhole threshold, equation (6). This refers to the condition beyond which the laser melting mode changes from conduction mode to keyhole mode (Metelkova et al., 2018).

$$\frac{\Delta H}{h_s} = \frac{A \cdot P}{\pi \cdot h_s \cdot \sqrt{D \cdot v \cdot d_{spot}^3}} [-] \quad (6)$$

$$h_s = c_p \cdot \rho \cdot (T_m - T_0) \left[ \frac{J}{m^3} \right] \quad (7)$$

With absorptivity  $A$ , enthalpy at melting  $h_s$ , thermal diffusivity  $D$ , specific heat capacity  $c_p$ , density  $\rho$ , melting temperature  $T_m$  and initial temperature prior to melting  $T_0$ .

The interesting aspect of the normalized enthalpy is that, if plotted versus the ratio between melt pool depth and laser spot size ( $d_{MP}/d_{spot}$ ), they show a linear relation. So, it becomes a way to separate the keyholes-mode data from the conduction-mode ones. This helps to set up the correct parameters, avoiding to hit the powder bed surface with an excessive energy density.

In the keyhole-mode the energy density is sufficient to cause the evaporation of the metal and the creation of plasma. This latter enhances the laser energy absorption and enables the laser to penetrate deeper into the material, more than the conduction-mode does.

Once the laser passed over, the incomplete collapse of some of these cavities can leave voids in the wake of the laser beam (King et al., 2014).

The porosity left from the keyhole mode is characterized by a small spherical shape. As aforementioned, the normalized enthalpy and the volumetric energy density (VED) can be used to forecast the keyhole threshold. Once a specific energy density value is exceeded, the keyhole-mode will increase in intensity and will have an increasing influence on the porosity level.

Some researchers found that keyhole porosity could be confused with another phenomenon on which research is still being carried out. It was found that sometimes plotting the porosity level against the energy density, even increasing the energy density, the porosity does not change for a range of values. If that porosity were due to the keyhole mode, increasing the energy density should increase the level of porosity, too. Since this was not happening, this condition is not considered being associated with the keyhole-mode but instead to be a direct consequence of the shield gas being trapped in the molten pool. This latter causes a porosity easily confused with the keyhole-like one (Kumar et al., 2019).

This means that in the conduction-mode the sample could be affected by porosity even though the "energy condition" should not promote it.

While for keyhole high power and/or low scanning rate are considered as main causes; regarding the *balling* the opposite situation takes place. This phenomenon is often related to high scanning rate and/or low laser power, either way according to the equation (1) both the situations involve low energy density.

However, several reasons have been attributed to the *balling* phenomenon (Sun et al., 2017), such as:

- hydrodynamic instability driven by *Maragoni Effect*
- capillary instability of the melt pool
- splashing of the melt pool as a result of its high surface temperature
- reduction in the wettability because of the high oxygen content in the atmosphere
- rapid solidification before the melt is properly spread (worse in case of high thermal conductive materials)
- lack of contact between molten powders and substrate because of insufficient melting of the latter.

This phenomenon comes in the form of spheres of molten metal. The system evolves from a straight track into balls in order to reduce the surface free energy. It is usually divided into two types (R. Li et al., 2012): ellipsoidal and spherical. The former is characterized by a particle size of 500  $\mu m$  whereas the latter of roughly 10  $\mu m$ . The latter is smaller and does not represent a problem for the quality of the process outcomes. Unlike the latter, being bigger the former can represent a severe problem not only for the final quality but for the process itself, too. In some cases, it hinders the roller sliding while laying the powder bed.

Therefore, the main issues connected with balling can be summarized as follows:

- Increasing in surface roughness, the printed components will have to undergo a polishing treatment;
- The products of balling can prevent metal powder from absorbing the laser energy thus generating porosity;
- Severe balling can hinder the distribution of the powder bed by the paving roller or re-coater blade.

As previously mentioned, the latter may bring serious damage to the printed component. This does not happen as long as only the small-sized balling takes place. Unlike it, big ellipsoidal particles cause the final surface to be rougher and the generation of stress between the surface affected by balling and the re-coater. If the friction is high enough, those stresses may break the printed part. This is the reason why, in the case of severe balling the process has to be stopped.

Even though the balling is often associated with laser power and scanning rate, some other parameters can influence its presence. In the aforementioned study the researchers highlighted the influence of the oxygen. This gas can be a serious problem when the process works with powder sensible to it. Too high partial pressure of oxygen causes the oxidation of the melt pool accordingly reducing the wetting ability of the surface because of the thin oxide layer generated, thus promoting balling.

A correct choice of the layer thickness is important as well. It has a pronounced effect on the balling initiation. A thicker thickness will cause a worse wetting ability of the melt pool since the energy in unit volume absorbed by the powder is insufficient. Less absorbed energy is therefore directly connected with lower molten pool temperature, low flow ability and balling.

Balling can be achieved as consequence of an increment of scanning rate at constant VED. Increasing the scanning rate decrease the dwelling time of the laser, meant as the time of which each point is subjected to the laser beam. If this time decreases, the maximum temperature of the melt pool achieved is lower as well, leading to higher viscosity of the molten metal, open-pores and limited relative density.

As described by the reference (Jia & Gu, 2014), the physical threshold after which balling takes place depends on the laser characteristic as well. Under this point of view, the melt pool is stable as long as the laser wavelength is  $\lambda < \pi D$ , with  $D$  as the diameter of the unperturbed liquid cylinder, namely the cylindrical approximation of a fully stable melt pool. Rising the scanning rate at constant  $\lambda$  will decrease the  $D$  connected to the stable pool up to the point at which the aforementioned relation will be no longer valid.

The track diameter decreases because of the molten pool viscosity and the need of the system to decrease as much as possible the surface free energy. Soon or later, the cylindrical shape no longer allows the system to reduce it. At that point, balling takes place splitting the track into "balls".

However, balling must be avoided and to some extent a solution to the problem is the remelting. The laser does a second scan over the just melted layer. It helps to mitigate the balling phenomenon and increase final density and surface quality, as well.

**Spattering** Spattering is due to overheating of the melt pool. It is usually associated with high values of energy density that cause the melt evaporation (ScienceVio, 2018; Leung et al., 2018). The so created gas causes a recoil pressure that expels the molten metal together with non-melted powder particles around the melt pool.

These large expelled particles are known as satellites. They are spherical in shape and can be bigger than the feed powder. Not only is this process deleterious for the final component, but it can lead to the oxidation of the most volatile elements leading to oxide inclusions in the final component.

Spattering like balling, keyhole and so on, causes porosity inside the final component and for this reason has to be avoided as much as possible (Sun et al., 2017).

**Process Efficiency** The process efficiency is a criteria useful to evaluate the printing process, better associated with the productivity rather than the quality of the process itself. The process efficiency increases the higher is the volume of powder processed per unit time. This would require either thicker powder bed layer or higher scanning rates.

When it comes to industrial applications it can represent a problem. Industrial sectors usually aim to get as good as possible mechanical properties in the final component along with high productivity and the least amount of necessary post-processing treatments. Indeed, the higher the number of components printed, the lower the final price. This is important since the main challenge that hinders metal-AM to become a mainstream of manufacturing technology is still its price.

However, the satisfaction of those requirements might represent a problem as far as mechanical properties and surface resolution are concerned. High scanning rate can be source of troubles, such as balling and therefore porosity, surface roughness, etc. In order to achieve a greater process efficiency, it must therefore be found a trade-off between productivity and quality of the process outcomes (Kumar et al., 2019).

In the last years some new technologies are setting the stage for the next generation of L-PBF technology. Among all the improvements, multiple lasers and multiple processed layers seem to be promising. Both of them aim to increase the process efficiency leading to lowering of the overall price of the process (Khorasani, Gibson, Veetil, & Ghasemi, 2020).

Wong et al. demonstrated the utilization of four lasers in the same time in a configuration called - "single multi-mode" (SM-L-PBF). It has the capability to increase the process throughput up to almost 3 times compared to the single laser configuration. This without affecting the mechanical properties of the final component (Wong et al., 2019).

Perhaps, the biggest leap forward has been made by *Aurora Labs* which introduced the Multi-layer Concurrent Printing (MCP) (Labs, 2019). This is part of the Rapid Manufacturing Technologies (RMT) and consists in laying down powder at different levels by means of a particular rake made of multiple powder hoppers. This allows the system to operate at several levels at the same time actually printing multiple layers simultaneously. This feature strongly increases the printing speed proportionally to the number of hoppers the rake is made up of, currently between 30 up to 100. The number of total sweeps needed to complete the component drastically decreases and

consequently its price. Their latest developed machine, called RMP1, demonstrated a print speed of 350 Kg/day but the company hopes to soon obtain speeds as high as a ton per day (Labs, 2019).

Similar developments will soon enable the printing of components at a cost competitive with traditional manufacturing.

**Anisotropy** As far as the as-built condition is concerned, a vertically printed sample always has different mechanical properties from a horizontally printed one. Those properties mainly refer to UTS, yield strength and, ductility.

There are several reasons behind this anisotropic mechanical behaviour. The heat generated by the molten pool is removed mainly along the building direction, from the molten pool towards the platform. The thermal conductivity of either the platform or the already processed underlying layers is indeed bigger than both the gas in the printing chamber and the surrounding loose powder.

Anyway, the heat flow direction is not necessarily perfectly aligned to the building direction. The phenomenon is more complicated since it can be strongly influenced by thermal fields, scanning parameters and convection inside the melt pool.

Consequently, according to some researchers a SLM printed FCC-materials (such as the super-alloys) show strong texturing along  $\langle 001 \rangle$  parallel to the building direction. In the meantime, others have stated the presence of relatively isotropic crystallographic orientation.

Nonetheless, previously mentioned anisotropy of the mechanical properties have been commonly reported as different in both textured and non-textured conditions. UTS and yield strength are usually higher along the direction perpendicular to the BD, while the ductility has an opposite trend.

During solidification, the melt pool tends to shrink. The underlying layer prevents this from happening. Consequently compressive forces are created in the material underneath the melt pool, which instead undergoes tensile stresses. This does not happen in the vertical direction where there are almost zero constrains from the already printed material.

Another aspect to take into account is that, the further you go from the base plate the lower cooling rate you get. This leads to the development of less strong internal stresses in the building direction.

Therefore, in a horizontally built sample much higher internal stresses will be created if compared with the same component printed vertically.

Internal stresses are partially converted into dislocations and plastic deformation which act as work-hardening to strengthen the material. Even though in the as-manufactured condition the difference in mechanical properties can be attributed to different crystallographic orientations, the bigger influence derives from the different amount of residual stress between the vertically and horizontally oriented sample.

However, despite the fact these differences may persist, they can be strongly mitigated if the printed component undergoes heat treatments such as homogenization. As a matter of fact, this

latter removes all the residual stresses still present in the as-manufactured form (Deng et al., 2018).

### 3 Ni-base superalloys for 3D printing

Nickel-based superalloys have an outstanding combination of corrosion resistance, toughness and high-temperature strength. Features required by aero-engines which seek high temperature structural material for high-pressure turbines (HPT) or rocket engines. In those sectors, Ni-base superalloys are used for disks, blades and many other applications where the components must undergo extreme conditions.

Despite this, they usually have a big drawback that is the high density, usually between 8 and 9 g/cm<sup>3</sup> (Perrut et al., 2018). In the aeronautic sector keeping the structures lightweight is really important. Lightness means less engine energy consumption and hence less greenhouse gasses emission as well. A way to achieve that is to substitute the Ni-based superalloys with other materials, as in the way TiAl alloys have done in the low-pressure turbines (LPT) where the conditions are not as extreme as in the HPTs. In the latter, the combination of harsh environment, complex mechanical stresses, the corrosive and oxidizing environment at high temperature make Ni-base superalloys irreplaceable.

Nevertheless, lightweight structures can be achieved even with these heavy materials making use of more efficient designs. The necessity of complex geometry thin-walled components made it difficult to produce them through the traditional routes. Unlike other alloys, superalloys are much more difficult to work with. Both milling and CNC machines have serious difficulties working with these precipitation hardened materials.

The solution ended up being additive manufacturing. The process which allows to create complex lightweight structures reducing waste of material and design-to-component time in the meanwhile.

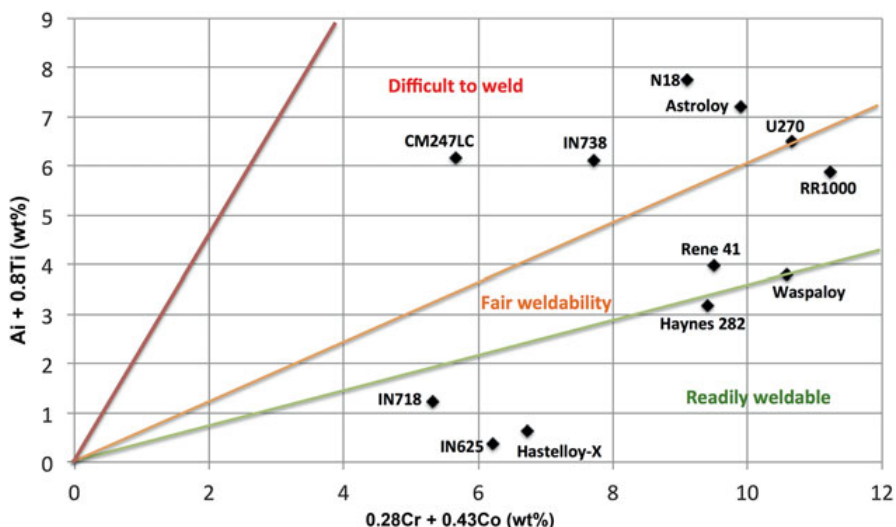


**Figure 9:** Weldability Assessment Diagrams for Ni-base Superalloys Depending on the Chemical Composition (Attallah et al. (2016))

When it comes to additive manufacturing the weldability of an alloy is an important parameter. Since most of the influence on this property is brought by relatively few elements such as Al, Ti, Cr, and Co (Henderson et al., 2004; Catchpole-Smith et al., 2017); graphs as in **Fig.9** have been created as common way to characterize the Ni-based superalloys based on their weldability. As highlighted, taking count of the weight fraction of those elements is possible to identify three regions - *Readily Weldable*, *Fairly Weldable*, and *Difficult to weld* (Attallah et al., 2016).

Despite the **Fig.9** which shows several readily weldable alloys, the Ni-base superalloys are well-known to be difficult to weld. Just a small number of superalloys is actually easy to weld.

The biggest concern about additive manufacturing of precipitation-hardenable Ni-based superalloys is their tendency to crack. During the welding process and the following quick cooling, internal stresses are generated and if they overpass the strength at break the component will not withstand the process.

The behaviour during conventional welding is well known and it might occur in the form of hot tearing, ductility-dip cracking or liquation cracking. Yet, it might occur in the post welding heat treatment (PWHT) as strain-age cracking (SAC). According to the intrinsic resemblances with the welding processes, the SLM is subject to all of them to some degree (Carter et al., 2012).

Hot Tearing, also known as *Solidification Cracking* it occurs in the mushy zone created by the solidifying melt pool, a volume of biphasic material having coexisting solid and liquid metal. During the rapid solidification the dendrite formation hampers the liquid flow in the interdendritic regions. Given the high stresses generated during the L-PBF process those remaining interdendritic regions can act as crack initiation points.

As regards the liquation cracking, despite the name, it actually occurs in the already solidified zone. Usually, it affects areas far from the melt pool but in which the metal is rapidly heated up to a high temperature, close but not over the liquidation temperature of the material. This fast heating causes the melting of some phases in the grain boundary such as low melting point carbides or  $\gamma$ - $\gamma'$  eutectics. So, the high residual stress generated by laser melting can make the liquid metal act as a crack initiator.

Different is the strain age cracking which is very common in the additive manufacturing processes. As known, the L-PBF consists of the melting of continuously deposited layers of powder. This process intrinsically leads to the reheating of the previous melted layer underneath the last processed one. This phenomenon may cause the  $\gamma'$  precipitation and hence strengthen the material. The process of reheating involves two aspects - on the one hand the material reheating allows stress relieving, on the other hand the aforementioned precipitation. If the latter has higher kinetics than the former, the strengthening of the material and the accumulated stresses may lead to the generation of strains. If these exceeded the ductility of the material, cracks would therefore generate preferentially at the grain boundaries, often with carbides acting as crack initiation points (Carter et al., 2012; Bourell et al., 2017).

Since the introduction of metals in additive manufacturing, the weldability has been therefore considered as an indication to processability by L-PBF. As depicted in the **Fig.9** not all the Ni-base superalloys are exploitable. IN 718, Waspalloy, IN625, Hastelloy-X and all the alloys laying in the "Readily Weldable" may have some applications in the additive manufacturing sector.

There is no doubt that the chemical composition of the alloy is an important aspect which strongly influences the proneness to AM applications.

When it comes to metallic-AM, an alloy is considered as proper for this kind of applications not only if it owns good weldability. As regards the L-PBF process is concerned affinity to the atmosphere components, reflectivity and conductivity have to be taken into account. The influence of the composition over all this aspect has made Inconel 718 and 625 two of the most used Ni-based superalloys in L-PBF process.

The purpose of this chapter is to give a basis on their features as regards the chemical composition and the phases generated as result of heat treatments.

### 3.1 *Inconel 718*

Inconel 718 is a common Ni-based (Ni-Cr-Fe) austenite ( $\gamma$ ) superalloy, material of choice for high temperature applications because of its high temperature strength and corrosion resistance. Inconel 718 is widely used in the additive manufacturing sector.

This alloy is strengthened through solid solution and aging treatments that promote the formation of different precipitates inside the austenitic matrix. More in detail, dispersion of fine-scale precipitates of intermetallics ( $\gamma'$  and  $\gamma''$ ) or other phases like carbides (mainly NbC) and nitrides in the austenitic fcc Ni matrix known as  $\gamma$  phase.

$\gamma''$  ( $\text{Ni}_3\text{Nb}$ ) is the inconel 718 main strengthening phase whereas  $\gamma'$ ( $\text{Ni}_3(\text{Al,Ti})$ ) is present in lower volume fraction.

High values of  $\gamma'$  would make the alloy strong but prone to cracking generation during welding and unsuitable for L-PBF purposes. Contrary, the high content of  $\gamma''$  is the reason why this alloy has been one of the best Ni-based alloys for the L-PBS process.

The presence of this phase can though be influenced by the thermal history of the sample. The main  $\gamma''$ -former element Nb is depleted by several other phases or mechanisms such as segregation, carbides and to some extent  $\gamma'$ . Like other elements, Nb tends to segregate and in such segregations it reacts generating carbides. These phases have a high melting point and, both if generated due to the segregation process or to heat treatments, remove available Nb from the matrix. The decrease in niobium content in the matrix reduces the precipitation of  $\gamma''$  during aging affecting the overall mechanical properties of the alloy.

Unlike  $\gamma'$ ,  $\gamma''$  is metastable and if exposed for long time at temperature around 700°C, it tends to coarsen and to transform into the stable incoherent  $\delta$  phase ( $\text{Ni}_3\text{Nb}$ ) (Oradei-Basile & Radavich, 1991; Azadian, Wei, & Warren, 2004). This can be a problem considering that at that temperature this transformation happens after only  $\sim 50$  hours which drop down to  $\sim 1$  hour if exposed at 800°C (Mignanelli, Jones, Hardy, & Stone, 2018). Due to its structure, it tends to reduce the ductility of the alloy. However, it can slightly increase the creep performance if precipitated in small amount at the grain boundary acting as pinning points and reducing the grain boundary creep fracture (Deng et al., 2018).

Being the additive manufacturing characterized by high cooling rate, the segregation affects

more the elements with low diffusion coefficients causing the formation of deleterious phases and uneven chemical composition.

**Table 1:** Inconel 718 Chemical Composition

Ni(plus Co)	Cr	Fe	Nb( plus Ta)	Mo
50.00 - 55.00	17.00 - 21.00	Bal.	4.75 - 5.50	2.80 - 3.30
Ti	Al	Co	C	Mg
0.65 - 1.15	0.20 - 0.80	1.00 max	0.08 max	0.35 max
Si	P	S	B	Cu
0.35 max	0.015 max	0.015 max	0.006 max	0.30 max

**Table 2:** Inconel 718 Principal Phases

Phase	Crystal structure	Chemical formula
$\gamma$	fcc	Ni
$\gamma''$	bct (ordered $D0_{22}$ )	$Ni_3Nb$
$\gamma'$	fcc (ordered $L1_2$ )	$Ni_3(Al, Ti)$
$\delta$	orthorombic (ordered $D0_a$ )	$Ni_3Nb$
MC	cubic $B_1$	(Nb,Ti)C
Laves	hexagonal $C_{14}$	$(Ni, Fe, Cr)_2(Nb, Mo, Ti)$

In the previous **Table 1** and **Table 2** (Deng, 2018), both the composition range and the main phases of the Inconel 718 are given. It can be seen as giving the high content of iron, this alloy is sometimes classified as iron-nickel based superalloy. Among other aspects, the content of Fe contributes to make lower the price of this alloy. Indeed, IN718 is characterized by being relatively cheap if compared to other Ni-base superalloys.

Since the composition plays an important role on the final properties of the components, whatever type you talk about, **Table 3** is an overview of the influence elements have on Ni-base materials while **Fig.10** shows those typical elements together with the beneficial and deleterious ones.

These aspects do not concern only Inconel 718 but they can be considered general throughout the Ni-base superalloys sector (Deng, 2018).

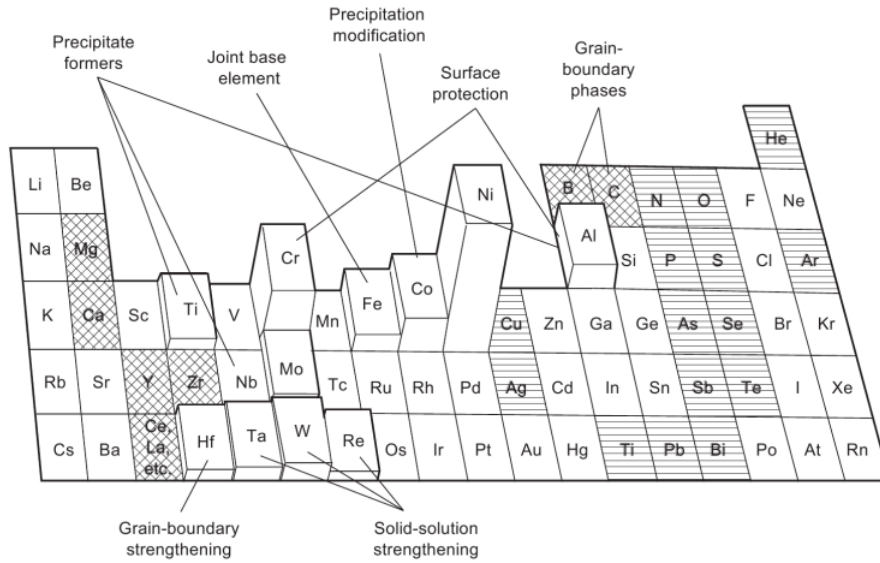


**Figure 10:** Alloying Elements used in Ni-based Superalloys. Beneficial Trace Element are Indicated with Crossing Lines Whereas Deleterious Trace Elements with Horizontal Lines. The height of each block indicates the proportion in which they are usually present (Davis et al. (2000)).

**Table 3:** Elements Influence

<i>Elements- Influence on properties</i>	
<b>Fe</b>	Solid-solution strengthener which changes the solidification range of Inconel 625. In particular, less iron in the alloy composition leads to smaller solidification range and variations in the microstructure as well. It causes the grains to grow smaller and the tensile strength to be higher than in the more Fe-rich samples (Marchese et al., 2020).
<b>Nb,Mo</b>	High tendency to the interdendritic segregation where both of them take part to the creation of deleterious phases like Laves phase. Among other things, Nb contributes to the nucleation of other phases such as $\delta$ , $\gamma''$ or MC and $M_6C$ carbides. Both Nb and Mo are then solid-solution strengtheners.
<b>Cr</b>	Solid-solution strengthener, $M_7C_3$ and $M_{23}C_6$ carbides former, improve oxidation and corrosion resistance.
<b>Co</b>	Solid-solution strengthener, raises solvus temperature of $\gamma' Ni_3(Al, Ti)$ .
<b>Al</b>	Strengthening phase $\gamma' Ni_3(Al, Ti)$ former, improve oxidation and hot corrosion resistance but it might affect alloy weldability.
<b>Ti</b>	Strengthening phase $\gamma' Ni_3(Al, Ti)$ and $\eta$ phase former. It might affect alloy weldability.
<b>W</b>	Solid-solution strengthener, MC, $M_{23}C_6$ and $M_6C$ carbides former
<b>Ta</b>	Solid-solution strengthener, MC carbide former, improve creep properties
<b>Re</b>	Solid-solution strengthener, retard $\gamma'$ coarsening and improve the creep life
<b>C</b>	M(C,N) carbonitrides former, grain-boundary strengthener
<b>N</b>	M(C,N) carbonitrides former
<b>B</b>	Grain-boundary strengthener, improve creep properties and rupture strength

Back to phase strengthening, the contributes of  $\gamma'$  and  $\gamma''$  come from:

- The intrinsic strength of these two phases
- Lattice mismatch between these phases and the matrix  $\gamma$
- The anti-phase boundary energy (APB) in the phases, which is proportional to the energy the dislocations need to have in order to pass through  $\gamma'$  and  $\gamma''$ .

In this alloy, the ratio between these phases is usually almost constant, or at least it does not change too much remaining close to roughly 3 ( $\gamma'':\gamma'$ ).

The  $\gamma''$  has a bigger mismatch with the matrix compared to the  $\gamma'$ . The slightly mismatch between matrix and these phases is the reason why they increase so much the alloy strength (Deng et al., 2018; Donachie & Donachie, 2002).

The reason why this alloy together with the Inconel 625 are the most diffused in the additive manufacturing sector is that they are less prone to strain-age cracking than the Ni-based alloys having as main strengthening phase  $\gamma'$ .

The sluggish  $\gamma''$  precipitation kinetics hides the creation of high internal stresses in the material which could lead the sample to break. Indeed, the slow precipitation enables stress relaxation to occur before any hardening reactions.

Nevertheless, the ultra high cooling rates, typical of the additive manufacturing, hinder the nucleation of these major strengthening phases. Consequently, even though the mechanical properties of the as-built SLM-processed components are usually higher than the as-cast ones; most of the times heat treated IN718 have instead lower yield and tensile strength than an aged wrought superalloy (Amato et al., 2012).

### 3.1.1 Gamma Prime, Gamma Double Prime, and Delta Phase

$\gamma''$  is the main Inconel 718 strengthening phase. This one and the delta phase ( $Ni_3Nb$ ) share the composition, though they differ in structure. The former has a body-centered tetragonal structure (ordered  $D0_{22}$ ,  $c/a = 2.04$ ) while the latter a orthorhombic structure (ordered  $D0_a$ ), far more brittle than the former.

On the contrary, the ordered  $\gamma'$  phase (ordered  $L1_2$ ) has the same fcc crystal structure of the austenitic matrix  $\gamma$ . As it comes to precipitation strengthening, important is the difference in lattice constant in comparison with the matrix. Based on this difference the strengthening power of a precipitate over the matrix can change. As regards  $\gamma'$ , being an ordered alternated structure of Ni and Al or Ti, the bond among them has a metallic and partially covalent nature. This aspect makes the bond slightly shorter than the one among Ni atoms typical of the matrix. This small difference is known as *misfit* and causes the increase in free energy at the interface between the matrix and  $\gamma'$ . The dislocations inside the material will therefore slip until the interface to alleviate the system free energy. In this way, the precipitates of  $\gamma'$  work as pinning points for the dislocations.

The "pinning effect" can be seen once the dislocations get to the precipitate. The energy required to cut into them is really high, this decreases their motion and strengthen the alloy. Indeed, in the precipitate ordered structure, the burger vector is twice the length of one in the matrix. This and the high-temperature stability of this phase are the source of its strong strengthening power and make it ideal in components that have to undergo stresses at high temperatures.

However, it must be aware of its drawback when it comes to additive manufacturing. The precipitation rate of this phase is in fact, really high, and it causes the material to increase the brittleness at the expenses of toughness. This often makes the welding process difficult if not, completely impossible.

Additions of either Ti or Al in the alloy chemical composition would increase  $\gamma'$  volume fraction likely affecting Inconel 718 welding properties, too. Consequently, the common Ni-base SLM alloys have low and controlled Al and Ti content to keep under control the  $\gamma'$  precipitation and its deleterious effect on the alloy weldability.

Inconel 718 takes advantage of both  $\gamma'$  and  $\gamma''$  in a ratio usually around  $\sim 3\%$  and  $\sim 20\%$  in volume, respectively.  $\gamma''$  is characterized by a disk morphology while  $\gamma'$  can be present under spherical-like precipitates or cuboidal shape depending on the misfit. The morphology of the  $\gamma'$  phase is mainly driven by interface energy and strain energy. When the misfit is small the coherent strain is small and the dominant contribute to the total free energy of the system is played by the interface energy. The latter is function of the  $\gamma'/\gamma$  interphase surface extension, therefore a spherical morphology is favoured since it has the smallest surface area per unit volume. Contrary, when the misfit is high, the greatest contribute to the free energy is provided by the strain energy. The cubical morphology owns the lowest strain energy value thus forming the typical cubic  $\gamma'$  phase (Shao et al., 2019). The latter structure can usually be observed in alloys with high concentration of  $\gamma'$  such as the single crystal alloy PWA 1484.

The negative aspect owned by  $\gamma''$  is the lower range of stability (low solvus temperature), which is the main limitation for the Inconel 718. Prolonged exposure at about  $650^\circ\text{C}$  or higher temperatures, makes  $\gamma''$  rapidly overage and decompose into the equilibrium  $\delta$  phase which, more often than not, worsens the mechanical properties such as - loss in strength and creep life (Mignanelli et al., 2017).

The  $\gamma''$  name derives from the fact that its structure is close to the  $\gamma'$  one. The '*double prime*' definition highlights the  $\gamma''$  characteristic of having the  $c$  parameters almost twice the lattice constant of  $\gamma'$  phase.

As aforementioned,  $\delta$  is a stable intermetallic phase in which  $\gamma''$  tends to transform in particular condition. It is characterized by a orthorombic structure (ordered  $D0_a$ ) with lattice constant as follows (S. Li et al., 2015).

a	b	c
0.574nm	0.422nm	0.454nm

This phase usually precipitates heterogeneously at grain boundary forming blocky particles. Even though it also grows with plate-like morphology when it precipitates in the grain interior. However, it is not usually present in the as-manufactured form. Indeed, SLM typical low pre-

heat temperatures and its high thermal gradients generate cooling rates so high to hinder the precipitation of any strengthening phase such as  $\gamma''$  and  $\gamma'$ , or the decomposition of  $\gamma''$  into  $\delta$ .

This latter is actually not the only way to generate  $\delta$ . Indeed, the previously mentioned solution treatment, can both slightly dissolve the Laves phase and precipitate the needle shaped  $\delta$  precipitates. It can be generated by a matrix supersaturation of its forming elements.

As a result of Nb segregation, nuclei are generated inside the grain and in its boundary. Even though  $\delta$  is usually undesired, to some extent it can bring some advantages reducing the grain boundary creep fracture. In order to achieve that and having this phase disperse only in the grain boundary, heat treatment has to be performed.

According to Deng et al., if the sample having already dispersed inside the  $\delta$  phase undergoes a heat treatment at temperature in the range of 1080°C (like during the homogenization treatment), the delta phase will be completely dissolved being the temperature higher than its solvus. Laves and  $\delta$  phase will release Nb which will distribute evenly in the matrix. If a solution treatment is carried out after the homogenization process, the  $\delta$  phase will precipitate only in the grain boundaries.

If the precipitates have small dimension, smaller than a micrometer, they do not represent an issue. Conversely, if they are as big as some micrometers, they can easily break and act as favourable site of crack propagation in inconel 718.

A solution heat treatment around 980°C only causes the coarsening of this phase. So, set a proper treatment schedule lets control its precipitation keeping its size under control and hence achieving improvements in creep life (Deng et al., 2018; S. Li et al., 2015).

In conclusion, even though the hardness can change usually no strengthening effects are expected from this phase since it is not coherent with the  $\gamma$  matrix. So, as regards L-PBF processed samples, delta is usually not desired.

### 3.1.2 Laves Phases

The majority of the nickel superalloys are particularly sensitive to the *Laves phases*  $(\text{Ni,Fe,Cr})_2(\text{Nb,Mo,Ti})$ , hexagonally close packed structures (hexagonal  $C_{14}$ ).

Laves is an intermetallic phase characterized by an irregular shape and often embedded in the interdendritic region rich in the elements listed above. They are mostly heavy elements with low thermal diffusion coefficient. So, the interdendritic region becomes particularly prone to the development of this phase, which can reduce the mechanical properties of the Inconel 718 in several ways. Perhaps the most important is its hard nature that causes a brittle fracture of the phase. Furthermore, Laves consumes large amounts of Nb leading to a depletion of this important hardening element in the matrix.

Moreover, even though this does not directly affect the SLM process, while welding the Laves phase can melt causing micro-fessurization in Inconel 718 components (Schirra, Caless, & Hatala, 1991).

Unfortunately, the formation of this phase is almost impossible to avoid. It affects every sample

of Inconel 718 printed by SLM. Heat treatments have been therefore adopted in order to fully remove or reduce its concentration and its following deleterious effects. The usual treatments carried out on this kind of alloy are solution, homogenization and ageing.

According to (Deng et al., 2018), both solution and homogenization processes contribute to more or less intensely dissolve the Laves phase. The temperatures at which these processes are usually carried out are around 980°C for the solution and 1080°C for the homogenization. On the contrary, the temperature involved during the aging heat treatment can vary roughly between 620°C and 720°C. This temperature range is not enough to let the Laves phase be dissolved. Therefore, direct ageing of as-manufactured samples will not have any effect on the Laves phase.

Remove this phase means to bring Nb back into the matrix. Moreover, it allows  $\gamma''$  to reach the maximum precipitation achieving the component peak strength. As aforementioned, a solution treatment can partially dissolve the Laves phase. Anyway, the latter will dissolve almost completely only when heated up to temperature of 1080°C or more.

### 3.1.3 Eta Phase

The  $\eta$  phase is a hexagonal close-packed (TCP, ordered D0<sub>24</sub>) crystal structure which shares the forming elements with the  $\gamma'$  phase. Its chemical composition is Ni<sub>3</sub>Ti, although recent investigations discovered that some other elements have solubility in it. Co, Al and Cr can take part to the crystal structure, according to that the updated stoichiometry is often referred as either (Ni,Co)<sub>3</sub>(Ti,Al,Nb) or Ni<sub>3</sub>Al<sub>0.5</sub>Nb<sub>0.5</sub> (Antonov et al., 2015; Fedorova et al., 2014).

This phase is usually a deleterious phase associated with the loss of ductility of the component. It exhibits a non-coherent lamellar and/or needle like morphology. Eta usually develops at high temperature whereas, when present, it tends to transform in  $\gamma'$  at low temperature.

Both Ti and Co stabilize the phase even though the former has a strongest effect on it. The fast kinetics typical of the powder bed fusion techniques hinder indeed its precipitation as well as of the  $\delta$  phase. Therefore, if allowed by the chemical composition, its precipitates may need an heat treatment to form.

When the composition allows the formation of both delta and eta phases, their identification may be difficult. These two phases are indeed similar in morphology. Like  $\eta$ ,  $\delta$  creates thin plates apparently similar, **Fig. 11**. Actually,  $\eta$  precipitates thinner and more irregular plates, often in the form of grouped precipitates in close proximity.

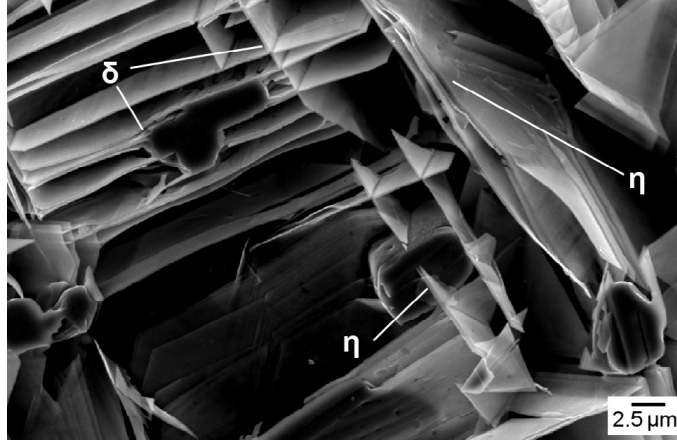


**Figure 11:**  $\eta$  Phase and  $\delta$  Phase Morphology (Antonov et al. (2015))

Antonov et al. defined an equation function of the chemical composition able to predict the likelihood of a  $\delta$  or  $\eta$  precipitation. This is based on the fact that having the same former elements of the main strengthening phases, their precipitation is favoured when the matrix is saturated of these elements and the solubility limits are approached. Following their approach, if the ratio (in %<sub>at</sub>)  $\text{Al}/(\text{Nb}+\text{Ta}+\text{Ti})$  is less than  $\sim 0.85$ , the microstructure will tend to create  $\delta$  and/or  $\eta$  precipitates. On the contrary, if the ratio exceeds that value these phases will not be stable enough to precipitate.

## 4 *In-situ Alloying*

*In-situ* refers to a technique in contrast with the utilization of pre-alloyed powders. Unlike the latter, the former achieves the final composition by mixing different powders.

As far as the conventional processes are concerned, the miscibility of elements, their solubility ranges and the risk of precipitation of deleterious phases may hinder, if not make impossible, certain alloys to be manufactured.

Under this point of view, the powder bed technology provides astounding opportunities. Indeed, it owns advantages of powder metallurgy allowing to mix a wide range of powders. As shown in **Fig.12**, the rapid heating and cooling rates ( $10^6$  K/s), peculiar of the L-PBF processes, can prevent the formation of such deleterious phases (Shoemaker, 2005; Lippold et al., 2011).

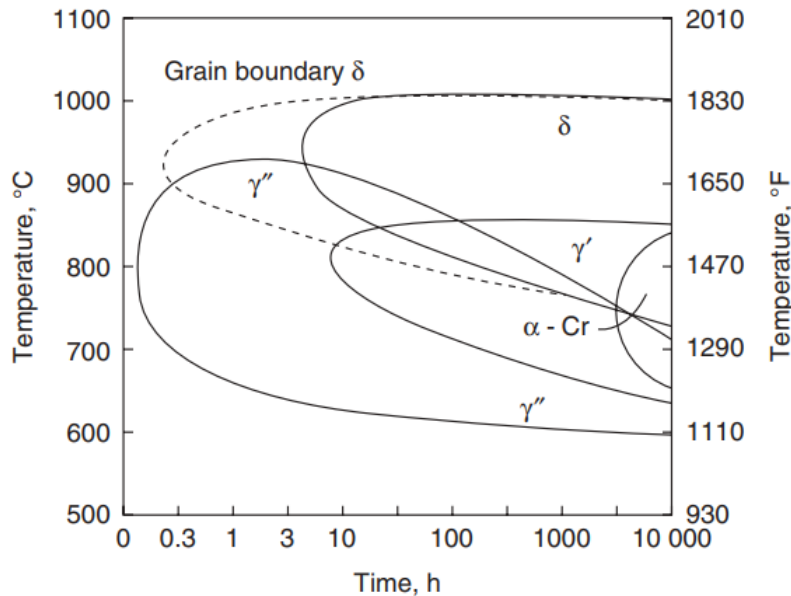


**Figure 12:** Time-Temperature-Transformation Diagram Inconel 718 (Lippold et al. (2011))

The *in-situ* alloying gets access to particular chemical composition in a faster and economical way with respect to the traditional processes. Nonetheless, selecting suitable process parameters capable of guaranteeing efficient alloying is far from easy.

*In-situ* alloying in SLM is challenging since both homogeneity and quality of the 3D-printed part are required. In order to achieve a good alloying of the elements, the molten metal should have low viscosity.

A trade-off must be made between high quality outputs in term of density or mechanical properties and a successful *in-situ* alloying.

However, laser powder bed has been proven to be a viable method to print powders using in-situ alloying (Krakhmalev et al., 2017). Many other works have been carried out using alloys such as Al-Si (Vora et al., 2015), Ti6Al4V, Ti-Nb (Fischer et al., 2016).

The latter, it showed how the in-situ methodology can be the most convenient way to produce some alloys exploitable with additive manufacturing. Ti-Nb alloys, like Ti-26Nb, are essential for the biomedical sector being inert and not toxic. Nevertheless, the production of their powders is challenging. The melting point of the Ti-Nb alloys is so high that the conventional gas atomization route is difficult and, time and energy expensive. Consequently, the in-situ alloying may be a significantly faster and cost/effective alternative to the conventional processes.

As previously said, the *in-situ* alloying is far from perfect. There are many problems to consider such as the risk of elemental segregation, powder flowability, choice of proper elemental powder size distribution and the proper powders mixing technique to be adopted. All those factors may lead to poor repeatability, variation in the response of the powder bed to the laser and the creation in the final component of regions having highly different chemical compositions.

When mixing free-flowing powders a random mixture is created and the chemical composition in any point can only be statistically predicted. Usually, *in-situ* alloying mixed powders are different in size and shape. When particles of different sizes are mixed together, they tend to group together, yielding a segregated mixture. This inhomogeneity causes different behavior of the powder with respect to the laser, such as laser energy absorption.

Furthermore, unlike the pre-alloyed condition, the *in-situ* alloying uses the laser to directly melt and create the desired alloy composition. This instantaneous synthesis of the alloy is associated to a negative enthalpy of mixing which can modify the thermodynamics of the process (Simonelli et al., 2018).

As explained by Yadroitsev et al., making it simple there are three important parameters to consider:

$$E = \rho \cdot [C \cdot (T_m - T_0) + L_f] \left[ \frac{J}{m^3} \right], \quad (8)$$

$$t_{D.I.} = \frac{d_{spot}}{v} [s], \quad (9)$$

$$t_{hom} = \frac{r^2}{a} [s]. \quad (10)$$

E stands for the amount of energy per unit of volume useful for fusion of the material. Whereas  $\rho$  is the density, C the specific heat capacity,  $T_m$  the melting temperature,  $T_0$  the starting temperature and  $L_f$  the latent heat of fusion. E changes depending on the powder material but if the values owned by two different mixed powders are close to each other, the energy provided by the laser will be enough to melt the different materials (Yadroitsev et al., 2017).

Nevertheless, a successful melting of the powder is strictly bonded to the exposure time (dwelling time) and the particle size, as shown by equations (9) and (10). The former represent the spot size

divided by the scanning rate. As discussed in the 2.3.5, the higher the scanning rate, the lower the exposure time of the powder to the laser energy. This reduces the melt pool peak temperature and its viscosity and could lead to track instability and balling. On the other hand, slow scan speed can have the opposite effect causing deep melt pool and keyholing. The last equation represents the square of the particle radius divided by the thermal diffusivity of bulk metal. The homogenisation temperature time ( $t_{hom}$ ) is the time required for the homogenization of the temperature with the powder particles around.

Whenever the energy provided is high enough to melt the powder if  $t_{hom} < t_{D,I}$  there will be a perfect fusion of the powder. While, if  $t_{hom} \gg t_{D,I}$ , partial melting of the powder might occur.

Therefore the energy must be high enough to melt the particles and the exposure time long enough to avoid lack of fusion. Despite that, even though we manage to achieve such result with both powders, the time affects the alloying process. Different powders have different viscosity when molten, in order to avoid segregation and inhomogeneity, the melt pool must exist long enough time to allow the thermal diffusion of the elements (Yadroitsev et al., 2017).

In general, these statements make clear that process parameters considered optimal for a pre-alloyed feedstock will be most of the time not the proper ones when it comes to *in-situ* alloying. Even though it is useful to rely on parameters for pre-alloyed feedstock as starting point, new ones must be defined depending on the mixing technique adopted.

*In-situ* alloying is an outstanding way to speed up the material development but it still needs to find a repeatable mixing process. An in-depth knowledge of the feedstock would allow researchers or users to set the proper parameters each time, thus making the process repeatable.

## 4.1 Inconel 718 Development

Inconel 718 is one of the oldest nickel superalloys. It was firstly discovered through a research investigation aiming to create a new solid solution strengthened Ni-base superalloy, back to 1950s. One of the element under investigation was in fact the niobium, which then became the most important element in the alloy. The addition of this element caused a strong age hardening which later, researchers discovered to be associated with a phase having a large misfit with the  $\gamma$  matrix. Although the presence of  $\gamma'$ , most of the strengthening was due to this newly discovered  $\gamma''$  phase.

The actual innovation brought by this alloy was the possibility to cast and wrought large components. Because of the high precipitation kinetics of the  $\gamma'$ -phase, this had been unusual for Ni-base alloys. This new strengthening phase allowed Inconel 718-based components to remain soft during the machining process. As mentioned in 3.1.1,  $\gamma''$  is indeed characterized by a sluggish precipitation which provides excellent weldability and manufacturability to the material. All these aspects led Herbert Eiselstein L. to file the patent in 1958 (Eiselstein, 1962).

Alloys with high content of  $\gamma'$  phase ( $Ni_3(Al, Ti)$ ) have always been difficult to work and weld. Unlike  $\gamma''$ ,  $\gamma'$  tends to precipitate during forging, making the component harder, stronger and with a reduced ductility. Yet, during welding it causes strain-age cracking (SAC) making the process difficult or even not possible. Moreover, a strengthened material is much more difficult to machine and this hinders the achieving of component with higher complexity. This is why in the past,

$\gamma''$  has always been considered an irreplaceable phase when requirements for both strength and manufacturability are needed.

Nevertheless, the instability of the  $\gamma''$ -phase makes impossible to significantly improve the microstructural thermal stability of the alloy as long as it is used as main strengthening phase. Though recently, deeper studies have highlighted the reasons behind its precipitation rate and stated  $\gamma'$  as possible substitute.

On this basis, several alloys have been studied such as ATI718plus, VDM 780 Premium or K4750. As far as the temperature capability is concerned, these alloys gained +50°C and +100°C, compared to the inconel 718 (Rösler et al., 2019; Xie et al., 2019).

All these derivatives, are based on the  $\gamma'$  as principal strengthening phase. The need for it stems from the fact that contrarily to  $\gamma''$ , the former is a stable phase. Exposed to high temperature, it does not tend to transform in other stable forms. Nevertheless, even though it may seem impossible to get 718-type properties making use of that fast precipitating phase, Rösler et al. demonstrated its feasibility. They did that by clarifying the influence of several factors on  $\gamma'$  and  $\gamma''$  precipitation kinetics. Among others, important factors are:

1. Solvus temperature of the precipitate phase;
2. Diffusivity of the elements taking part to the precipitate;
3. Interface energy.

Elements with low coefficients of thermal diffusion are typical of phases with slower precipitation rates. Despite this, the diffusivity of Nb, Al and Ti at around 800°C (temperature usually involved in the inconel 718 aging process) is almost the same. Consequently,  $\gamma'$  and  $\gamma''$  should have equal or almost the same precipitation kinetics, clearly not true.

Even considering the interface energy, these two phases own values most of the times reported by the literature as close. Neither the diffusivity nor the interface energy hence clarify to what the precipitation kinetic of these phases is due.

The solvus temperature was the key solution that allowed researchers to replace  $\gamma''$  with  $\gamma'$ . Indeed, if the solvus temperature increases, the precipitation onset shifts to higher temperature, too. It is common knowledge that the diffusion is faster at higher temperatures, and so the precipitation kinetics involved. Therefore, since  $\gamma'$  has a higher solvus temperature than  $\gamma''$ , the precipitation kinetics involved in its precipitation range are higher too.

Following these discoveries, recently high content  $\gamma'$  Ni-base superalloys in additive manufacturing are more and more common. Research have been focusing on developing new Ni superalloys capable to reach always higher temperatures such as high  $\gamma'$  content ABD 900AM (Alloy-By-Design modelling approach) . This Ni-base alloy precisely designed for AM purposes has 33%  $\gamma'$ , temperature capability of 900°C and similar mechanical properties to IN939 (Tang et al., 2020; Ghossoub, Tang, Panwisawas, Németh, & Reed, 2020).

Based on this trend, in the following sections are highlighted several alloys, results of different approaches to stabilize inconel 718. They have in common a reduction of  $\gamma'$  solvus temperature

sharing the need for a decreased precipitation kinetic to keep the newly developed alloys as weldable and strong as the original one.

#### 4.1.1 Allvac 718Plus

The development of a new alloy is a tough task. Not only have the properties to be better but the alloy has to outperform the previous alloys in such a way to make the former economically feasible. As a matter of facts, when it comes to Inconel 718 derivatives and temperature capability, 55°C of temperature advantage is often considered as the least improvement you can get in order to provide the market a new product (Kennedy, 2005). Improving the maximum temperature which an alloy is able to reach, even when small improvements are considered, represents a cost. Most of the time, it requires changes in alloy composition and therefore its cost arises. Because of this, a new alloy will be successful in the market only when it represents an essential and not replaceable solution to a given problem.

The aeronautic sector has always needed to improve Inconel 718. Indeed, in order to improve the engine efficiency a temperature arise is needed and so the thermal stability of this alloy. This has been of paramount importance because IN718 is the most common Ni-base superalloy in the aeronautic sector and an important material in the engine design. Allvac 718Plus is a precipitation hardened Ni-Cr-Co-Fe base superalloy developed by ATI Allvac and patented in 2013 (W.-D. Cao et al., 2013).

This alloy has been developed in order to achieve the high-temperature capability and thermal stability of Waspalloy alloy and the good weldability and workability typical of Inconel 718. Indeed, ATI asserts ATI 718Plus provides a nominal 100°F (55°C) temperature advantage compared to IN718, as well as superior strength, formability, wear and weld cracking resistance with respect to Waspalloy (ATI, 2013).

**Table 4** shows the comparison between the chemical composition of Inconel 718 and Allvac 718Plus (718Plus) in %<sub>wt</sub>.

**Table 4:** Allvac 718Plus Chemical Composition (Tsang et al. (2010))

Name	Ni	Cr	Mo	W	Co	Fe	Nb	Al	Ti	C	P	B
Allvac 718Plus	Bal.	18	3.0	1.0	9.0	10	5.4	1.4	0.70	0.020	0.014	0.006
Inconel 718	Bal.	18	3.0	-	-	18	5.4	0.5	1.0	0.025	0.007	0.004

Unlike the following alloys, 718Plus is strengthened by both  $\gamma'$  and  $\gamma''$ . Despite of this, the main strengthening phase is  $\gamma'$  instead of  $\gamma''$  as in IN718. Moreover, referring to **Figure 9**, the chemical composition places it in the readily weldable alloys.

This is confirmed by the CHRT (Controlled Heating Rate Test) . This test was developed by Rocketdyne in 1960s and is used to relate hot tensile ductility to straining age cracking. Because of that, it proves to be an easy way to compare the weldability of several alloys.

According to the test, the higher the ductility between 816°C and 899°C, the greater the resis-

tance to strain age cracking. As shown in the **Fig. 13**, having weldability and straining age cracking resistance ATI 718Plus can be compared to well weldable alloys such as inconel 718 and C263, much higher than Waspalloy and René 41.

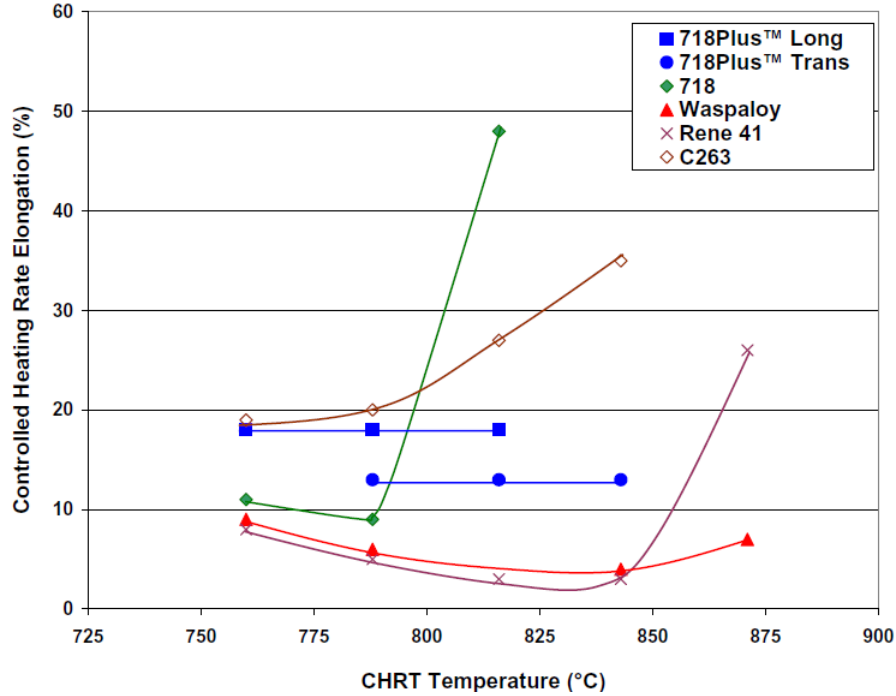


**Figure 13:** Sensibility to Strain Age Cracking via CHRT (Kennedy (2005))

The chemical composition causes an ageing response similar to the Inconel 718 one. As in **Table 4**, the main differences between the chemical composition of this alloy and the 718 are an higher amount of Al (1.4 %<sub>wt</sub>) and a lower amount of both Ti (0.70 %<sub>wt</sub>) and Fe (10 %<sub>wt</sub>). Furthermore, there is the presence of two elements completely absent in the 718 composition - W (1.0 %<sub>wt</sub>) and Co (9.0 %<sub>wt</sub>). Smaller variations can be found in the amount of P and B as well. These addition have been made in order to increase the grain boundary strength and consequently improve the alloy response to creep and stress rupture (Kienl, 2019).

The development of new derivatives of the alloy 718 often starts from the analysis of the influence which Al and Ti have on the thermal stability. This because they are the most important elements to define the  $\gamma'$  stability. In this respect, 718Plus has Al+Ti content (4 %<sub>at</sub>) almost twice the 718 one which is around 2%<sub>at</sub>. According to several sources, the higher the content of Al+Ti, the higher the amount of  $\gamma'$  at the expenses of  $\gamma''$  and  $\delta$ . To get  $\gamma'$  as main strengthening phase, Al+Ti was found to be greater than 3%<sub>at</sub> (Kennedy, 2005; Tsang et al., 2010; Löhnert & Pyczak, 2010; Kienl, 2019).

The second step is to understand which role the Al/Ti ratio plays in the mechanical properties of the final component, **Fig. 14**.

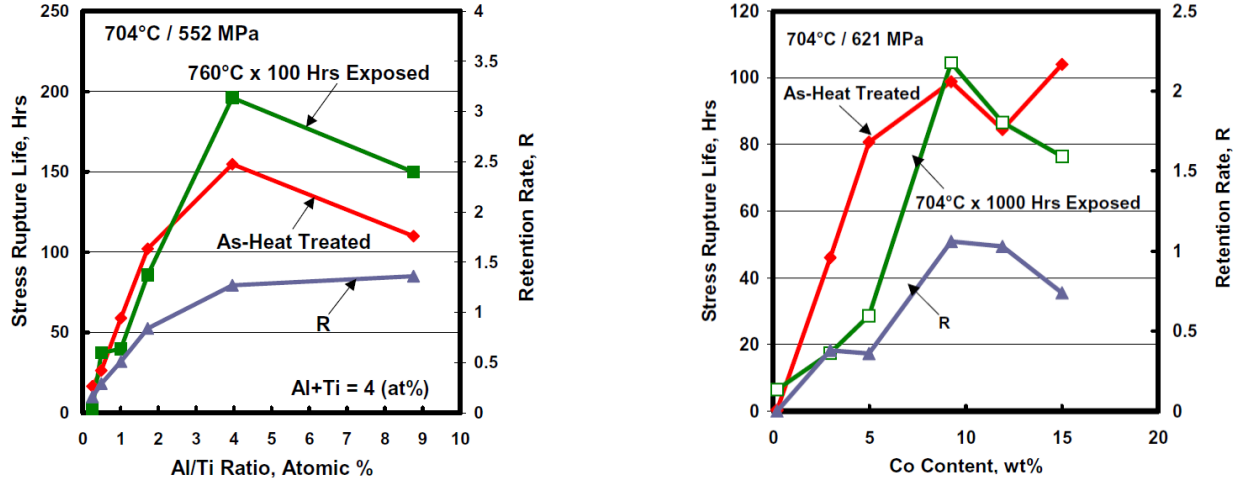


**Figure 14:** Stress Rupture Life and Thermal Stability Function of ATI 718Plus Chemical Composition (Kennedy (2005))

Unlike Al+Ti which controls the  $\gamma'$  and  $\gamma''$  precipitation, working on Al/Ti ratio acts on the  $\gamma'$  growth rate and its misfits with the matrix. Reducing that ratio leads towards slower  $\gamma'$  growth and lower misfit (Kienl, 2019).

The previous graphs show the influence those chemical variations can have on mechanical properties. It can be seen as the stress rupture life peaks at Al+Ti=4%<sub>at</sub> and Al/Ti=4. The parameter R represents the thermal stability, they got it dividing the stress rupture life of a sample with extended exposure at high temperature and the value of a as-heat treated one. It easy to understand then that increasing the Al/Ti ratio the material thermal stability will undergo a notable improvement.

Same considerations can be made speaking of Co. Its presence have a positive influence on the thermal stability of 718Plus, even though it follows an opposite trend when its content exceeds 10%<sub>wt</sub>. The higher the content of Co the lower the solubility of Al and Ti in the matrix hence the higher the  $\gamma'$  volume fraction.

As far as the Nb is concerned, keeping its concentration as high as in IN718 had a reason. Nb, like Ta and Ti, is soluble in the  $\gamma'$  phase. All of them are considered among its forming elements since they can replace the Al position in the Ni<sub>3</sub>Al lattice. On the other hand, Nb promotes the reduction of misfit between  $\gamma'$  precipitate-matrix increasing its overall precipitation (Antonov et al., 2015; Kienl, 2019). The slow diffusion of Nb is one of the reason why the  $\gamma''$  phase is characterized by sluggish precipitation and phase growth. When  $\gamma'$  volume fraction increases without any variation in the Nb content, the phase becomes richer in this element. This phenomenon increases the processability of the alloy reducing the precipitation kinetic of  $\gamma'$ .

The addition of W has pro and cons. If on the one hand it decreases the overall bulk diffusivity, on the other hand it increases the density of the material. Tungsten is in fact a solid solution hardening material, which because of its big size, is characterized by slow diffusion coefficient (Kienl, 2019). This aspect is often used in order to increase the resistance at high temperature of

the materials in which it is dissolved. The main issue is that, when it comes to aerospace/aeronautic purposes, being light is of primary importance. If not thoroughly calculated, its addition can increase the overall density so much that the final component would be useless for this kind of applications.

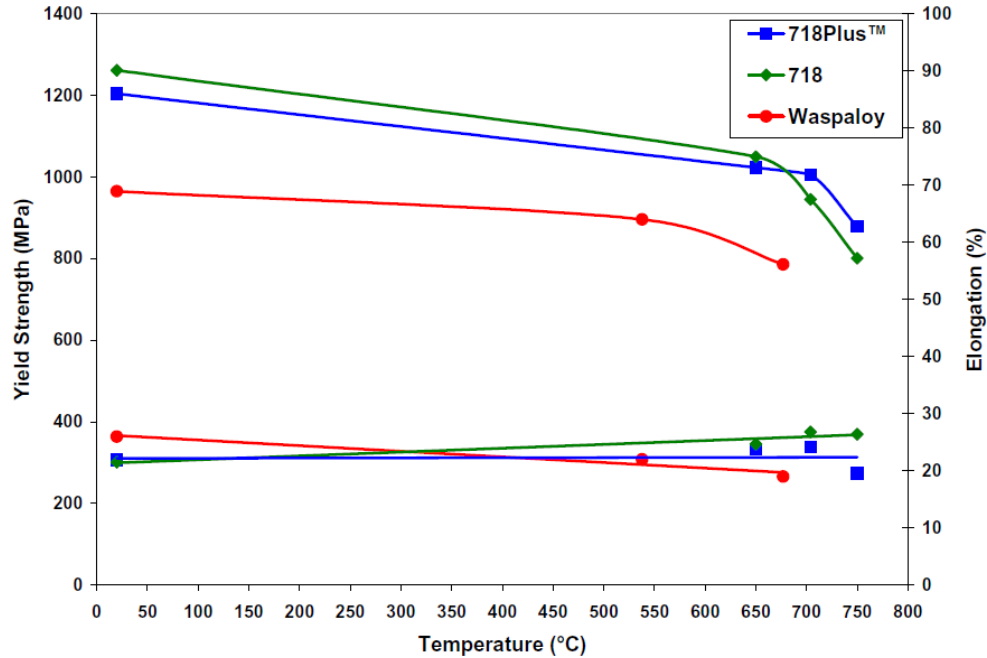


**Figure 15:** Tensile YS and Elongation for ATI 718Plus, IN718 and Waspaloy Function of Temperature (Kennedy (2005))

The **Fig. 15** shows a comparison of mechanical properties owned by 718Plus, 718 and Waspaloy. It is clear that ATI 718Plus exhibits the highest yield strength at high temperature, well beyond the Waspaloy value over the entire temperature range. Above the 650°C the Inconel 718 curve start to be steeper. The 718Plus behaves in a similar way but at roughly +50°C, as aimed by their developers.

As for the ductility, it is quite high for all these alloys, roughly 20% at all tested temperatures.

Given good weldability and mechanical properties have allowed ATI 718Plus to be exploited for L-PBF purposes. Indeed, Megahed et al. used this alloy in order to develop a rapid qualification methodology for the certification of a rocket nozzle developed by Aerojet Rocketdyne (Megahed et al., 2019). This work, sponsored by the Air Force Research Lab (AFRL) under a US government program, aimed to certify laser powder bed fusion as a manufacturing method of components for aerospace applications.

### 4.1.2 VDM 780 Premium

VDM Metals GmbH, in collaboration with the Technische Universität Braunschweig, has developed this  $\gamma'$  strengthened alloy with the goal to push further the limits of the Inconel 718 enabling higher temperature application without losing workability. The key element of this alloy has been the Co, 25 %<sub>wt</sub> Co replaces indeed the Fe inside INCO718.

Addition of Co decreases the  $T_{\gamma', solvus}$  as well as it decreases the solubility in the matrix of  $\gamma'$  forming elements at usual service temperatures. So, the amount of precipitated strengthening phase increases for a given amount of  $\gamma'$ -forming elements.

Joachim Rösler et al. found  $\gamma'$  solvus temperature in VDM 780 Premium slightly above 950°C, namely a bit higher than  $\gamma''$  ones defined as around 930°C. This means that is actually possible to influence the solvus temperature by chemical composition alteration. Yet, it explains why even having as principal strengthening phase  $\gamma'$ , the alloy keeps its good weldability. Through changes in the chemical composition is therefore possible to directly act over the precipitation kinetics of a phase, mitigating troubles such as SAG.

Although the cobalt has a huge role in the development of this alloy, an important contribute was provided by the thorough study on the consequences of Al and Ti content. They turned out to be the key elements when it comes to microstructure stability.

Below, the comparison between the chemical composition of Inconel 718 and VDM 780 premium is displayed (Bergner et al., 2018; Deng, 2018).

**Table 5:** VDM Alloy 780 Premium Chemical Composition (Bergner et al. (2018); Deng (2018))

Name	Ni	Cr	Co	Fe	Mo	Al	Ti	Nb
VDM Alloy 780 Premium	Bal.	18.0	25	-	3.0	2	0.2	5.40
Inconel 718	Bal.	18.1	-	18.0	2.90	0.45	1.00	5.40

The most important differences compared to Inconel 718 are the replacement of Fe by 25 %<sub>wt</sub> Co, a higher Al content (2 %<sub>wt</sub>) and a lower Ti content (0.2 %<sub>wt</sub>). Moreover, the (Al+Ti+Nb) amount is higher than in the alloy 718. This partially explain how this alloy can have similar mechanical properties and high temperature performance even without the  $\gamma''$  strengthening contribute. Indeed, the high content of those elements causes a  $\gamma'$  volume fraction to increase up to roughly 35%, much higher than in the IN718. Unlike the former,  $\gamma'$  shows a smaller misfit and needs higher volume fraction in order to provide the same mechanical strength (Rösler et al., 2019).

All these aspects allow for applications up to 750°C, +100°C compared to the reference alloy. Not only is it superior as far as the thermal stability is concerned, but VDM Alloy 780 Premium outperforms Inconel 718 as regards creep, hardness and strength when produced making use of casting (Bergner et al., 2018; Rösler et al., 2019).

So far, there are no significant studies concerning this alloy and its mechanical properties when 3D printed, for that reason the following considerations mainly focus on casting as production route.

As previously mentioned, the cobalt has the function to slow down the solvus temperature of  $\gamma'$ , despite the relatively high content of Al. This, like the Ti, follows a different trend. As highlighted in **Fig.16**, if it were not for the Co contribute, Al would likely increase the solvus temperature of  $\gamma'$ , accelerating its precipitation kinetic and worsening so its workability (Fu et al., 2009).

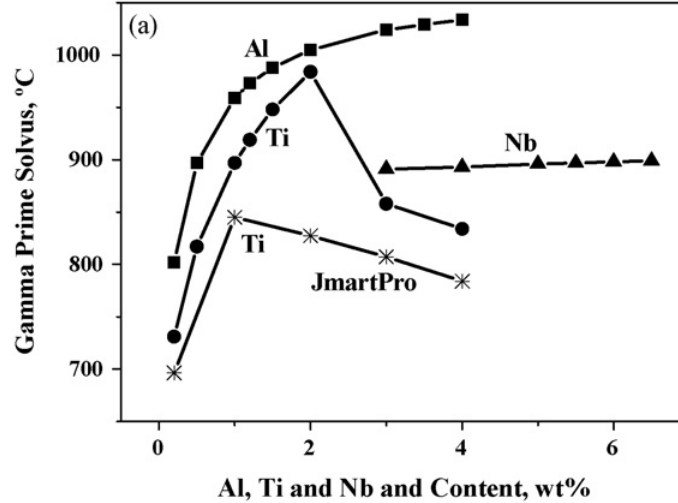


**Figure 16:** Influence of Chemical Composition on  $\gamma'$  Solvus Temperature (Fu et al. (2009))

Despite this, it is inevitable to increase the Al content as precipitation strengthening is switched from  $\gamma''$  to  $\gamma'$ . According to their chemical composition, respectively  $\text{Ni}_3\text{Nb}$  and  $\text{Ni}_3(\text{Al},\text{Ti})$ , in order to achieve  $\gamma'$  as main strengthening phase it requires higher content of Al.

Since  $\gamma''$  is no longer present, it may seem awkward to keep almost constant the Nb content, fairly high in any case. The reason behind that must be sought keeping in mind the scope this alloy has been created for.

Additive manufacturing is a pretty new technology. So far, many processes still involve casting and other traditional manufacturing routes. In those sectors, when Ni-base superalloys are considered, inconel 718 has often occupied the role of the most used Ni alloy. Therefore, its derivatives are often created starting from those manufacturing routes and only then applied to the additive manufacturing. VDM Alloy 780 Premium was born as a casting alloy. Cast ingots are then forged to obtain the desired microstructure and phase dispersion. The reason behind a so high amount of Nb stems from that. Being a  $\delta$  former-element, it useful to allow the precipitation of the correct amount of this phase. Observing proper size and distribution,  $\delta$  is in fact used for grain refinement.

In the **Fig.17** below, is instead highlighted a typical consequence of Co addition. Not only reduces  $T_{\gamma',\text{solvus}}$  but it also stabilizes two other phases, namely  $\delta$  and  $\eta$ .

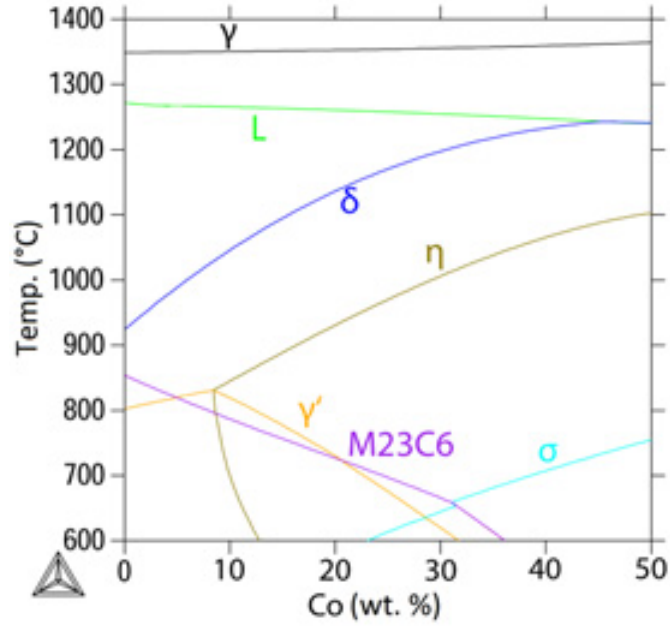


**Figure 17:** Quasi Binary Ni-Co Diagram Based on Inconel 718 with Co Replacing Fe and Partially Ni (Fedorova et al. (2014))

As visible in the figure,  $\eta$  hides an unfavourable circumstance. In fact sharing the chemical composition of  $\gamma'$ ,  $\eta$  has a not negligible influence on its precipitation.

As stated in 3.1.3, the the same way Ti and Al have partial solubility in  $\gamma''$ ,  $\eta$  is often referred as  $(\text{Ni,Co})_3(\text{Ti,Al,Nb})$  since Co, Al and Nb can take part to the phase, as well. Despite this, they differ for the crystal structure, respectively hexagonal close packed (TCP,  $\text{D0}_{24}$ ) and FCC (Antonov et al., 2015). The precipitation of  $\eta$  decreases the concentration of available Ti for  $\gamma'$  development. This phenomenon reduces the microstructural stability of the latter.

The development process of the alloy began thus to focus on reducing  $\eta$  nucleation tendency in favor of  $\gamma'$ .

Along with an increment of Al and Co in the alloy, the researchers started therefore to reduce the amount of Ti directly acting on  $(\text{Ti}+\text{Al})$  and Ti/Al ratio. In this way, its amount was the least possible, enough to avoid the brittle  $\eta$  phase (stabilized by Co and Ti) but not enough to affect  $\gamma'$ .

In order to understand the influence of the Ti/Al ratio and of their weight percentage, isothermal sections of quasi-ternary Ni-Al-Ti system were analyzed, **Fig.18**.

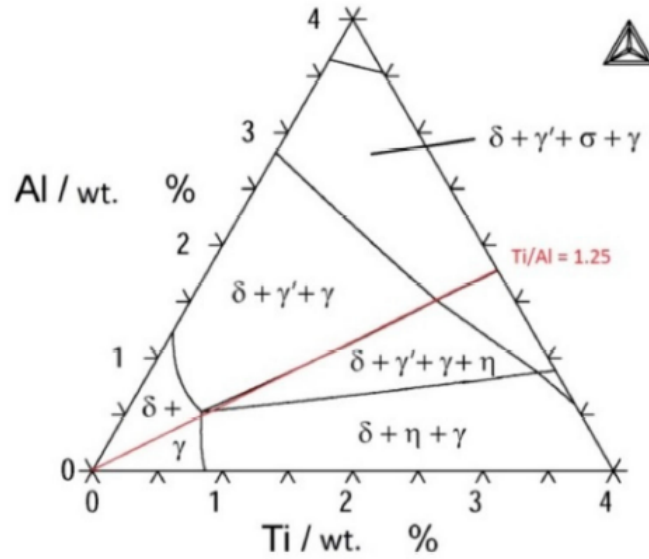


**Figure 18:** ThermoCalc Simulation of Isothermal Sections of the Quasi-ternary Ni–Al–Ti System at 800°C. The Composition of the other alloying elements is kept constant at 17%<sub>wt</sub> Co, 5.4%<sub>wt</sub> Nb, 18.7%<sub>wt</sub> Cr and, 2.96%<sub>wt</sub> Mo. A constant Ti/Al ratio line is highlighted in red (Rösler et al. (2019)).

As displayed in the ternary diagram, alloying elements such as Nb, Cr and Mo are kept constant (to Inconel 718 typical values) contrary to Ti and Al. In this way, it is visible the strong influence of these two elements on the phase stability.

The limitation among the  $(\delta+\gamma'+\gamma+\eta)$  field of existence and the  $(\delta+\gamma'+\gamma)$  one is a line with constant ratio (Ti/Al) equal to 1.25. This to say that the smaller the ratio, the more stable the latter field of existence becomes. In order to provide high microstructural stability at high temperature, VDM Alloy 780 Premium developers slowed down the Ti %<sub>wt</sub> up to 0.2 %<sub>wt</sub>. This not only allowed the alloy to either achieve the typical Inconel 718 mechanical performance or even to outperform them, but to do it at higher temperatures.

Eventually, it is worth to notice that in the **Fig.17** the Laves phase is not present although, it is typical of Inconel 718. The reason stems in the Fe content, which is usually responsible for the deleterious Laves precipitation. Being devoid of this element, VDM Alloy 780 Premium is not affected by its precipitation.

During the VDM Alloy 780 Premium, Co has proved to be an essential element to achieve the desired results. Nevertheless, so high amount of Co in the alloy may increase its price, leaving out one of the IN718 attractive aspects in the Ni-base superalloys sector, its relatively low price.

### 4.1.3 K4750

As the previous alloy, K4750 was born as cast alloy. It has been developed in China by the Institute for Metal Research, for aeroengine application at temperature until 750°C, +100°C compared to the reference alloy INCO 718 and +50°C above ATI 718Plus. A comparison between the chemical compositions of K4750 and INCO718 is shown below (Ou et al., 2019; Deng, 2018).

**Table 6:** K4750 Chemical Composition (\*Inconel 718 does not contain W)(Ou et al. (2019); Deng (2018))

Name	Ni	Cr	Fe	(Mo+W)	(Al+Ti)	Nb	C	B
K4750	Bal.	19.44	5.06	4.35	4.39	1.58	0.12	0.006
Inconel 718*	Bal.	18.1	18.0	2.90	1.45	5.40	0.08	0.006

Unlike in the VDM 780 Premium (4.1.2), K4750 does not make use of Co. On the contrary, it has Fe that was not present in the former. Fe, as already said, could mean presence of Laves phases but in the meantime it helps to lower the price of the alloy.

The main differences between K4750 and Inconel 718 are the addition of W (not present in the latter) and the lower amount of both Nb and Fe. Eventually, K4750 has higher weight percentages of Al and Ti whose sum reaches more than double the Inconel 718 value.

As shown in the following simulation of K4750 thermodynamic phase diagram, **Fig.19**, this alloy is  $\gamma'$  strengthened (Xie et al., 2019). As the previous alloys, this one utilizes this phase as main strengthening mechanism to provide high mechanical properties and microstructural stability at high temperature.

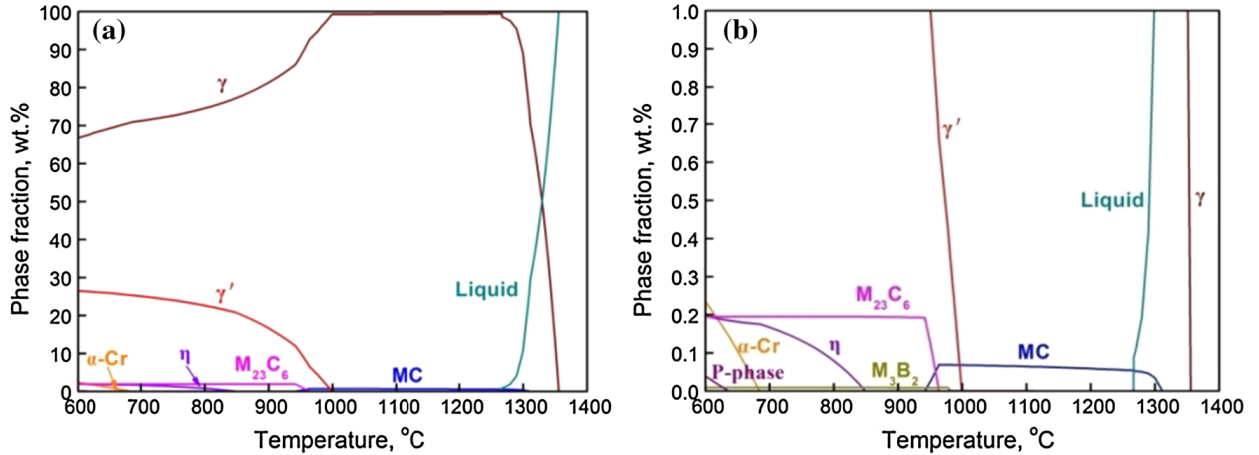


**Figure 19:** K4750 Thermodynamic Phase Diagram in (a) total and (b) partial version (Xie et al. (2019)).

The alloy shows a  $\gamma'$  volume fraction of about 30%. According to the thermodynamic predic-

tions, K4750 is characterized by the presence of some other precipitates or phases such as carbides MC and  $M_{23}C_6$  or the  $\eta$  phase.

Xie et al. and Ou et al. defined the Ti content as 3.0 %<sub>wt</sub>, much higher than both IN718 and VDM Alloy 780 Premium. As previously said, the Ti strongly increases the likelihood of  $\eta$  precipitation, which is demonstrated by this software prediction. However, even though these thermodynamic predictions forecast the presence of several phases, some of them could not be present in a 3D printed material. As it happens for the Inconel 718, with the exception of the Laves phase, many others are not able to form due to the rapid cooling rate. Even though simulation softwares may forecast some phases to precipitate, they could not form because of the followed non-equilibrium process. Despite of that, following thermal treatments can make those phases precipitate, in accordance with the previous predictions.

The following graphs show that the influence of Ti on this alloy is high. Unlike  $\gamma'$ , which sees its solvus temperature increase the higher the Ti content in the alloy, carbides and borides precipitation temperatures are substantially insensitive to Ti concentration, **Fig.20**.

As stated by Ou et al., the amount of Ti inside the alloy causes  $\eta$  precipitation only over a critical content. In the left-hand side of **Fig.20**, this threshold appears to be between 2.71-2.86 %<sub>wt</sub> (Ou et al., 2018).

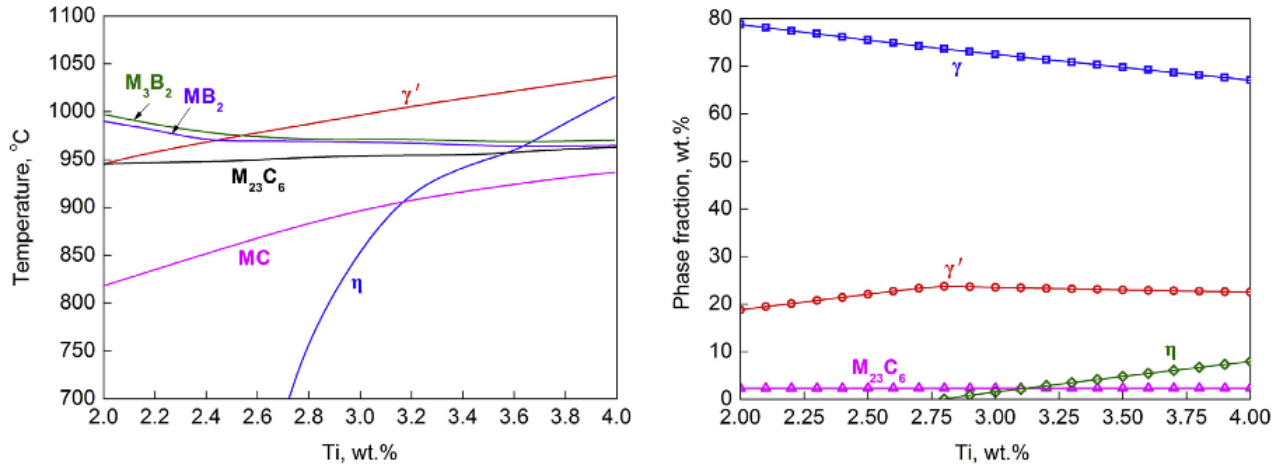


**Figure 20:** Precipitation Temperature of Equilibrium Phases (left) and their Weight Fractions (right) Depending on Ti Content (Ou et al. (2018)).

This has an impact on  $\gamma'$  precipitation. In the graph on the right side of the previous figure, Ti increases the content of  $\gamma'$  in the alloy as long as the  $\eta$  phase does not form. To some extent, these two phases compete in fact for the same forming elements. As aforementioned, Ti stabilizes the  $\eta$  phase which causes depletion of Ti useful for the  $\gamma'$  precipitation. This is clearly shown in the graph, where indeed while  $\eta$  volume fraction steadily increases, the  $\gamma'$  remains constant and apparently no longer sensitive to Ti content.

The research carried out by Ou et al. analyzed the influence Ti has on mechanical properties. They did that by testing two sample cast into bars after being prepared by VIM . Their composition is the same but the Ti amount, 2.4%<sub>wt</sub> and 3.0%<sub>wt</sub> respectively. After having undergone heat treatments such as aging, the sample with more Ti showed a higher room temperature microhardness (RTMH) as well as room temperature yield strength (YS) and ultimate tensile strength (UTS). In particular, the sample richest in Ti showed an increase of 12% in RTMH, 13.8% in YS and 9.6% in UTS with respect to the counterpart. Almost all this aspect are referred as associated with the higher content in strengthening phases such as  $\gamma'$  and MC, caused by the different chemical composition.

As far as the  $\eta$  phase is concerned, according to the same bibliographic reference, its forecast precipitation does not seem to take place. Even though this phase should be stable at high temperature as shown in **Fig.19** and **Fig.20**, its precipitation requires equilibrium and hence long-term aging treatment in order to get as close as possible to the ideal thermodynamic equilibrium. However, here the Ti content made the difference, too. Only the sample having 3.0%<sub>wt</sub> of Ti showed  $\eta$  precipitation after prolonged aging at high temperature (Ou et al., 2018).

Even though this alloy was born to be an alternative to inconel 718 with higher thermal stability, to some extent it may fail. Considering the **Fig. 9**, despite having a higher temperature capability than IN718 there are still some concerns about its weldability.

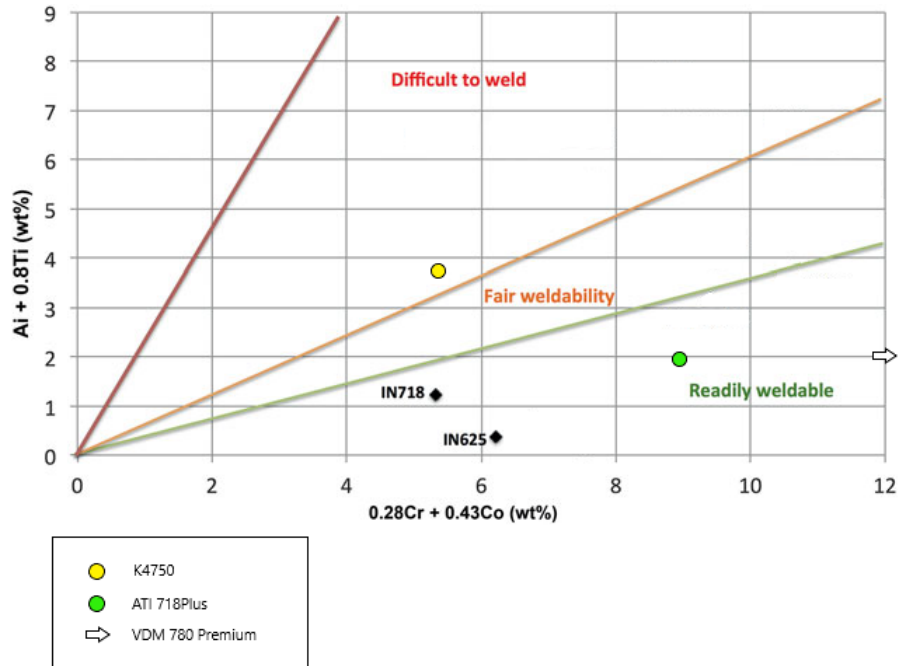


**Figure 21:** Weldability Assessment Diagram for ATI 718Plus, VDM 780 Premium and, K4750 (Attallah et al. (2016)).

In the **Fig. 21** is clear that whereas ATI 718Plus and VDM 780 Premium follow the "Readily weldable" trend of inconel 718 and 625, K4750 lays in the area of "Difficult to weld" alloys. This

could mean SAC or crack formation during welding and of course this is not desired when it comes to additive manufacturing.

Despite of this, many studies have been focusing on the extension of the SLM-processable alloys. Among them there are some "difficult to weld" Ni-base alloys such as IN738LC (Rickenbacher, Etter, Hövel, & Wegener, 2013; Perevoshchikova et al., 2017) and CM247LC (X. Wang, Carter, Pang, Attallah, & Loretto, 2017). Both of them share  $\gamma'$  as main strengthening phase as K4750 but unlike the latter, they are further away from the border with the fairly weldable area, **Fig. 9**.

The success of those studies regarding the SLM-processing of alloys defined as "tough to weld" gives hope about the possibility to use K4750 in the same process. Although, this alloy cannot be considered like Inconel 718 concerning this aspect.

#### 4.1.4 Inconel 718 + Ti

The chemical composition of Inconel 718 can be modified differently depending on the purpose of the project. Unlike the previously described alloy modification which aimed to improve the temperature capability of Inconel 718 increasing its thermal stability, this work was based on different goals. The first was to improve the alloy mechanical properties in conditions different from high-temperature applications. Indeed, while the literature is rich in research aiming to modify Inconel 718 to improve its maximum application temperature, little research has been done on the optimization of its room temperature application employing of additive manufacturing. In particular, there is a lack of knowledge as far as the situ-alloying of Inconel 718 is concerned. Further work is needed concerning the final homogeneity achieved in the printed component and the needed heat treatments to achieve outcomes as close as possible to the ideal pre-alloyed condition. But, first thing first it is important to evaluate the weldability of this blend of powders made out of Inconel 718 and Ti.

The effects that Ti could have on Inconel 718 are different. As already said, it stabilizes the  $\gamma'$  strengthening phase. Therefore, an addition of Ti is expected to increase its precipitation leading to higher values of microhardness compared to the reference Inconel 718. At the same time, higher values of yield strength should be a direct consequence of a greater amount of strengthening phase although, it would bring to lower ductility.

Despite that, several could be possible drawbacks. Indeed the fast kinetics typical of the L-PBF process will probably lead to macroscopical defects such as Ti segregation or not fully melted Ti-particles. Not to talk about the possibility of crack generation. The stabilization of the  $\gamma'$ -phase is usually linked to worse alloy weldability, SAC, and higher porosity in the process outcome. Moreover, segregation means inhomogeneity and therefore regions owning high Ti-concentrations and therefore the risk of generation of intermetallics. Indeed, a high concentration of Ti can bring to the generation of  $\eta$  phase which could alter the mechanical properties of the material.

## 5 Material and Methodology

The project involved a blend of two powders as feedstock of the L-PBF process. Inconel 718 powder (EOS GmbH) had a powder size distribution within the range of 10-50  $\mu\text{m}$ . As for Ti powder, it was commercially pure Ti GR1 (LPW Technology Ltd) with a powder size distribution sieved below 20  $\mu\text{m}$ . Ti and Inconel 718 powders were mixed in a 1:99 ratio (1%<sub>wt</sub> Ti and 99%<sub>wt</sub> Inconel 718 powder) and underwent a mixing process by a rotary cylinder for 24 hours at 60 rpm.

The feed of the process did not involve only new-powder but part of it came from the recycling from a previous job. This causes the presence of several morphologies ascribable to different phenomena. In particular, it is clearly visible the presence of satellites, fine particles stuck to larger ones. Moreover, the applied load due to the mixing process caused the Ti-particles to deform and to mechanically stick to the Inconel 718 ones, **Fig.22a,b**. As visible in the image, the latter condition characterizes most of the time the Ti-particles and less frequently they keep their spherical shape as in **Fig.22c,d**.

The creation of those physically or mechanically joined particles is actually not bad and it can probably promote a better homogeneity of the following 3D-printed component. Though, the presence of a great amount of satellites could affect the powder flowability leading to a higher amount of porosity in the final specimens.

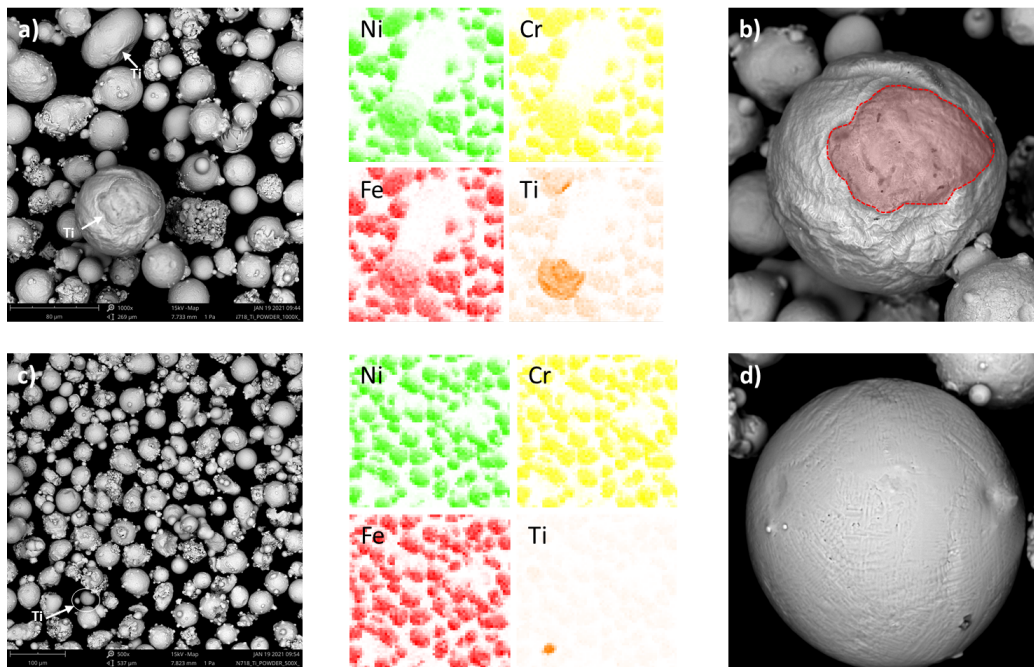


**Figure 22:** Morphology of Inconel 718 Situ-Alloyed Powder. Deformed Ti particle over a bigger Inconel 718 one in a) and b), spherical particle of pure Ti in c) and d).

The research process followed a methodology highlighted in **Fig.23**. The beginning consisted of finding the proper printing parameters for the new situ-alloyed powder. Common printing

parameters for Inconel 718 were used as starting parameters in order to improve them and to tailor the process to the new alloy.

Each sample underwent the usual steps of stress relief and EDM-removal from the printing platform to avoid alteration in the physical-mechanical state of the samples due to their internal stresses after the printing process.

The quality of the set parameters was defined through metallographic analysis of both hardness and porosity. Once achieved satisfactory results as regards those sample properties, the optimized parameters were used to print the samples which went ahead in the characterization process.

The latter involved their metallographic characterization in three conditions, as-built (ab), solution treated (ST), and solution treated and double-aged (SDAG) respectively. The characterization process involved image analysis, scanning (SEM) and optical microscopy (OM), EDX analysis, and mechanical test like the hardness (Vickers and Brinell) test.

Throughout the process, both pure and situ-alloyed Inconel 718 were printed. The former was employed for comparison to the situ-alloyed condition to get a clear idea of the influence Ti has on all the aspects of each analysis.

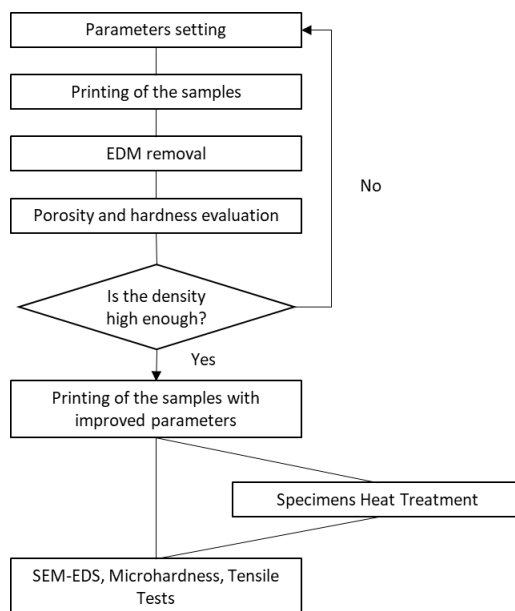


**Figure 23:** Flow Chart of the Process Steps.

## 5.1 L-PBF

The samples were printed employing an L-PBF machine, precisely the Mlab Cusing R (Concept Laser GmbH) visible in **Fig.24**



**Figure 24:** Mlab Cusing R L-PBF Printing Machine (*Concept Laser GmbH* (2021)).

<b>Layer thickness</b>	15 – 30 $\mu\text{m}$
<b>Production speed</b>	1 – 5 $\text{cm}^3/\text{h}$ (depending on material)
<b>Laser system</b>	Fibre laser 100 W (cw)
<b>Max. scanning speed</b>	7 m/s
<b>Focus diameter</b>	approx. 50 $\mu\text{m}$
<b>Connected loads</b>	Power consumption max. 1.5 kW Power supply 1/N/PE AC 230 V, 16 A
<b>Inert gas supply</b>	1 gas connection provided / Nitrogen or Argon
<b>Inert gas consumption</b>	approx. 0.6 – 0.8 l/min *
<b>Machine dim:</b>	705 x 1848 x 1220 mm (W x H x D)
<b>Handling station dims:</b>	729 x 1391 x 628 mm (W x H x D)
<b>Machine weight</b>	approx. 600 kg
<b>Handling station weight</b>	approx. 100 kg
<b>Operating conditions</b>	15 – 30°C

**Figure 25:** Mlab Cusing R Technical Sheet (*Concept Laser GmbH* (2021)).

The Mlab R machine, whose technical sheet is visible in **Fig.25**, uses a laser to melt the metal

powder creating a complex structure from a CAD file using the patented LaserCUSING technology. This machine can be used to print both non-reactive and reactive materials such as titanium. The process chamber is separated by the handle station in order to allow safe and easy sample handling.

All the steps are led under inert gas which shields the process from the external environment. Precisely, in this work, the process was carried out under argon-gas continuous flow.

Every sample was printed in a cubic shape with a 1cm edge, then removed from the printing platform by electro-discharge machining, and then characterized. The printing parameters will be discussed in the next chapter since they underwent an optimization process.

## 5.2 Heat Treatments

To understand the influence of the Ti on the microstructure and mechanical properties of the modified Inconel 718, the printed samples were divided into three groups. Each of them underwent a different heat treatment. Some of them were analysed in the as-built (ab) condition whereas the others were either solution treated (ST) or both solution treated and double-aged (SDAG).

The samples underwent a heat treatment according to the AMS5667 in **Fig.26**, standard treatment widely used for wrought and cast Inconel 718. It involves a solution treatment at  $1065^{\circ}\text{C} \times 1\text{h}/\text{water cooling (WC)} + 720^{\circ}\text{C} \times 8\text{h}/\text{furnace cooling (FC)} + 620^{\circ}\text{C} \times 8\text{h}/\text{air cooling (AC)}$  (X. Li et al., 2019; *SAE International AMS*, 2020). Despite the actual AMS 5667 involves air cooling after ST, we employed water cooling to avoid the formation of any phase so that the concentration of elements in the matrix before the aging treatment was as high as possible.

The purpose of the heat treatment is indeed to release age-hardening constituents (i.e. Nb, Ti, Al) in the matrix making them available to the following steps of precipitation of the strengthening phases (Tucho & Hansen, 2019).

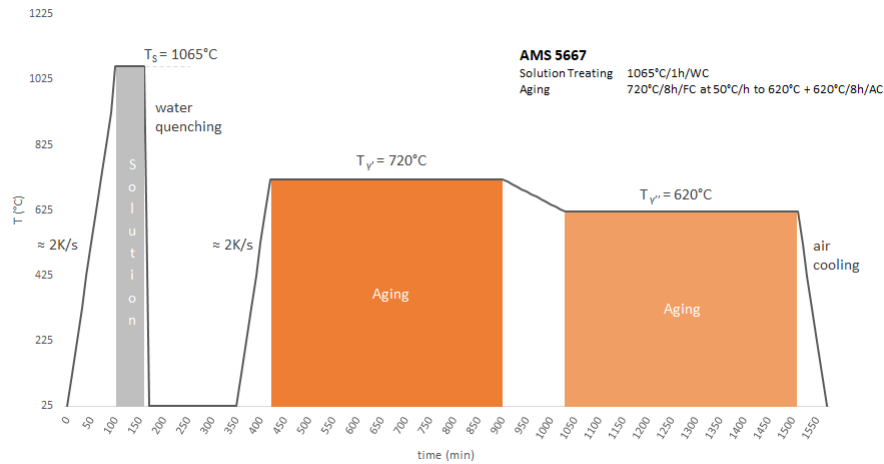


**Figure 26:** AMS5667 Heat Treatment for Inconel 718.

### 5.3 Metallographic Preparation

The samples removed by the printing platform by means of EDM then underwent the metallographic preparation. The aim of it is to highlight specimen surface features such as porosity, grain boundaries, melt pools, crack, and phases. It involves several steps:

1. Cut of the sample by means of a precision miter saw along the z-y plane (3200rpm and 0.02 mm/s);
2. Mechanical grinding from 800 grit up to 2500 grit;
3. Polishing with cloth up to 1  $\mu\text{m}$ ;
4. Final polishing with  $\text{Al}_2\text{O}_3$  suspension (0.05  $\mu\text{m}$ );
5. Chemical etching with Kalling n.2 solution (40ml HCl, 2g  $\text{CuCl}_2$ , 80ml  $\text{CH}_3\text{OH}$ ) for 15s.

The final polishing of the surface was carried out with  $\text{Al}_2\text{O}_3$  suspension.

As regards the Kalling n.2 reagent, it is a standard etching reagent adopted when it comes to Inconel 718. Despite the Ti situ-alloying, it ended up being a proper etching for the new alloy too. The contact of the reagent with the sample triggers redox reactions which corrode more or less intensively the surface depending on the chemical composition. This increases the contrast among the different characteristic features of the surface making easier the identification of grain boundaries and phases. In particular, the Kalling n.2 reagent showed to be strongly aggressive towards the Ti-rich areas, such as the core of Ti segregations.

### 5.4 Optical Microscopy

The analysis of porosity and the microstructure was carried out utilizing the optical microscope Leica DMI5000 M (*Leica Microsystems*, 2021) in **Fig.27**. It is an inverted digital research microscope provided of a manual stand and focus. This allows to carefully observe selected areas of the specimen by moving the stage with an analog spindle.

This microscope allowed the calculation of porosity percentages, particle size, and the observation of the melt pools morphology. Eventually, it lets us investigate the microstructure and the presence of phases and precipitates due to the heat treatments carried out.



**Figure 27:** Optical Microscopy Leica DMI5000 M (*Leica Microsystems* (2021)).

## 5.5 Scanning Electron Microscopy

The Scanning Electron Microscope known as SEM is one of the most diffuse microscopy techniques, widely used in research. It is mainly consisting of an electron source, electromagnetic lenses, deflection coils, and detectors.

Commonly the electron sources are either a tungsten filament, a  $\text{LaB}_6$  or  $\text{CeB}_6$  crystal, or a tungsten field emission gun. The latter owns the greatest performances because of its more collimated electron beam. Once the beam is generated, it travels through the instrument up to the lenses which condensate it and control the spot size focusing the beam over the sample. The deflection coils allow instead to scan the surface of the sample moving the beam in the desired areas.

The instrument works under vacuum ( $10^{-4}$ - $10^{-7}$  Torr for SEM,  $10^{-9}$ - $10^{-10}$  Torr for FE-SEM) to avoid the interaction of the electrons with the atmosphere. This improves the overall efficiency of the system reducing the beam dispersion.

The sample has to be conductive. If it is not conductive, the image would be affected by *charging*, namely the accumulation of static charges on the sample surface. Non-conductive materials such as polymers, most ceramics, and oxidized metals have to be coated by means of Au, Pd, Ag, or carbon to be ground with the sample holder and avoid charging.

The SEM allows obtaining topological and compositional information about microstructure, phases, cracks, porosity at a resolution of up to a few nanometers. This technology is based on two different signals - secondary electrons (SE) and back-scattered electrons (BSE). SE are ideal for topological analysis. They come from the non-elastic electrons-matter interaction in the first few nanometers of the specimen surface. BSE are instead the product of elastic electron-matter interactions in the first 100 nm below the surface. The electrons striking the surface are attracted to the positive nucleus of the atoms they pass by. This attractive force deflects them back off the surface. Therefore, the bigger the atom involved in the process, the higher the BSE signal

generated. This type of analysis increases the contrast in the image among areas with different chemical composition but without any topological information.

During this research, SEM was used to study morphology, space, and size distribution of phases and porosity inside the polished samples in all the considered conditions (as-built, ST, SDA).

### 5.5.1 Energy Dispersive Spectroscopy

The Energy Dispersive Spectroscopy, also known as EDS or EDX, is an analysis able to determine the elemental composition of a point or to map the surface distribution of elements using the scanning capabilities of the electron microscopes such as SEM or TEM.

As visible in **Fig.28**, when an electron hits the sample, if it owns enough energy it can kick an electron out of the electron shell of an atomic nucleus. The vacancy generated is then immediately filled by another electron coming from a higher energy shell through the release of energy equal to the difference in energy between the two shells involved. While the kicked electron represents a SE, the release of energy is actually a characteristic X-ray, different based on the involved element. Once generated they are picked up by a detector which transforms them into chemical composition data.

In order to generate these rays, the electrons bombarding the surface must have enough energy. This is controlled by the acceleration voltage, which has usually to be around 25 KV (Welker, 2012).

EDS was used to confirm, by chemical composition, the nature of the phases identified during the scanning electron microscopy. Despite that, the information provided by the SEM-EDS must not be considered definitive by itself. The characteristic X-rays come from a depth of roughly  $1\mu m$  so the information achieved may be influenced by phases present slightly below the surface and not visible in the previous SEM analysis.

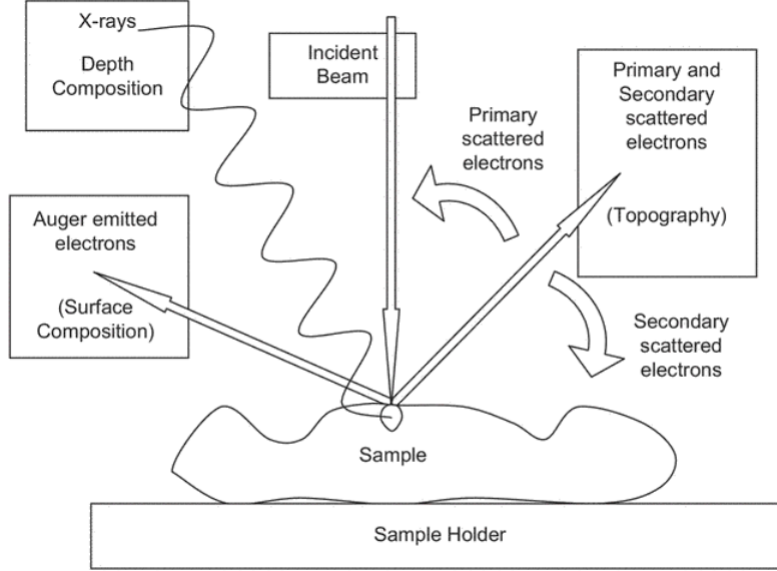


**Figure 28:** SEM-EDS Analysis (Welker (2012)).

## 5.6 ImageJ and Archimede's Density

ImageJ is a convenient digital image processing software to display, edit, analyze and modify grayscale images (8-bit, 16-bit, and 32-bit) and color type images (8-bit, 24-bit) in PNG, JPEG, GIF, BMP, DICOM, FITS, TIFF, and raw file format. It can calculate angles, distances, and create histograms based on the calculation of area and pixel value statistics of user-defined selections and intensity-thresholded objects (*National Institute of Health, 2021*). In particular, the thresholding allows to carry out the so-called *segmentation*, namely the isolation of a feature of interest from the background in order to better process it.

The possibility to modify the images is particularly convenient since it allows not to take into account defects such as residues of paste particles, filaments, or halos coming from a not proper cleaning of the samples which would otherwise affect the evaluation of the needed data.

Archimede's density is instead a useful physical method to calculate the volume and porosity of irregularly-shaped samples. Also known as *Hydrostatic Weighing*, it consists of the calculation of the porosity through physically weighing the specimens first in the "dry" ( $m_0$ ) condition and then while immersed in water ( $m_B$ ). The difference in weight provides the mass of the water displaced by the sample. According to the buoyancy principle, the volume can be calculated and consequently the density of the sample. In **eq.11** the Archimede's porosity percentage is calculated making use of the Inconel 718 as reference.

$$P\%_{Archimede} = 100 - \left( \frac{m_0}{m_0 - m_B} \right) \cdot \frac{\rho_{water}}{\rho_{IN718}} \cdot 100 \quad (11)$$

The values of porosity percentage provided by image analysis and Archimede's method are different but show similar trends.

## 5.7 Hardness Measurements

### 5.7.1 Vickers Microhardness

Microhardness measurements were carried out using a microindentation hardness indenter (LEICA VMHT-001, Walter Uhl). This tester is equipped with a four positions turret that holds one indenter position and three objective lenses having 2.5x, 10x, and 50x magnification. The hardness values achieved are reported in Vicker's microindentation hardness scale, HV. The focal position is found thanks to a focus finder once the sample is carefully held by a precision vise. The tested points are chosen randomly over the surface of the sample using analog micrometer spindles to move the specimen stage. The final hardness was the average of six evaluations for each component, two at the bottom, two in the middle, and two at the top of the polished cross-section. After choosing the indentation spot, the indenter is brought into its working position. The force (500 gf) is applied smoothly and held for the required time, usually between 10 and 15 seconds. In order to avoid influences from the previous indentations, a spacing of at least 2.5 times the average diagonal of the indentation mark is maintained between each indentation.

Vicker test indenter is a square-based pyramid whose plane faces create at the apex a 136° angle. The bidimensional mark left by the instrument should have a square-like shape. The HV hardness of the material is determined by the ratio between the force applied (Kgf) and the square-like indentation mark area (mm<sup>2</sup>).

The hardness evaluation follows the equations below:

$$A = \frac{d^2}{2\sin(136/2)} \approx \frac{d^2}{1.8544} [mm^2] \quad (12)$$

$$d = \frac{d_1 + d_2}{2} [mm] \quad (13)$$

$$HV = \frac{F}{A} \approx \frac{1.8544F}{d^2} \left[ \frac{Kgf}{mm^2} \right] \quad (14)$$

The hardness test was carried out with 500 gf and 15 s holding time. The diagonal lengths are calculated acting on the digital measuring eyepiece. The latter can be swiveled from horizontal to vertical position in order to measure both the diagonals of indentation mark by turning its lateral spindles, **Fig. 29**.



**Figure 29:** LEICA VMHT-001 Microhardness Instrument (Uhl (2020))

### 5.7.2 Brinell Hardness

The Brinell hardness can be used as microindentation technique like the Vickers. ASTM E10-15a and ISO 6506-1 explain the standard methodology for Brinell hardness for metallic materials (E10-15, 2015; STANDARD & ISO, 2006). Unlike the Vickers, Brinell has a spherical indenter made out of steel or tungsten carbides for hard materials. The size of the indentation mark left by the Brinell test is much bigger than the Vickers'. When non-homogeneous materials are tested it can be better than Vicker microhardness. Indeed, if there are precipitates with a size in the range of Vickers indentation marks (tens of  $\mu m$ ), the Vickers may provide incongruous results depending on where the indenter press the surface of the sample. The Brinell test can though decrease the standard variation of the results acting over a wider surface area.

The **eq. 15** highlights all the parameters involved in the calculation of the BHN (Brinell Hardness Number), also known as HB . It involves the applied load in kgf P, the indenter sphere diameter D, and the depression diameter d. Like in the Vickers' hardness test, the diameter calculated on the left impression is the average of two measurements perpendicular to each other. Except for the indenter, the working principles are the same as the Vickers test.

This project used an HB10 test involving a load of 62,5 kgf applied for 15 seconds by a WC-spherical indenter of 2,5 mm in size.

$$BHN = \frac{2P}{\pi D(D - \sqrt{D^2 - d^2})} \quad (15)$$

## 6 Result Discussion

The research work was divided into three jobs. The first two jobs aimed to optimize the printing parameters to get a density high enough to then proceed with the metallographic characterization. In particular, the aim was to achieve the same sample density as Inconel 718. During all the process, the latter was used as reference material since it is the most common Ni-based superalloy processed by L-PBF with high density. In the following steps, Inconel 718 will be used to help understand the effect that titanium has on the mechanical properties of the achieved specimens.

### 6.1 Job 1

For both the first and the second job the followed methodology involved the Design of Experiment (DoE). A method that allows multiple parameters manipulation and the determination of their effect on the outcome of the process.

Job1 involved the printing of 16 samples characterized by the same constant power and layer thickness but differ on hatching distance (HD), scanning speed (SS), and scanning strategy. **Table 7** shows the set parameters utilized during the first Design of Experiment.

**Table 7:** Printing Parameters Adopted for the Job 1

Sample	P (W)	SS (mm/s)	HD (mm)	Layer Thickness (mm)	Strategy	VED (J/mm <sup>3</sup> )
01	95	800	0.04	0.015	Stripe/67°	197.9
02	95	800	0.05	0.015	Stripe/67°	158.3
03	95	800	0.06	0.015	Stripe/67°	131.9
04	95	800	0.04	0.015	Island/Meander	197.9
05	95	800	0.05	0.015	Island/Meander	158.3
06	95	800	0.06	0.015	Island/Meander	131.9
07	95	700	0.04	0.015	Stripe/67°	226.2
08	95	700	0.05	0.015	Stripe/67°	180.9
09	95	700	0.06	0.015	Stripe/67°	150.8
10	95	700	0.04	0.015	Island/Meander	226.2
11	95	700	0.05	0.015	Island/Meander	180.9
12	95	700	0.06	0.015	Island/Meander	150.8
13	95	800	0.05	0.015	Stripe/67°	158.3
14	95	800	0.05	0.015	Island/Meander	158.3
15	95	800	0.05	0.015	Stripe/67°	158.3
16	95	800	0.05	0.015	Island/Meander	158.3

The values of VED were calculated thanks to equation (2), as indicated in section 2.3, which

involves power, hatching distance, layer thickness, and scanning speed. The outcomes of the printing process were 16 different cubes with 1 cm side each. The samples were labeled with an identification number printed on top in order to make easier the identification of the specimens in the following analysis, **Fig.30**.

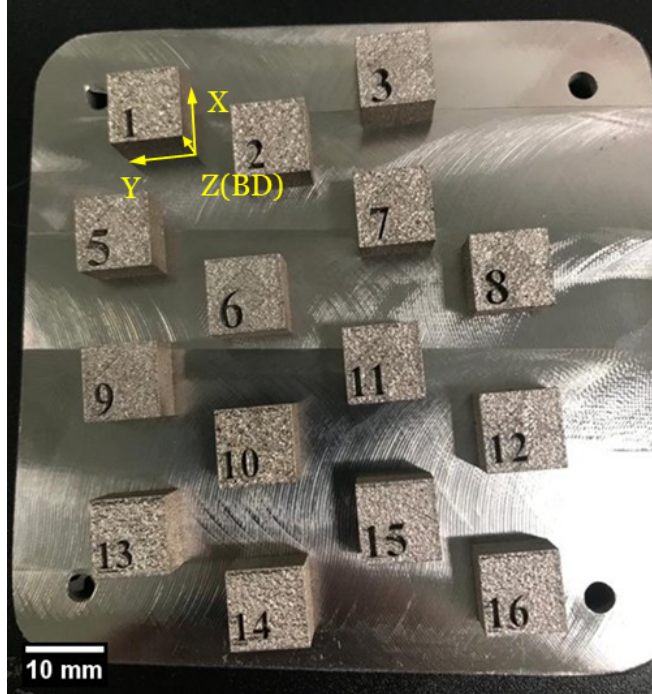


**Figure 30:** Specimens out of the L-PBF process

After being removed from the machine they underwent a stress-relieving heat treatment as standard specification ASTM F3055 recommends for powder bed fusion additively manufactured IN718. By means of electro-discharge machining (EDS), the samples were then removed from the platform making them ready for the following metallographic characterization. The sample followed the metallographic preparation described in section 5.3 with the exception of the etching step. Indeed, this job aimed only to improve the printing parameters rather than study the microstructure. The only concern was to cut every sample in the same direction (BD). Additive manufacturing produces samples whose defects can be direction-dependent, thus it is important to analyse them along the same direction.

**Table 8** shows the porosity values achieved for the 16 samples involved in Job1. The high values achieved proved that the process parameters still had to be optimized. This was something comprehensible since not having previous studies on which base the selection of the printing parameters, the process started using the ones typical of Inconel 718, the reference alloy.

Some aspects can though be noticed, such as the trend of the porosity when plotted against the Volumetric Energy Density. In **Fig. 31** the previous results are plotted and the trendline is highlighted. As you can see the values follow a parabolic trend with a minimum in  $174 \text{ J/mm}^3$ .

This value is though not characteristic since it would need many more samples in order to track a proper trend line.

Another interesting aspect is how different can be the porosity connected to the same VED value. Indeed, even though the VED is widely used in the research field as a reference parameter for porosity evaluation and parameters optimization, many times it lacks meaning. For instance, considering the VED of  $158.33 \text{ J/mm}^3$ , it produced samples characterized by porosity from 0.26% up to 5.19%. The reason why this happens is that the way power and scanning rates are combined actually matters. Despite power and scanning speed do not have the same effect on the outcome of the process, in the VED they are linearly dependent.

Despite what aforementioned, the actual trend seems to advise a reduction in porosity for lower values of VED. In particular, the two lowest values achieved were coming from samples 09 and 15 with a porosity of 0.31% and 0.26%, respectively.

**Table 8:** Porosity Percentage Values First DoE

Sample	VED ( $\text{J/mm}^3$ )	Porosity (%)
01	197.9	7.1
02	158.3	5.2
03	131.9	1.7
04	197.9	4.5
05	158.3	5.1
06	131.9	1.7
07	226.2	5.6
08	180.9	1.4
09	150.8	0.3
10	226.2	6.1
11	180.9	4.9
12	150.8	4.7
13	158.3	2.3
14	158.3	4.8
15	158.3	0.3
16	158.3	3.8

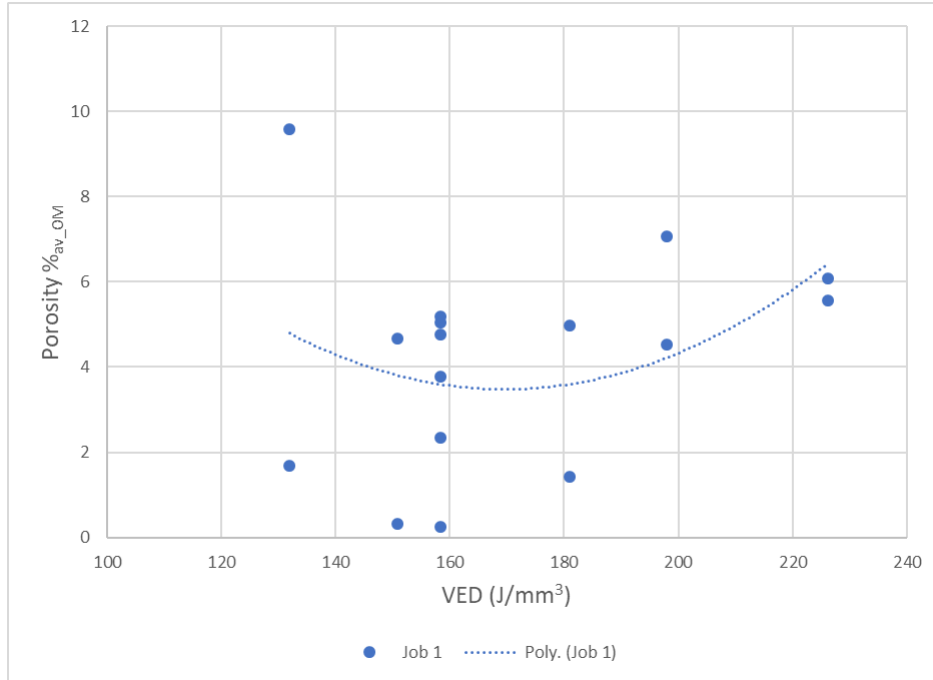


Figure 31: Porosity vs VED Referred to Job 1

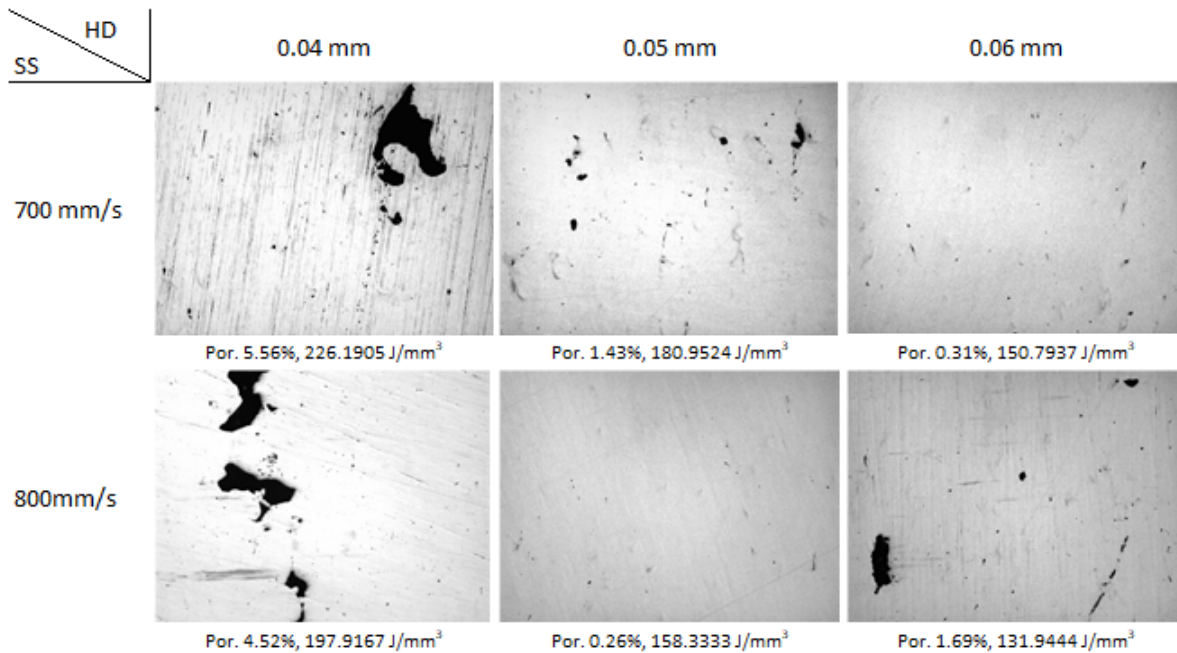
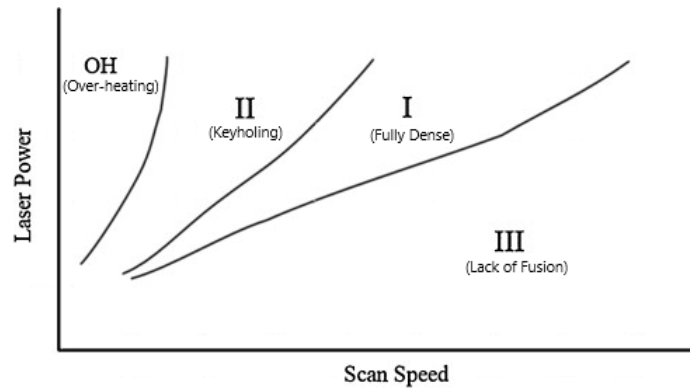


Figure 32: Sample Cross-Sections with Scanning Parameters 95 W, 0.015 mm Respectively Power and Layer Thickness. OM Porosity and VED Are Shown Below Each Picture. Sample 07, 08, 09 at the Top; Samples 04, 15, 06 at the Bottom.

Based on the cross-examination of **Fig.31** and the optical microscopy images of **Fig.32**, it was decided to work on lower VED values in the following job.

In particular, **Fig.32** provides many hints on the effects which the previously adopted parameters had on the system. Looking at the picture on the bottom-right side it is possible to see porosities of different shapes, spherical or irregular. The latter are no longer present when looking at images referring to slightly higher energy densities. This could mean that those irregular porosities are associated with lack-of-fusion (LOF) that was removed once the energy supplied to the bed increased. As far as the small spherical porosity is concerned, it is due to trapped gas coming from either the process atmosphere or already present in the powder feed. When VED of  $180 \text{ J/mm}^3$  or higher is involved, those irregular porosities seem to show up again with a higher influence, the higher the VED. Although they seem to be lack-of-fusion too, a different mechanism is the cause. As already said, not enough energy means risk of LOF, high VED a risk of keyholing, and the values in the middle lead to high-density outcomes. There is actually another possible outcome of the process when high VED are involved. This is called *over-heating* (OH) and it is highlighted in **Fig.33** which confirms what previously stated, porosity is not linearly dependent on the energy density. In the over-heating zone, excessive heating causes the generation of high strain energy that strongly increases the surface roughness. This makes difficult to properly lay down another powder layer jamming the recoating unit (Gong, Rafi, Gu, Starr, & Stucker, 2014). When the latter manages to cover the bed with another layer of powder, this is not even. Some particles will therefore undergo only partial melting during the following laser scanning, creating defects as in the image on the left-hand side of **Fig.32**.



**Figure 33:** Process window for L-PBF process. "Fully Dense" (Zone I), "Keyholing" (Zone II), "Lack of Fusion" (Zone III), and "Over-heating" (Zone OH) (Tepylo et al. (2019))

## 6.2 Job 2

The second job involved the printing of 5 cubes of the same size as the previous work. Moreover, since in the latter better results were achieved when printing with stripe-scanning strategy, all the samples of the current section underwent printing with this strategy. **Table 9** are listed all the process parameters involved in the job. The main differences with the previous one were the

increase in layer thickness from  $15\mu\text{m}$  to  $20\mu\text{m}$  and the adoption of the same scanning strategy for all the samples. As before,  $67^\circ$  indicates the hatching angle, the variation in scanning direction from one layer to the next one.

Job 2 led to an average sample density much lower than the previous job. Sample 03 represents the only exception showing a porosity of 4.1% as indicated in **Table 10** and **Fig. 34**. As visible in the images on top of **Fig.35**, both samples 03 and 04 showed evident porosity not present in the other samples. In particular, sample 02 at the bottom right shows little spherical porosity, likely due to entrapped gas by the protective atmosphere. Since the density was as high as 99.752%, it was considered enough to go ahead with the characterization work.

Not only this result allowed to continue the characterization but it confirmed that the addition of Ti did not actually affect the weldability of the alloy. This is of paramount importance when considering a new alloy to be adopted in the L-PBF process.

**Table 9:** Printing Parameters Adopted for the Job 2

Sample	P (W)	SS (mm/s)	HD (mm)	Layer Thickness (mm)	Strategy	VED (J/mm <sup>3</sup> )
01	95	800	0.04	0.02	Stripe/ $67^\circ$	148.4
02	95	800	0.05	0.02	Stripe/ $67^\circ$	118.7
03	95	700	0.04	0.02	Stripe/ $67^\circ$	169.6
04	95	700	0.05	0.02	Stripe/ $67^\circ$	135.7
09	95	800	0.05	0.02	Stripe/ $67^\circ$	118.7

**Table 10:** Porosity Percentage Values Second DoE

Sample	VED (J/mm <sup>3</sup> )	Porosity (%)
01	148.4	0.4
02	118.7	0.2
03	169.6	4.1
04	135.7	2.6
09	118.7	0.7

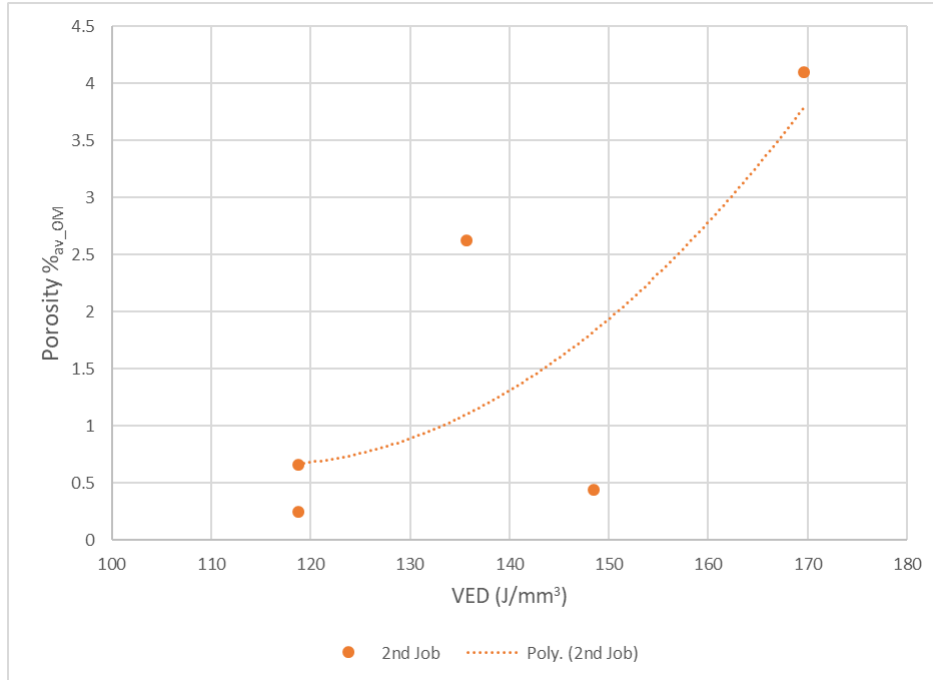


**Figure 34:** Porosity vs VED Referred to Job 2

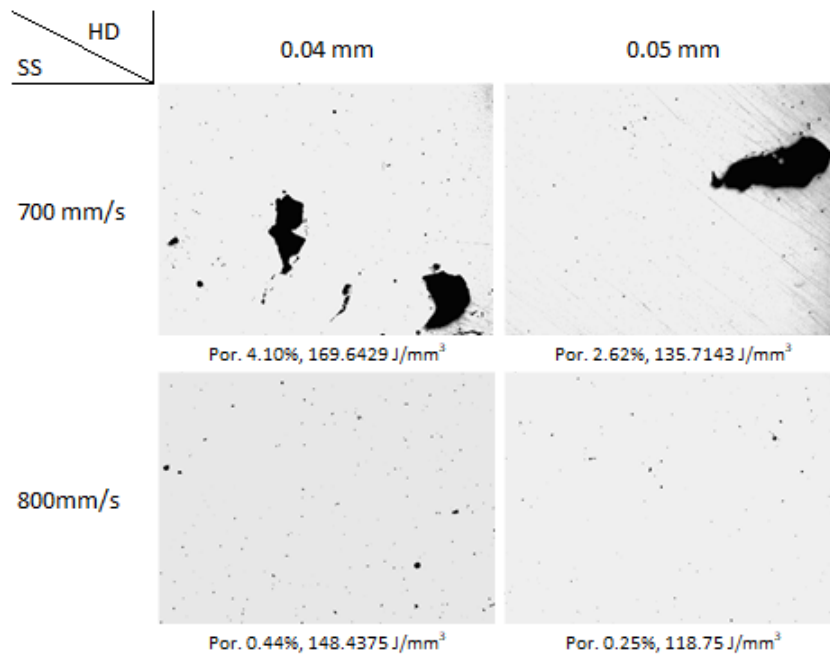


**Figure 35:** Sample Cross-Sections with Scanning Parameters 95 W, 0.02 mm Respectively Power and Layer Thickness. OM Porosity and VED Are Shown Below Each Picture. Sample 03 and 04 at the Top; Samples 01 and 02 at the Bottom.

### 6.3 Job 3

#### 6.3.1 As-Built Condition

According to the flow chart of the process in **Fig.23** section 5, once optimized the process parameters, several samples were printed to proceed with the metallographic characterization. A group of 20 cubes among which 10 of pure Inconel 718 and 10 of the situ-alloyed version (Inconel 718 + Ti powder) were built by means of the process parameters of sample 02 (Job 2) summarized in the **Table 11**.

**Table 11:** Optimized Process Parameters Adopted in Job 3

<b>Job3 Settings</b>		
Parameters		VED
P (W)	95	118.7 J/mm <sup>3</sup>
SS (mm/s)	800	
HD (mm)	0.05	
t (mm)	0.02	
Scanning Strategy:	Stripe/67°	
Processed Materials:	IN718	
	IN718+Ti	

For each category, 1 sample was left in the as-built condition, 6 were solution heat-treated, and 3 both solution heat-treated and double aged (AMS5667). This process enabled the understanding of which influence the Ti powder has on the Inconel 718 microstructure and mechanical properties.

From image analysis by ImageJ software on Inconel 718 and Inconel 718 + Ti sample cross-sections, a final density of 99.65%  $\pm$ 0.24 and 99.71%  $\pm$ 0.14 was achieved, respectively. Regarding the cross-sections of these L-PBF processed samples, they are characterized by arc-shape melt pools that formed due to the Gaussian distribution of the laser beam energy. The addition of titanium powder had only a slight effect on their size. Through image analysis by ImageJ software on the size distribution of these melt pools, highlighted in **Fig.36**, the latter were characterized by average width of 65 $\pm$ 14  $\mu$ m and 71 $\pm$ 17  $\mu$ m, and an average depth of 50 $\pm$ 10  $\mu$ m and 45 $\pm$ 9  $\mu$ m for Inconel 718 and Inconel 718 + Ti respectively. Hence, the addition of titanium caused an increase of 8.5% in the melt pool width and a reduction of 10% in the melt pool depth, referred to the reference alloy.

**Fig.36** shows an evident difference between IN718 and IN718+Ti. These images were taken by an optical microscope after polishing the surfaces and then etching for 15s with Kalling n.2 reagent. The sample printed with the situ-alloyed powder shows black spots. Since both the sample of pure Inconel 718 and the other one are printed with the same process parameters, those regions can be referred as Ti-segregations. This confirmed that the simple printing process is not

able to let the Ti diffuse properly. The fast cooling rate ( $10^6$  K/s) (Sun et al., 2017) typical of the L-PBF does not provide enough time for the Ti to diffuse into the matrix leaving areas with a high concentration of Ti. The black spots in the image are actually areas more corroded that during the optical microscopy result darker. This behaviour is comprehensible since it depends on the electrode potential of the considered element which makes it more or less noble in the galvanic series. The electrode potential of Ti is -1.63 V whereas the Ni is -0.25 V. Nb and Ti own two of the lowest electrode potential in Inconel 718. During the etching process, the element (or the area) with the lowest electrode potential (anode) undergoes the most aggressive corrosion. Therefore, titanium segregations represent regions with a high concentration of Ti and thus low electrode potential compared to the matrix rich in Ni. Thus the Ti-rich areas are more aggressively corroded and become darker during optical microscopy (Zhu, Yu, & Zhang, 2018).

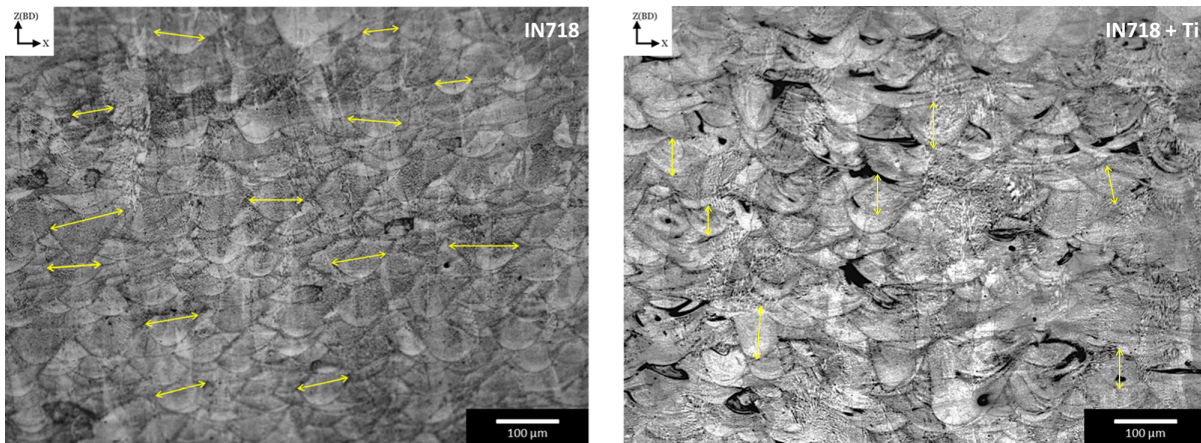


**Figure 36:** Melt Pools Comparison of Optical Microscopy Images of IN718 and IN718 + Ti Samples at Magnification 100X

A microstructure comparison is done in **Fig.38**. Being samples not heat treated (they only underwent stress-relieving treatment), they show a microstructure typical of the as-built specimens. This figure is divided into two columns - the one on the left-hand side referred to the reference Inconel 718 and the one on the right-hand side to the situ-alloyed version, both of them displayed at bigger magnification going downwards.

In **Fig.38a,b** it is visible as both the alloys show a microstructure directionally oriented towards the building direction (yellow arrows). As mentioned in the previous section, this was expected because typical of the L-PBF process. Looking at magnifications of 2000X or 5000X several features start being visible. Both the samples show the cellular/dendritic structure typical of L-PBF processed Ni-based superalloys (indicated with CS-cellular structure, DS-dendritic structure). Thanks to image analysis these structures were discovered to have an average cellular size of  $0.73 \pm 0.24 \mu m$  and a primary dendrite arm spacing of  $0.45 \pm 0.13 \mu m$ .

The images show a contrast between white regions and black ones. The latter are referred as the  $\gamma$  matrix whereas the former are identified as laves phase, some Nb-rich carbides, and probably some segregated elements. The fast cooling of each layer causes indeed directional growth as well

as microsegregation of refractory elements like Mo and Nb and the nucleation of non-equilibrium phases such as carbides or Laves inhibiting the development of strengthening phases such as  $\gamma'$  and  $\gamma''$  (Saboori et al., 2020; G. Cao et al., 2018). The macrosegregation is indeed completely prevented by the rapid cooling but this does not guarantee the lack of microsegregation. The high concentration of Nb, Mo, and C in the melt allow indeed the activation of eutectic reactions (Chlebus, Gruber, Kuźnicka, Kurzac, & Kurzynowski, 2015). The phase transformation starts at high temperatures with the nucleation of austenite ( $\gamma$ -matrix) from the liquid phase (L) according to  $L \rightarrow \gamma$ . This enriches the remaining liquid metal with Nb and C triggering the eutectic-type reaction  $L \rightarrow (\gamma + NbC)$  when the temperature drops down. The formation of these carbides reduces the concentration of C in the liquid enabling a second eutectic-type reaction  $L \rightarrow (\gamma + \text{Laves})$  (Tucho et al., 2017).

In the right-hand side column, it is though visible another detail, a roughly  $50\mu\text{m}$  Ti segregation. In **Fig.38f** can be noticed as the area close to the precipitate was characterized by much more activity than the matrix. The diffusion of the Ti caused the creation of a sort of cellular structure with a dimension of  $0.67 \pm 0.24 \mu\text{m}$ . Moreover, the bottom of the segregation semicircular shape seems to follow the contour of a melt pool.

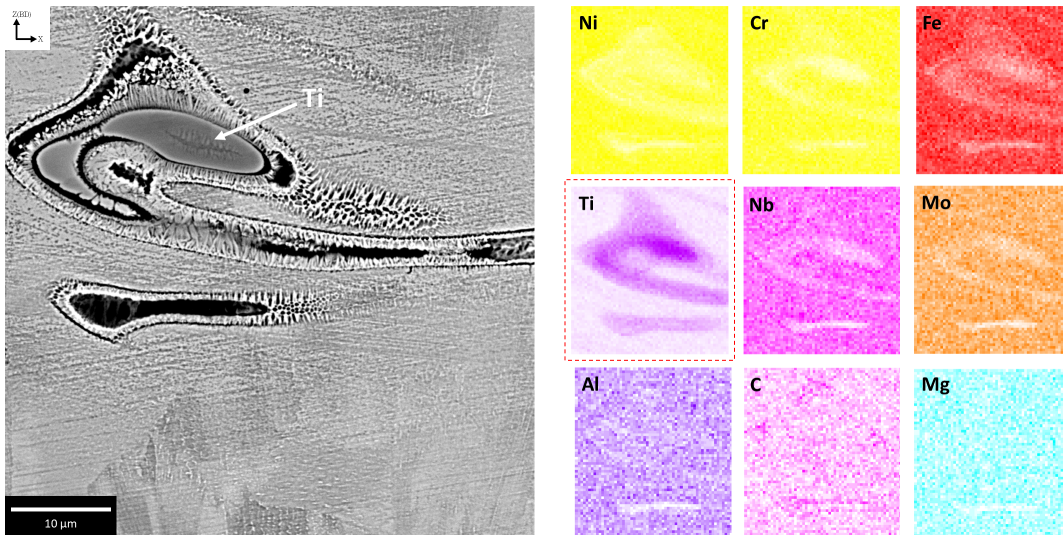


**Figure 37:** SEM-EDX Analysis of a Non-Fully Melted Titanium Particle in the As-Built Condition

In **Fig.37** a partially-melted Ti particle is magnified and analysed by EDX-mapping. It is possible to see from the dispersive analysis that the site is characterized by the presence of a core where the concentration of Ti is really high. Comparing this spot with the segregation in **Fig.38f**, it can be seen that in this case there is a net division between the area showing Ti-diffusion and the core rich in Ti. This may mean that in some cases, not only the particle of Ti is not provided with enough energy to diffuse in the Ni-matrix, but it just melts and gets deformed by the flux of liquid metal inside the molten pool. The EDX does not show the presence of other phases confirming that the fast cooling hindered their development. The only visible phase is in fact the aforementioned Laves, white spots generated in the inter-dendritic regions.

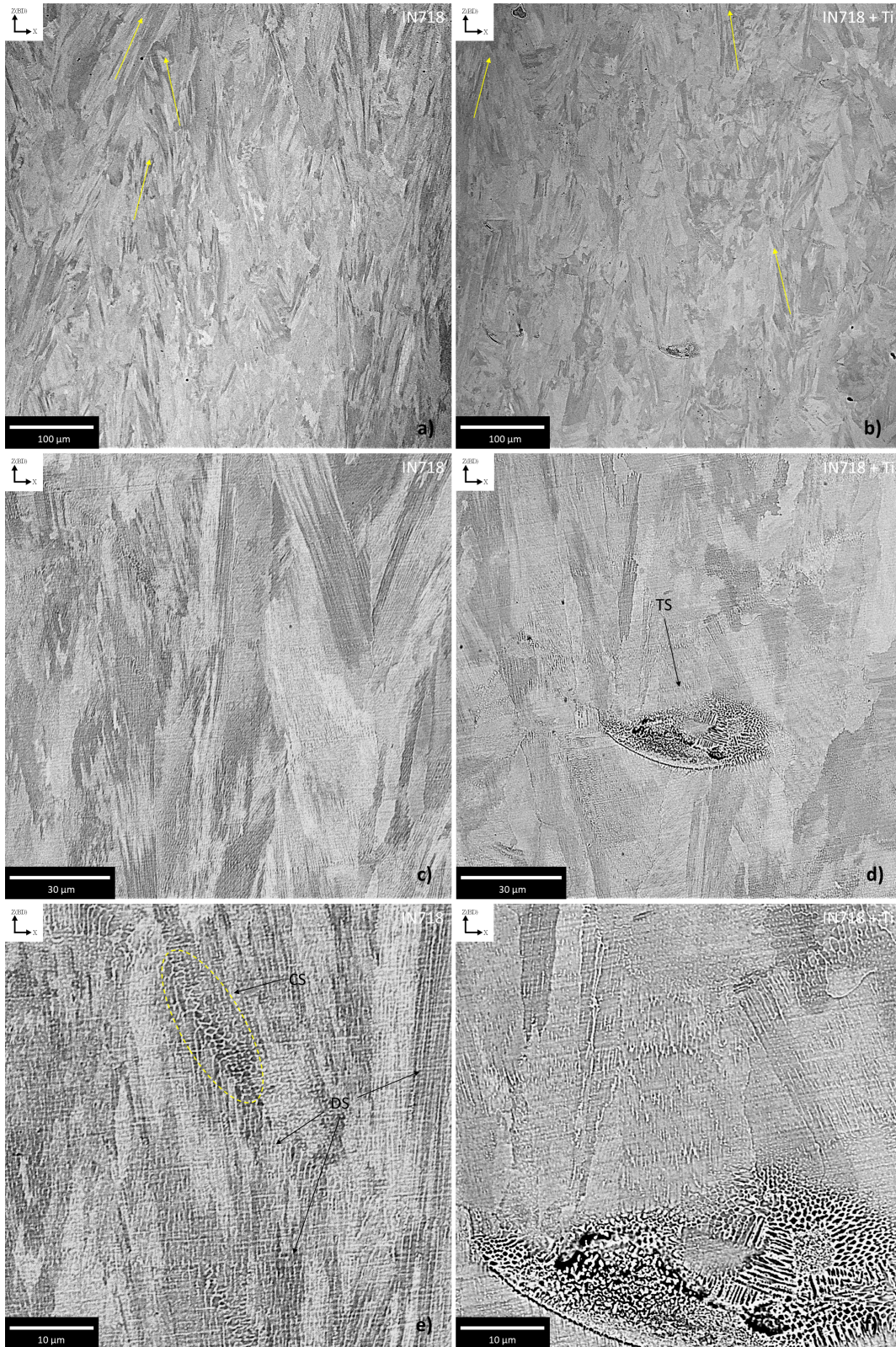


**Figure 38:** Scanning Electron Microscopy on an As-Built Microstructure of IN718 (left) and IN718+Ti (right) Samples. a),b) 500X; c),d) 2000X; e),f) 1000X. TS = Titanium Segregation, CS = Cellular Structure, DS = Dendritic Structure, Yellow Arrows = Grain Orientation

### 6.3.2 Solution Heat Treated Condition

The solution heat treatment was carried out according to **Fig.26** section 5.2 in an argon gas atmosphere. The actual aim of this process is to increase the alloy homogeneity favouring the thermal diffusion in areas with high concentration gradients. This in order to dissolve segregations and possible phases present in the material, homogenizing the chemical composition making ready the alloy to the double aging which will precipitate  $\gamma'$  and  $\gamma''$ .

At the same time, the temperature of 1080°C is high enough to start reducing the Laves phases present in the cellular/dendritic regions after the printing process, indeed no longer visible in **Fig.38e**. Despite that, Laves cannot be removed completely after 1h at 1080°C, likely still present as a small nucleus. This temperature is though already high enough to remove the microstructural features related to the layer interfaces (melt pools) improving the isotropy of the material, compared to the as-built condition. The latter phenomenon happens thanks to the activation of the recrystallization process that will further continue in the aging step (Qi, Azer, & Ritter, 2009). At the same time, the solution treatment allows the precipitation to start in the intergranular boundaries, and to reduce the dislocation density. The precipitation mainly involves carbides, since a temperature of 1080°C is higher than the  $\delta$ -solvus temperature of 1030°C (Fayed et al., 2021). Therefore, this heat treatment makes not possible the nucleation of the  $\delta$ -phase. Moreover, despite being unlikely its presence in the as-built condition, if a few  $\delta$  nuclei could instead be found in the ab-microstructure, they would melt during this step.

As visible in **Fig.40c,e** the IN718 microstructure still shows grain orientation, much more than the situ-alloyed version where it seems almost disappeared. As previously said, the solution heat treatment led to the precipitation at the grain boundary of tiny phases then proved to be Nb/Ti-rich carbides of the MC-type in **Fig.39**.

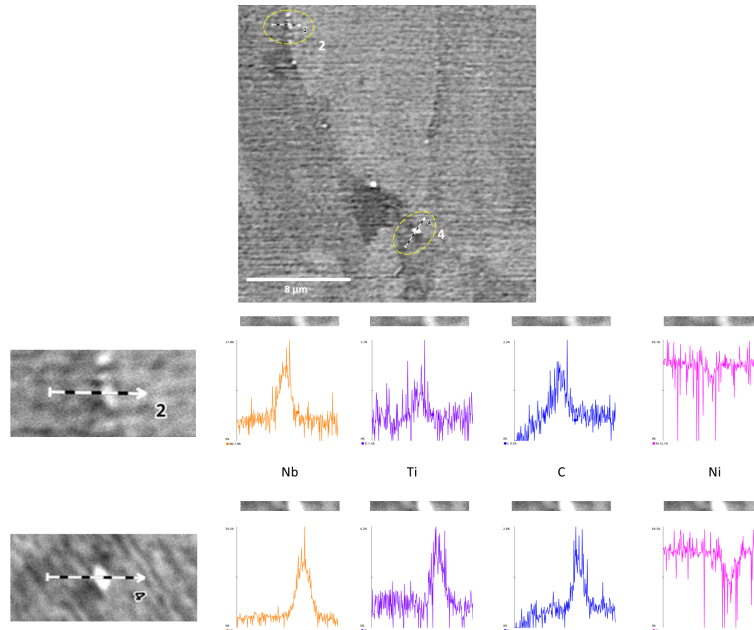


**Figure 39:** Linear EDX Scanning Electron Microscopy on Carbides Particles in a Solution Treated Microstructure of IN718, Magnification 9000X

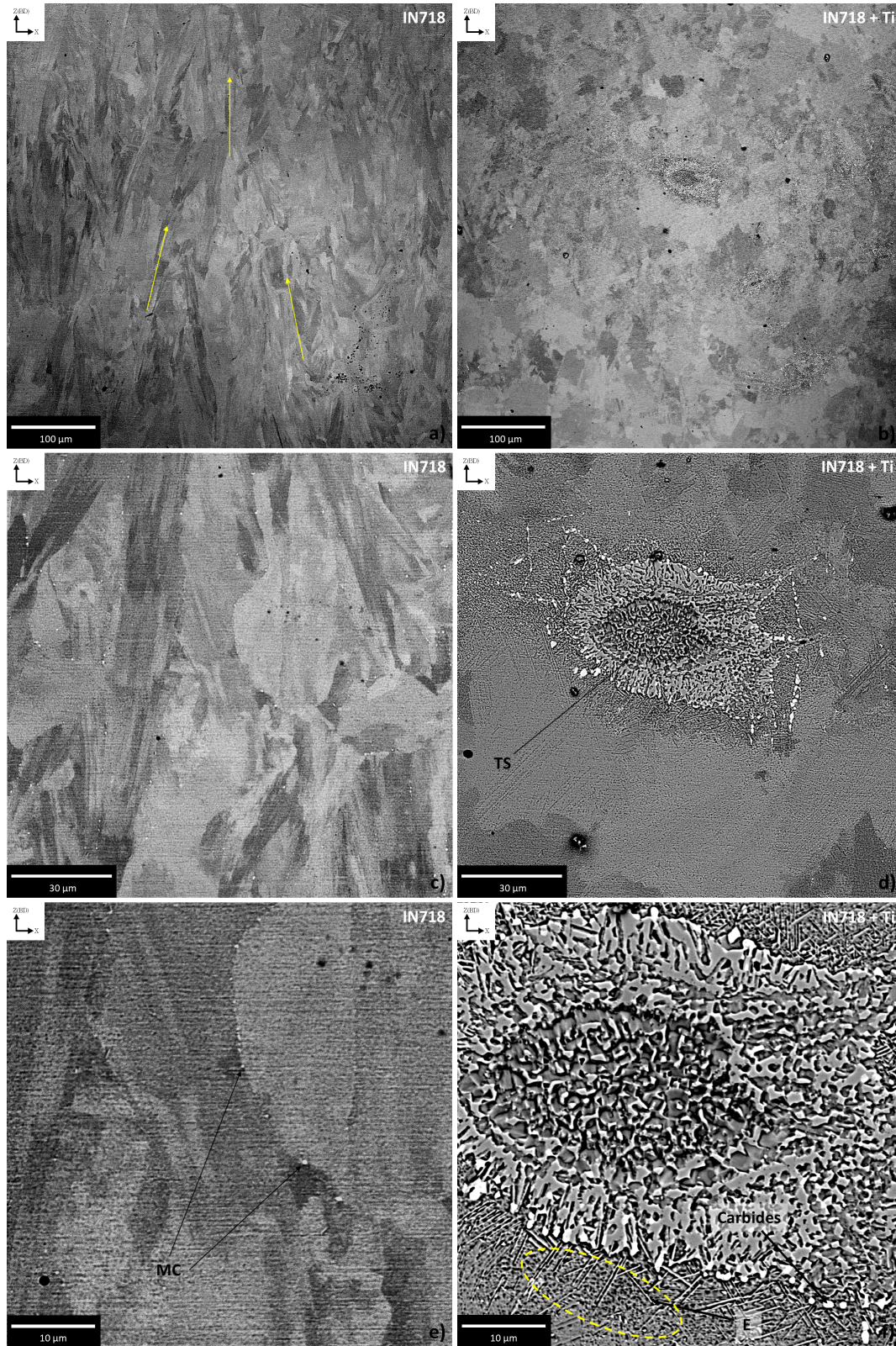


**Figure 40:** Scanning Electron Microscopy on a Solution Treated Microstructure of IN718 (left) and IN718+Ti (right) Samples. a),b) 500X; c),d) 2000X; e),f) 1000X. TS = Titanium Segregation, C = Carbides, E = Eta Phase, Yellow Arrows = Grain Orientation

Two linear-EDX were carried out on two precipitates with different sizes in the IN718 sample in order to identify the present phases. Both of these analyses showed peaks in C, Ti, and Nb in the area corresponding to the precipitates confirming that those were indeed carbides of the MC-type. **Fig.40d,f** show the presence of these phases too. Though, it can be visibly noticed how their size is on average bigger compared to the reference IN718. Moreover, while the latter shows an even distribution of these carbides, in **Fig.40b,d** is clear that IN718+Ti underwent a precipitation process mostly in the regions close to the Ti-precipitates leaving the matrix and the grain boundaries relatively free of them.

One of the most distinctive features of the situ-alloyed specimens is the presence of acicular-shape phases all around Ti-precipitates. These phases characterized by a length of roughly  $5 \mu\text{m}$  are highlighted by the yellow dashed circle in **Fig.40f**. Needle-like precipitates can be observed in both solution ST and SDAG samples. In the literature, this morphology is typically associated with mainly two phases - delta and eta phase (Antonov et al., 2015). While the chemical composition of the former is  $\text{Ni}_3\text{Nb}$  the latter is  $\text{Ni}_3\text{Ti}$ . The addition of titanium may lead to the precipitation of the latter when its concentration in the matrix exceeds saturation. However, while some researchers bond higher Ti concentrations to the presence of the  $\eta$ -phase (Wanderka et al., 2004; Antonov et al., 2015), others argue that the latter is instead due to the high concentration of Nb rather than Ti (Antonov et al., 2017). This comes from recent works reporting this phase with a chemical composition of  $\text{Ni}_3\text{Ti}_{0.5}\text{Nb}_{0.5}$  (Pickering et al., 2012).

Further analysis carried out on the microstructure allowed to achieve more shreds of evidence that could confirm that these structures may indeed be  $\eta$ -phase.

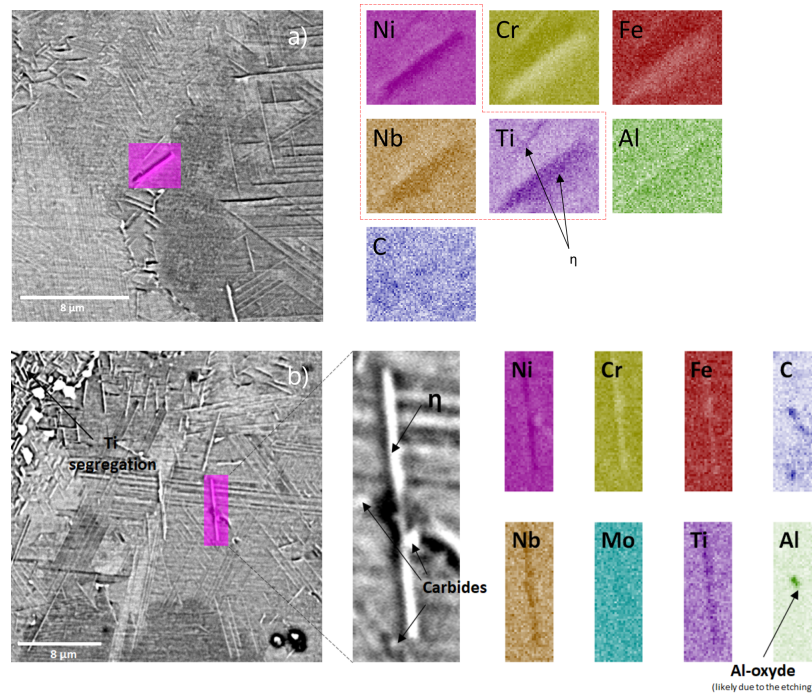


**Figure 41:** EDX Maps by Scanning Electron Microscopy of a Solution Treated Microstructure of IN718+Ti, Magnification 9000X.

From the two images in **Fig.41a,b** is possible to notice the high concentration of Ti, Ni, and Nb in the regions corresponding to the needle-like precipitate. This is expected considering the chemical composition of this phase. It has to be considered that these regions were both close to a Ti-segregation so the concentration of Ti in the surrounding matrix was already higher than 3%<sub>wt</sub>. In particular, **Fig.41b** shows the presence of tiny carbides close to the particle. The peaks of Al may stand from the formation of Al<sub>2</sub>O<sub>3</sub>, a possible product of the corrosion process brought by etching with Kalling n.2 reagent (Z. Wang et al., 2012). The possibility of these phases to be labeled as  $\eta$ -phase increases when looking at **Fig.42**. This image shows a linear-EDX carried out on a white particle in a grain boundary close to a Ti-segregation. This was done to identify the nature of these particles widely diffused around the segregation as visible in **Fig.40f**. The particle was identified to be an M<sub>6</sub>C-type carbide due to the peaks in C, Nb, and Mo. Moreover, another information can be obtained. Looking at the Ti, it can be seen as it drops down in the area corresponding to the carbide (confirming that it should not be an MC-type carbide) and it peaks at the border of it. In these areas, it can be seen an acicular-shape phase crossing the carbide. Hence, the Ti well foresees the presence of the Ti-rich particle which cannot be referred to as a carbide since the peaks do not match. This would confirm the high presence of  $\eta$ -phase in the region close to the precipitate and could justify the mismatch of mechanical behaviour from IN718 and IN718+Ti that will be described in a following section.

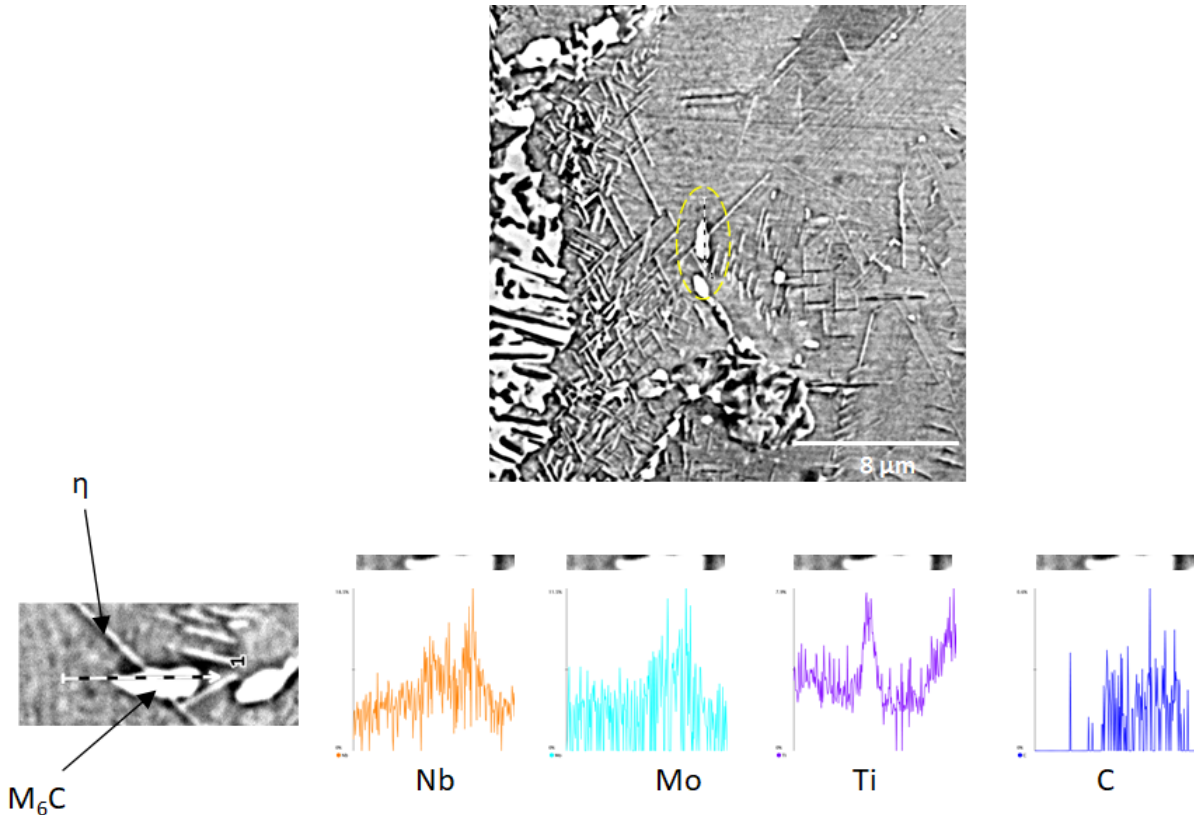


**Figure 42:** Linear EDX Scanning Electron Microscopy of a Solution Treated Microstructure of IN718+Ti, Magnification 9000X.

### 6.3.3 Double Aged Condition

The double aging heat treatment was carried out according to **Fig.26** section 5.2. This step is useful for starting to precipitate the main strengthening phases -  $\gamma'$  and  $\gamma''$ . The heat treatment involves two steps -  $720^{\circ}\text{C} \times 8\text{h}$ /furnace cooling (FC)+  $620^{\circ}\text{C} \times 8\text{h}$ /air cooling (AC). According to several authors in the literature such as Boyer and Gall,  $\gamma''$  mainly precipitates at  $720^{\circ}\text{C}$  whereas  $\gamma'$  mainly at  $620^{\circ}\text{C}$  (Boyer & Gall, 1985). Despite that, these phases cannot be observed by common SEM images because even though they are present, their size is in the nanoscale range needing further analyses by FE-SEM and TEM in order to be properly evaluated (G. Cao et al., 2018).

The first thing that can be actually noticed in the SEM images is the orientation of the grains. In **Fig.43**, it is possible to see that while the heat treatment was not enough to remove the grain orientation along the building-direction in the IN718 sample (indicated by the yellow arrows), the microstructure of IN718+Ti appears almost equiaxial. To some extent, this behaviour can be explained by the density of precipitates in the grain boundaries. As depicted by **Fig.44**, the IN718 shows a greater amount of precipitates (likely MC-type Nb-rich carbides) at the grain boundaries than IN718+Ti. The presence of secondary phases such as carbides can pin the grain boundaries reducing the grain growth in IN718 compared to IN718+Ti (Raghavan et al., 2017).

As in the solution treated condition, there is still the presence of Ti-segregations indicated in **Fig.43f** as TS. Though, compared to the only solution treated samples (ST), the segregation-size is smaller in the aged condition (SDAG), about  $42 \pm 20 \mu\text{m}$  and  $31 \pm 16 \mu\text{m}$  for ST and SDAG, respectively. The heat treatments enhance the Ti diffusion leading to a 26% reduction in the size of these segregations as highlighted in **Fig.45**. The SDAG samples, undergoing both solution heat treatment and double aging show not only fewer segregations but the size distribution curve shifts to the left towards lower sizes. This data comes from image analysis by ImageJ of the segregations through taking 3 measurements of each segregation and developing the size distribution.

As already noticed in the solution treated condition, the segregations are regions of intense activity which end up in the presence of many different phases. The double aging treatment caused a further coarsening of the acicular-shape precipitates visible in **Fig.43e,f**, and previously in **Fig.40f**.

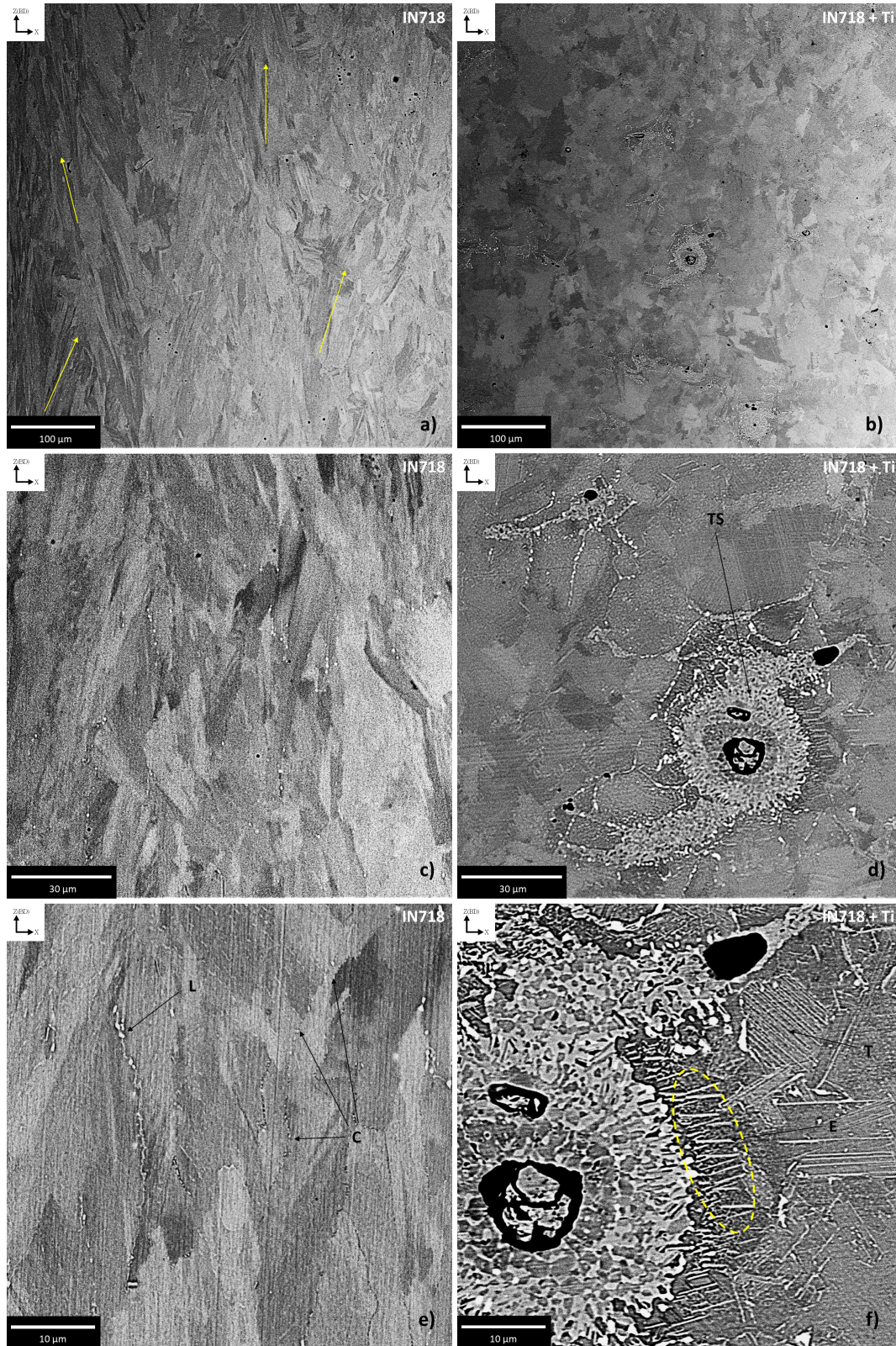


**Figure 43:** Scanning Electron Microscopy on a Solution Treated and Double Aged Microstructure of IN718 (left) and IN718+Ti (right) Samples. a),b) 500X; c),d) 2000X; e),f) 1000X. TS = Titanium Segregation, C = Carbides, E = Eta Phase, T = Annealing Twins, L = Laves Phases, Yellow Arrows = Grain Orientation

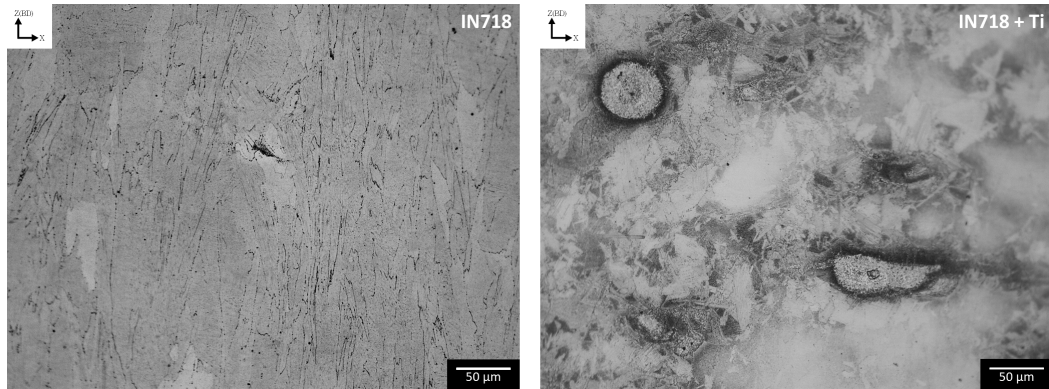


**Figure 44:** Optical Microscopy on a Solution Treated and Double Aged Microstructure of IN718 (left) and IN718+Ti (right) Samples at Magnification 200X.

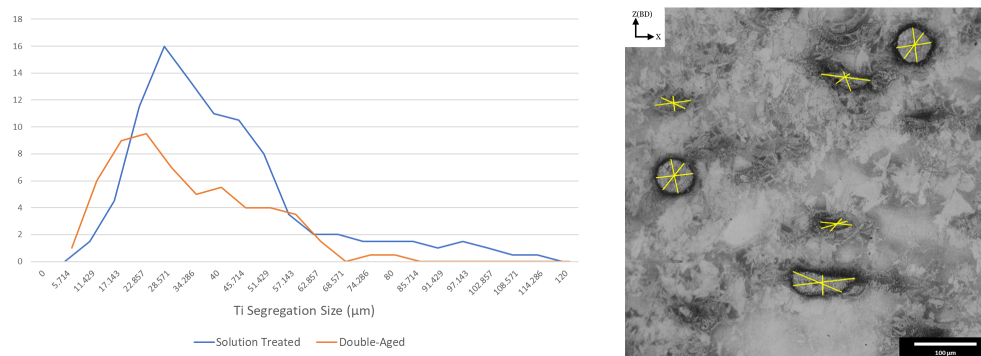


**Figure 45:** Size Distribution of Ti Segregations in IN718+Ti in Solution Treated and Solution treated+ Double Aged condition Through Image Analysis by ImageJ Software.

While the length of the acicular phases does not seem to vary much during aging, this heat treatment made them thicker than in the ST condition, **Fig.46**. This figure shows a portion of **Fig.43f**, at the border of the region richest in titanium (orange color) there are several spherical-like phases. The EDX element maps indicate they are rich in Nb and Mo. Despite this information, an area element distribution EDX alone is not enough to understand the nature of these likely carbides. In **Fig.47** there is double linear-EDX carried out over two of these precipitates. As previously stated in the ST-condition, also here the nature of these precipitates seems to be an  $M_{23}C_6$ -type carbide the former and a  $M_6C$ -type the latter. These phases are indeed rich in Nb, Mo, Cr, and C, typical of the considered families of precipitates. Looking at the image on top of **Fig.47**, it can be seen as on the left side of the considered particles, there are many tiny acicular-shape phases. Their morphology appears to look like the  $\gamma''$  one, despite this is not possible due to their size. The latter is indeed probably precipitated in the matrix as well but with a size in the range of nanometers, not detectable by simple SEM. It is likely that these phases could be indeed  $\eta$ -phase, just smaller than the previously discovered ones. These smaller versions of the phase could be nucleated later not having enough time to coarsen in the same way as previously described. Both the linear analyses show indeed peaks at the border of the analysed particles where there are

smaller likely  $\eta$ -phase, which would justify the peaks in Ti.

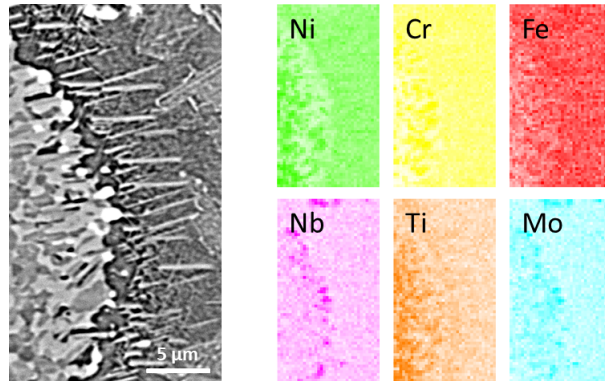


**Figure 46:** SEM-EDX analysis of a Ti-segregated area.

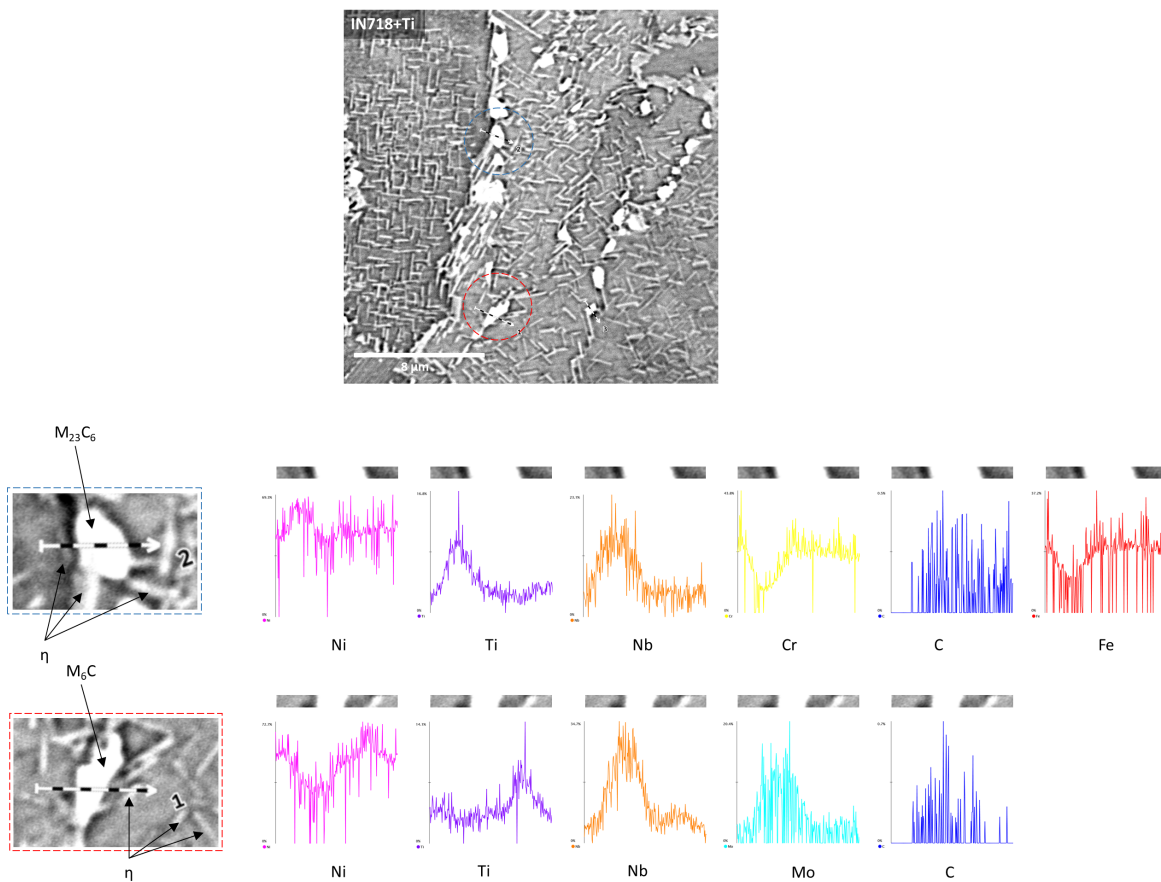


**Figure 47:** Linear SEM-EDX analysis of the Ti-segregated area in an Aged IN718+Ti at 900X magnification.

Since the limitations of the SEM machine used, further analysis should be done with more precise techniques such as FESEM, TEM, or XRD analysis in order to properly identify the involved phases, with particular attention to the acicular ones. This would allow us to better understand the impact that Ti has on the IN718 when situ-alloyed so that the additional knowledge would let the definition of proper heat treatments aiming to achieve a better chemical homogeneity in the material.

### 6.3.4 Microhardness

The microhardness test is useful to test the uniformity of mechanical properties, widely used as far as the additive manufactured samples are concerned. The microhardness values are the average of 5 measurements for each sample taken at a distance of at least 3 times the mark diameter from each other, in the (x-z) plane. In **table 12** and **Fig.48** are highlighted the average hardness values achieved by testing the samples in the different conditions - ab, ST, SDAG by means of Brinell hardness tester. The microhardness evaluation was done through both Vickers and Brinell tests. Despite that, the outcome of a Vickers microhardness test on an IN718 sample with 0.5 kgf and 15s dwelling time is a mark with characteristic diameters in the range of 40-50  $\mu m$ . This represented a problem when situ-alloyed samples were considered. The titanium segregations had a size distribution in the same range, see **Fig.45**, so the recorded value strongly depended on whether the indenter was penetrating a segregation or pure matrix. Because of that, it was decided to adopt the Brinell tester as the main hardness evaluation technique. The latter leaves indeed a mark in the range of 150  $\mu m$  when applied 62.5 kgf over a sphere-indenter of 2.5 mm in diameter. The bigger mark allows obtaining a more characteristic value taking a count of the overall material and reducing the influence of the presence of local defects on the tested surface.

It can be seen as all the samples in the SDAG condition show a greater hardness than the samples in the other conditions. This stands from the precipitation of strengthening phases  $\gamma'$  and  $\gamma''$  during the aging process. The two materials showed a hardness of  $425 \pm 5$  HB<sub>10</sub> and  $393 \pm 6$  HB<sub>10</sub>, for IN718 and IN718+Ti respectively. These values represent a gain of 44% and 31% compared to the respective ab-conditions for IN718 and IN718+Ti respectively.

As far as the solution treated condition, IN718+Ti shows a different behaviour than the reference material IN718. ST-IN718 shows a lower hardness compared to the ab-IN718. On the contrary, the situ-alloyed specimen shows an opposite trend. The lower hardness of the ST-IN718 sample is common in the literature. Due to the high gradient generated by the printing process, the L-PBF system generates in the as-built component high internal stresses which partially evolve in plastic deformation and hence dislocations. The intergranular regions, as well as the matrix of the as-built samples, are indeed characterized by high densities of entangled dislocations (Tucho et al., 2017) that contribute to increasing the hardness of the material. The solution heat treatment provides enough energy to strongly decrease their density as well as the internal strain which contributes to hardening the material too. In the common Inconel 718, these two aspects have a greater influence compared to the strengthening contribution provided by the precipitation of secondary phases at the grain boundary, leading then to a reduction in hardness (-17%).

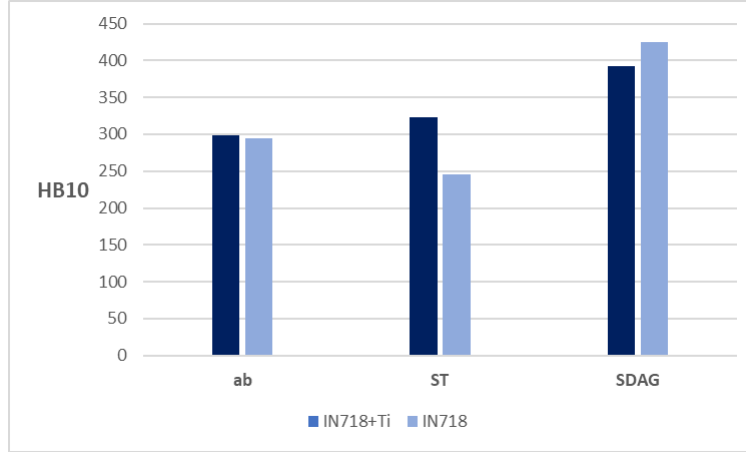


**Figure 48:** Brinell Hardness of IN718 and IN718+Ti Samples in As-Built (ab), Solution Treated (ST) and Solution Treated and Double Aged (SDAG) Condition.

**Table 12:** Brinell Microhardness Test Result of IN718+Ti and IN718 in the as-built (ab), Solution Treated (ST), Solution Treated and Double Aged (SDAG) Condition

IN718+Ti		IN718	
Condition	HB <sub>10</sub>	HB <sub>10</sub>	Condition
<b>ab</b>	299±2	295±4	<b>ab</b>
<b>ST</b>	322±3	246±2	<b>ST</b>
<b>SDAG</b>	393±6	425±5	<b>SDAG</b>

All these aspects are expected in IN718+Ti samples as well. Despite that, the outcome of the process is different. The ST-IN718+Ti shows a higher hardness than the ab-condition (+8%). This phenomenon must be due to the Ti addition. The Ti segregations introduce in the matrix highly disordered regions that together with the high chemical gradient cause the system free energy to be high. Therefore, during the solution heat treatment, the diffusion processes in those regions are likely to be favored compared to the other regions in the matrix. While during ST, IN718 undergoes intense stress relieving and reduction in dislocations density, a strong activity around the Ti-segregations in IN718+Ti leads to greater precipitation of secondary phases in these regions. Despite the stress-relieving mechanisms are active in the IN718+Ti as well, the hardness is higher than ab-IN718+Ti. This behaviour is apparently against the logic. Indeed, as visible in **Fig.43b**, the microstructure of the situ-alloyed material is characterized by a much lower anisotropy, aspect that characterizes systems in which the recrystallization process has been started leading to high stress-relieving in the material which is strongly connected with dislocation density and grain boundary surface area extension. The fact that the recrystallization was already started in the ST-IN718+Ti is confirmed by the presence in **Fig.49** of annealing twins, direct consequences of the recrystallization process. They are indeed typical of materials having face-centered cubic structures. In the latter, the stacking fault energy is low and allows the creation of annealing twins during the heat treatment.

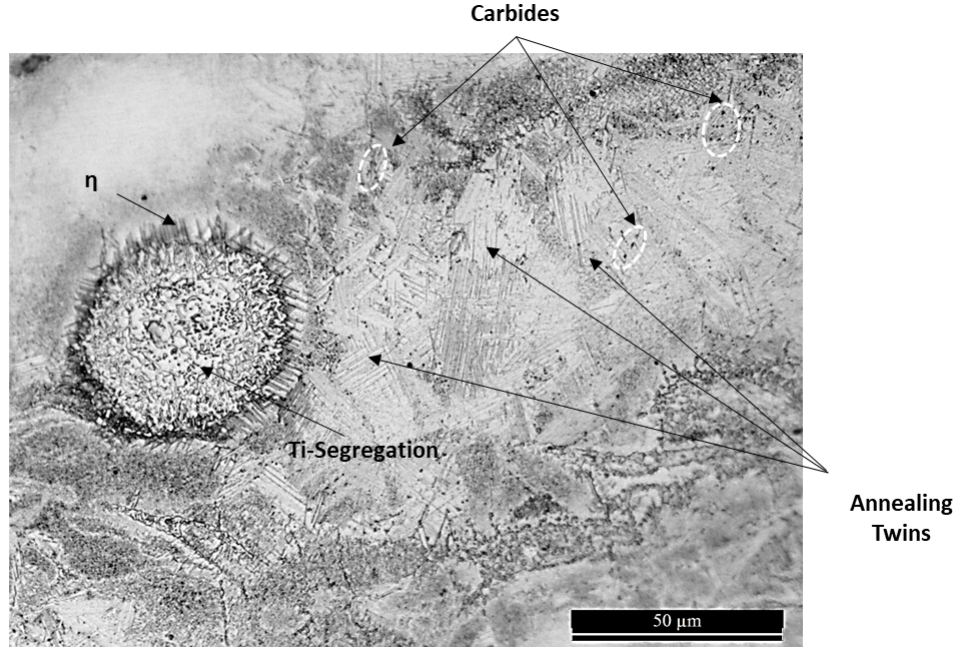


**Figure 49:** Optical Microscopy of a solution treated IN718+Ti Sample Showing the Presence of Annealing Twins and Activated Recrystallization.

Although IN718 has less anisotropy and likely bigger grains, the hardness is higher. If the acicular-shape phases were confirmed to be  $\eta$ -phase, the explanation could be sought in its behaviour. According to Jahangiri (Jahangiri, 2019), this phase can play an important role as regards the increase in mechanical properties of the alloy in which it is. In particular, according to him, the  $\eta$ -phase intrinsic hardness is  $450 \text{ kg/mm}^2$ , higher than the  $\gamma'$  one which is  $220 \text{ kg/mm}^2$ . The  $\eta$ -phase is indeed capable to increase the hardness more than the  $\gamma'$ -phase as long as the latter is not nanosized. In his studies, he worked with Inconel 939 which chemical composition is not too far from the Inconel 718 one. The former has indeed an amount of  $\gamma'$ -former elements close to the Inconel 718. Moreover, the content of titanium is roughly  $3\%_{wt}$ , higher than in Inconel 718 but close to the situ-alloyed version. The amount of Co in that alloy is also high. As discussed in the state-of-the-art, the cobalt reduces the solubility in the matrix of the  $\gamma'$ -former elements. Hence the available free-titanium in the matrix is even higher than what just indicated. This phenomenon makes this alloy behave even more like the situ-alloyed Inconel 718 discussed in this work. In particular, the high content of Ti in the IN939 can be referred to the areas close to the Ti-segregations.

In those regions, the solution treatment at  $1080^\circ\text{C}$  could provide enough energy to nucleate and grow this phase, as scientifically proved by Jahangiri and perhaps, this scientific work. The high hardness typical of the  $\eta$ -phase, and its strong precipitation close to the Ti-segregation could explain why the hardness data in IN718+Ti are higher than its as-built condition, contrary to the reference IN718. The  $\eta$ -phase was indeed not present in any as-built condition, as well as in the ST-IN718.

The fact that the  $\eta$ -phase can increase the hardness more than  $\gamma'$  only if the latter is not

nanosized, could explain the awkward behaviour recorded after aging. The aging of IN718 causes indeed the precipitation of nanosized  $\gamma'$  and  $\gamma''$ . These phases are actually expected in IN718+Ti too. Despite that, the strong presence of  $\eta$  in the latter would cause a strong depletion of available Ti and Nb for  $\gamma'$  and  $\gamma''$  precipitation. Indeed, **Fig.41** shows that this phase, whether it is actual  $\eta$ -phase or not, it removes lots of available Nb and Ti from the matrix. At the same time, as discovered during the microstructural characterization, IN718+Ti has bigger Nb-rich precipitates which remove even more Nb from the matrix. Thus, an over-aged  $\eta$ -phase, lower amount of  $\gamma'$  and  $\gamma''$  would therefore lead to a lower hardness (-7.5%) if compared to the reference material Inconel 718.

**Table 13:** Common Microhardness Values for Cast, Wrought, L-PBF, EBM, and L-DED Processed Inconel 718

Vickers Microhardness					
	Cast	Wrought	L-PBF	EBM	L-DED
As-built					T 298 [11,12,13]
			331-368 [1,2,3]	428 [2,5,6]	M 381 [12]
					B 385 [12]
ST			310 [3]	210 [7]	200-210 [11]
SDAG	370 [8]	390-401 [9,10]	470 [4]	472 [5]	438 [12]
[1]	(Jia & Gu, 2014)				
[2]	(Deng, 2018)				
[3]	(Calandri et al., 2018)				
[4]	(Z. Wang et al., 2012)				
[5]	(Deng, Moverare, Peng, & Söderberg, 2017)				
[6]	(Al-Juboori, Niendorf, & Brenne, 2018)				
[7]	(Goel, Zaninelli, Gårdstam, Klement, & Joshi, 2021)				
[8]	<i>(Inconel Alloy 718, 2007)</i>				
[9]	<i>(Alloy 718, 2021)</i>				
[10]	(Malara & Radavich, 2005)				
[11]	(Liu, Lyu, Liu, Lin, & Huang, 2020)				
[12]	(Z. Li et al., 2020)				
[13]	(Ma, Wang, & Zeng, 2015)				

T = Top, M = Middle, B = Bottom

Eventually, in **Table 13** are listed the data available in literature concerning several manu-

facturing techniques, such as either wrought Inconel 718 or cast, L-PBF, EBM or L-DED (Laser Direct Energy Deposition) Inconel 718.

By a comparison of the value achieved during this investigation and the ones from literature, it can be seen as ab-Inconel 718 hardness of 337,1 HV falls within the provided range in **Table 13** for as-built Inconel 718. According to the references, the ideal value for fully-dense Inconel 718 by L-PBF would be 395.8 HV (Jia & Gu, 2014). The lower values are therefore likely caused by the value of porosity which affects the final hardness of the samples. Despite not being as high as in the fully dense condition, the ab-IN718+Ti got a higher value of 354.6 HV. As previously explained, this is likely due to the presence of the needle-like secondary phases which may have increased the evaluated hardness. As for the other AM techniques, it can be seen as, by and large, they over-perform the outcomes of the L-PBF process. The former are though characterized by the precipitation of strengthening phases already in early stages. The higher energy provided to the system during EBM and L-DED allows the precipitation to begin during the printing step. Therefore, the as-built material already shows higher densities of precipitates hampering dislocations movement and consequently increasing material hardness. Despite that, the provided energy can differ from the bottom to the top of the printed specimen. Different amounts of energy cause the strengthening mechanisms to vary in the space and thus to show different hardness values depending on how much  $\gamma'$  and  $\gamma''$  managed to precipitate in a certain area. The mismatch among those technologies actually becomes much narrower after aging heat-treatment. Indeed, the process allows L-PBF specimens to precipitate the strengthening phases so that, they reach almost the same mechanical performances as the former. However, during this work, SDAG-IN718+Ti actually reached 451.2 HV, still much lower than what was expected by being an IN718 derivate. Even though this value is lower than 470 HV, commonly associated in the literature to SDAG-IN718, it is still higher than what typical in laser direct energy deposition processed samples. It is worth noticing, that this value could strongly change once solved the homogeneity downsides linked to the *situ-alloying* process. In fact, the pre-alloyed SDAG-IN718 displayed a hardness of 483.5 HV, 3% higher than what was foreseen by the literature review. Moreover, this demonstrates the reliability of the process parameters adopted.

The conventional processes are instead characterized by a different microstructure that affects their mechanical properties. In particular, it is undeniable that solution treated and aged cast-IN718 is not able to achieve hardness values comparable to the ones typical of the as-printed AM samples. This comes from the coarser microstructure. Lower cooling rates cause the grain size distribution to shift towards higher sizes causing a reduction in hardness. This condition is though to some extent recovered by means of work hardening. Billets and beams of cast-IN718 can in this way take advantage of the recrystallization process to decrease the average grain size gaining higher mechanical properties, and higher hardness. Despite the fine microstructure owned by AM-processed specimens, their mechanical properties before the aging phase are indeed worse than in wrought-IN718. In the latter, good control of the work hardening process can in fact lead to values in the range of 390-401 HV, comparable to what can be obtained with the most modern AM technologies.

## 7 Conclusion

### 7.1 Results and Highlights

The results of this thesis highlight the feasibility of *in-situ* alloying as a route to carry out alloy modification on Inconel 718 despite proving the need for further studies. The process managed to provide almost full dense samples, comparable to the typical values achievable by 3D-printing pure Inconel 718. Although, the process parameters needed to be optimized. The intrinsic inhomogeneity of a blend of powder proved indeed to play a role as regards the laser-material interaction so that the common Inconel 718 process parameters led to the generation of a high level of porosity.

As expected, an almost fully dense sample does not necessarily mean a lack of microstructural inhomogeneity. The presence of Ti-powder caused the generation of numerous segregations, areas characterized by high chemical gradients. This is one of the main drawbacks of *in-situ* alloying when compared to the pre-alloyed condition. It was possible to see that the activation of the diffusion processes brought by the heat treatments led to a reduction in the size of 26% from the solution treated condition to the aged one. However, the average segregation size remained at  $31\mu\text{m}$  causing inhomogeneity.

In these regions of increased disorder, the diffusion processes were favored by the heat treatments leading to more intense development of secondary phases, such as carbides. A phenomenon that had several consequences in the microstructure and mechanical performances of the new alloy. First, the increased precipitation of mainly Nb-rich carbides in these Ti-rich regions actually hindered an even precipitation of carbides to the grain boundaries, instead common in the reference material IN718. Therefore, while the applied heat treatments are not able to remove the grain orientation in IN718, the lack of pinning action on the grain boundaries in IN718+Ti led to complete removal of grain orientation after aging. Second, the hardness test showed an awkward behaviour as regards the *in-situ* alloyed IN718. According to the literature, an increase in Ti in the chemical composition should be linked to a greater amount of  $\gamma'$ -phase and hence higher hardness. Contrarily, after aging, the hardness of IN718+Ti was lower than the IN718 one. Combining microstructural analysis and literature review, it was possible to link the mismatch in the mechanical answer to the generation after solution heat treatment of (Nb, Ti)-rich micrometric acicular phases, uncommon in conventional IN718. Despite the need for deeper investigation with more precise technologies, this acicular/needle-like phase is thought to be  $\eta$ -phase. Indeed, being rich in Nb and Ti it decreases the concentration of the strengthening phases former-elements leading to a reduction in  $\gamma'$  and  $\gamma''$  precipitation. The formation of this phase would explain the peak in hardness in the solution treated (ST) condition. Whereas its overaging, supported by the decrease strengthening would explain the 7.5% lower hardness in the aged (SDAG) condition compared to the reference IN718.

The development of the  $\eta$ -phase and its consequences on the  $\gamma'$  phase show that the addition of Ti-powder to the IN718 failed as regards the goal of creating a stronger alloy. It highlights indeed the need for further studies to reduce the inhomogeneity which is the source of the problem. It is likely indeed, that with a proper homogenisation heat treatment at higher temperatures for longer times, the chemical composition of the alloy prior to aging would probably lead to higher contents of  $\gamma'$  succeeding in the intent. However, the possibility to achieve an almost completely dense material seemingly without greater difficulties than traditional IN718 suggests the good chances

of implementing *in-situ* alloying as a faster and cost-effective way to produce the desired alloy composition on a small-batch scale.

## 7.2 Future Works

To complete the microstructural characterization would be interesting to carry out more analysis by transmission electron microscopy (TEM), and electron backscatter diffraction analysis (EBSD). In particular, a combination of these two analysis techniques would allow the complete identification of the likely  $\eta$ -phase.

In order to make the *in-situ* alloying fully reliable and a cost-effective alternative to conventional pre-alloying, the process needs to be fully characterized. In order to achieve an homogeneity as close as possible to the ideal condition of pre-alloyed powder, it would be necessary to study a bespoke series of heat treatments able to completely dissolve the Ti-segregations. This should be done before aging through a homogenization heat treatment. It is known that the homogeneity after aging is directly linked to the degree of element distribution achieved during the homogenization step.

Moreover, a study on the relationship between Ti-powder size distribution and the degree of inhomogeneity after heat treatments could help to identify the proper process-feed powder to choose to achieve pre-alloyed-like outcomes. The combination of this point with the previous one could provide a solution as regards the homogeneity problem so realizing the "*in-situ* alloying" full potential.

Eventually, it could be interesting to process the same powder both in L-PBF and EBM. The latter indeed is characterized by higher processing temperature which could reduce the extension of the Ti segregations. Investigations on the process-microstructure-properties relationship would allow to extend this study to the EBM technology, which is like the L-PBF widely used as regards metals 3D-printing.



## References

- Al-Juboori, L. A., Niendorf, T., & Brenne, F. (2018). On the tensile properties of inconel 718 fabricated by ebm for as-built and heat-treated components. *Metallurgical and Materials Transactions B*, 49(6), 2969–2974.
- Alloy 718. (2021). Retrieved from [shorturl.at/gmuQ4](http://shorturl.at/gmuQ4) (Accessed March 1, 2021)
- Amato, K., Gaytan, S., Murr, L. E., Martinez, E., Shindo, P., Hernandez, J., ... Medina, F. (2012). Microstructures and mechanical behavior of inconel 718 fabricated by selective laser melting. *Acta Materialia*, 60(5), 2229–2239.
- Antero, J. (2018). *Designing for additive manufacturing* (Unpublished doctoral dissertation). Politecnico di Torino.
- Antonov, S., Detrois, M., Helmink, R. C., & Tin, S. (2015). Precipitate phase stability and compositional dependence on alloying additions in  $\gamma$ - $\gamma'$ - $\delta$ - $\eta$  ni-base superalloys. *Journal of Alloys and Compounds*, 626(76–86), 215–220.
- Antonov, S., Huo, J., Feng, Q., Isheim, D., Seidman, D. N., Helmink, R. C., ... Tin, S. (2017).  $\sigma$  and  $\eta$  phase formation in advanced polycrystalline ni-base superalloys. *Materials Science and Engineering: A*, 687, 232–240.
- ATI. (2013). *Ati718plus alloy, precipitation hardened nickel-base superalloy*. Retrieved from [shorturl.at/boAD9](http://shorturl.at/boAD9) (Allegheny Technologies Incorporated Technical Data Sheet, Accessed October 26, 2020)
- Attallah, M. M., Jennings, R., Wang, X., & Carter, L. N. (2016). Additive manufacturing of ni-based superalloys: The outstanding issues. *MRS Bulletin*, 41(10), 758.
- Attaran, M. (2017). The rise of 3-d printing: The advantages of additive manufacturing over traditional manufacturing. *Business Horizons*, 60(5), 677–688.
- Azadian, S., Wei, L.-Y., & Warren, R. (2004). Delta phase precipitation in inconel 718. *Materials characterization*, 53(1), 7–16.
- Bean, G. E., Witkin, D. B., McLouth, T. D., Patel, D. N., & Zaldivar, R. J. (2018). Effect of laser focus shift on surface quality and density of inconel 718 parts produced via selective laser melting. *Additive Manufacturing*, 22, 207–215.
- Bean, G. E., Witkin, D. B., McLouth, T. D., & Zaldivar, R. J. (2020). Process gas influence on microstructure and mechanical behavior of inconel 718 fabricated via selective laser melting. *Progress in Additive Manufacturing*, 1–13.
- Bensoussan, H. (2016). The history of 3d printing: 3d printing technologies from the 80s to today. *Blog post. Sculpteo. Np*, 14.
- Bergner, M., Rösler, J., Gehrmann, B., & Klöwer, J. (2018). Effect of heat treatment on microstructure and mechanical properties of vdm alloy 780 premium. In *Proceedings of the 9th international symposium on superalloy 718 & derivatives: Energy, aerospace, and industrial applications* (pp. 489–499).
- Bourell, D., Kruth, J. P., Leu, M., Levy, G., Rosen, D., Beese, A. M., & Clare, A. (2017). Materials for additive manufacturing. *CIRP Annals*, 66(2), 659–681.
- Boyer, H., & Gall, T. L. (1985). Metals handbook, desk ed. *American Society for Metals, Metals Park, OH*, 4–20.
- Calandri, M., Manfredi, D., Calignano, F., Ambrosio, E. P., Biamino, S., Lupoi, R., & Ugues, D. (2018). Solution treatment study of inconel 718 produced by slm additive technique in view of the oxidation resistance. *Advanced Engineering Materials*, 20(11), 1800351.
- Calignano, F. (2014). Design optimization of supports for overhanging structures in aluminum and titanium alloys by selective laser melting. *Materials & Design*, 64, 203–213.

- Cao, G., Sun, T., Wang, C., Li, X., Liu, M., Zhang, Z., ... others (2018). Investigations of  $\gamma'$ ,  $\gamma''$  and  $\delta$  precipitates in heat-treated inconel 718 alloy fabricated by selective laser melting. *Materials Characterization*, 136, 398–406.
- Cao, W.-D., Kennedy, R. L., Antony, M. M., & Smythe, J. W. (2013, March 12). *Nickel-base alloys and articles made therefrom*. Google Patents. (US Patent 8,394,210)
- Carter, L. N., Attallah, M. M., & Reed, R. C. (2012). Laser powder bed fabrication of nickel-base superalloys: influence of parameters; characterisation, quantification and mitigation of cracking. *Superalloys, 2012*, 577–586.
- Catchpole-Smith, S., Aboulkhair, N., Parry, L., Tuck, C., Ashcroft, I., & Clare, A. (2017). Fractal scan strategies for selective laser melting of ‘unweldable’ nickel superalloys. *Additive Manufacturing*, 15, 113–122.
- Chakravorty, D. (2020). Stl file format (3d printing)—simply explained, 2019. URL: <https://all3dp.com/what-is-stl-file-format-extension-3d-printing/#pointthree>.
- Chlebus, E., Gruber, K., Kuźnicka, B., Kurzac, J., & Kurzynowski, T. (2015). Effect of heat treatment on the microstructure and mechanical properties of inconel 718 processed by selective laser melting. *Materials Science and Engineering: A*, 639, 647–655.
- Concept laser gmbh. (2021). Retrieved from [shorturl.at/hpuLS](http://shorturl.at/hpuLS) (Concept Laser GmbH Website, GE Additive Machines, Accessed January 17, 2021)
- Conner, B. P., Manogharan, G. P., Martof, A. N., Rodomsky, L. M., Rodomsky, C. M., Jordan, D. C., & Limperos, J. W. (2014). Making sense of 3-d printing: Creating a map of additive manufacturing products and services. *Additive Manufacturing*, 1, 64–76.
- Davis, J. R., et al. (2000). *Nickel, cobalt, and their alloys*. ASM international.
- Deng, D. (2018). *Additively manufactured inconel 718: Microstructures and mechanical properties* (Vol. 1798). Linköping University Electronic Press.
- Deng, D., Moverare, J., Peng, R. L., & Söderberg, H. (2017). Microstructure and anisotropic mechanical properties of ebm manufactured inconel 718 and effects of post heat treatments. *Materials Science and Engineering: A*, 693, 151–163.
- Deng, D., Peng, R. L., Brodin, H., & Moverare, J. (2018). Microstructure and mechanical properties of inconel 718 produced by selective laser melting: Sample orientation dependence and effects of post heat treatments. *Materials Science and Engineering: A*, 713, 294–306.
- Donachie, M. J., & Donachie, S. J. (2002). *Superalloys: a technical guide*. ASM international.
- E10-15, A. (2015). *Standard test method for brinell hardness of metallic materials*. American Society for Testing and Materials (ASTM) Philadelphia, USA.
- Eiselstein, H. L. (1962, July 24). *Age-hardenable nickel alloy*. Google Patents. (US Patent 3,046,108)
- Fayed, E. M., Saadati, M., Shahriari, D., Brailovski, V., Jahazi, M., & Medraj, M. (2021). Effect of homogenization and solution treatments time on the elevated-temperature mechanical behavior of inconel 718 fabricated by laser powder bed fusion. *Scientific Reports*, 11(1), 1–17.
- Fedorova, T., Rösler, J., Joachim Klöwer, & Gehrman, B. (2014). Development of a new 718-type ni-co superalloy family for high temperature applications at 750°C. In *Matec web of conferences* (p. 01003).
- Fischer, M., Joguet, D., Robin, G., Peltier, L., & Laheurte, P. (2016). In situ elaboration of a binary ti–26nb alloy by selective laser melting of elemental titanium and niobium mixed powders. *Materials Science and Engineering: C*, 62, 852–859.
- Fu, S., Dong, J., Zhang, M., & Xie, X. (2009). Alloy design and development of inconel718 type alloy. *Materials Science and Engineering: A*, 499(1-2), 215–220.

- Gausemeier, J., Echterhoff, N., Kokoschka, M., & Wall, M. (2011). Thinking ahead the future of additive manufacturing—. *Future Applications*.
- Ghousoub, J. N., Tang, Y. T., Panwisawas, C., Németh, A., & Reed, R. C. (2020). On the influence of alloy chemistry and processing conditions on additive manufacturability of ni-based superalloys. In *Superalloys 2020* (pp. 153–162). Springer.
- Goel, S., Zaninelli, E., Gårdstam, J., Klement, U., & Joshi, S. (2021). Microstructure evolution-based design of thermal post-treatments for ebm-built alloy 718. *Journal of Materials Science*, *56*(8), 5250–5268.
- Gong, H., Rafi, K., Gu, H., Starr, T., & Stucker, B. (2014). Analysis of defect generation in ti-6al-4v parts made using powder bed fusion additive manufacturing processes. *Additive Manufacturing*, *1*, 87–98.
- Henderson, M., Arrell, D., Larsson, R., Heobel, M., & Marchant, G. (2004). Nickel based superalloy welding practices for industrial gas turbine applications. *Science and technology of welding and joining*, *9*(1), 13–21.
- Inconel alloy 718*. (2007). Retrieved from [shorturl.at/gmuQ4](http://shorturl.at/gmuQ4) (Accessed March 1, 2021)
- Jahangiri, M. (2019). Different effects of  $\gamma'$  and  $\eta$  phases on the physical and mechanical properties of superalloys. *Journal of alloys and compounds*, *802*, 535–545.
- Jhabvala, J., Boillat, E., Antignac, T., & Glardon, R. (2010). On the effect of scanning strategies in the selective laser melting process. *Virtual and physical prototyping*, *5*(2), 99–109.
- Jia, Q., & Gu, D. (2014). Selective laser melting additive manufacturing of inconel 718 superalloy parts: Densification, microstructure and properties. *Journal of Alloys and Compounds*, *585*, 713–721.
- Kantzos, C., Pauza, J., Cunningham, R., Narra, S. P., Beuth, J., & Rollett, A. (2019). An investigation of process parameter modifications on additively manufactured inconel 718 parts. *Journal of Materials Engineering and Performance*, *28*(2), 620–626.
- Keaveney, S., Shmeliov, A., Nicolosi, V., & Dowling, D. P. (2020). Investigation of process by-products during the selective laser melting of ti6al4v powder. *Additive Manufacturing*, *36*, 101514.
- Kennedy, R. (2005). Allvac® 718plus™, superalloy for the next forty years. *Superalloys*, *718*(706), 1–14.
- Khorasani, A., Gibson, I., Veetil, J. K., & Ghasemi, A. H. (2020). A review of technological improvements in laser-based powder bed fusion of metal printers. *International Journal of Advanced Manufacturing Technology*.
- Kienl, C. (2019). *Hot forging of the nickel-base superalloy ati 718plus* (Unpublished doctoral dissertation). University of Cambridge.
- King, W. E., Barth, H. D., Castillo, V. M., Gallegos, G. F., Gibbs, J. W., Hahn, D. E., ... Rubenchik, A. M. (2014). Observation of keyhole-mode laser melting in laser powder-bed fusion additive manufacturing. *Journal of Materials Processing Technology*, *214*(12), 2915–2925.
- Krakhmalev, P., Yadroitsev, I., Yadroitsava, I., & De Smidt, O. (2017). Functionalization of biomedical ti6al4v via in situ alloying by cu during laser powder bed fusion manufacturing. *Materials*, *10*(10), 1154.
- Kumar, P., Farah, J., Akram, J., Teng, C., Ginn, J., & Misra, M. (2019). Influence of laser processing parameters on porosity in inconel 718 during additive manufacturing. *The International Journal of Advanced Manufacturing Technology*, *103*(1-4), 1497–1507.
- Labs, A. (2019). *About multilayer concurrent printing mcp*. Retrieved from [shorturl.at/qIJ46](http://shorturl.at/qIJ46) (Aurora Labs website, Accessed November 07s, 2020)

- Leica microsystems.* (2021). Retrieved from [shorturl.at/lwNT7](https://shorturl.at/lwNT7) (Leica Microsystems Website, Accessed January 16, 2021)
- Leung, C. L. A., Marussi, S., Atwood, R. C., Towrie, M., Withers, P. J., & Lee, P. D. (2018). In situ x-ray imaging of defect and molten pool dynamics in laser additive manufacturing. *Nature communications*, *9*(1), 1–9.
- Li, R., Liu, J., Shi, Y., Wang, L., & Jiang, W. (2012). Balling behavior of stainless steel and nickel powder during selective laser melting process. *The International Journal of Advanced Manufacturing Technology*, *59*(9-12), 1025–1035.
- Li, S., Wei, Q., Shi, Y., Zhu, Z., & Zhang, D. (2015). Microstructure characteristics of inconel 625 superalloy manufactured by selective laser melting. *Journal of Materials Science & Technology*, *31*(9), 946–952.
- Li, X., Shi, J., Cao, G., Russell, A. M., Zhou, Z., Li, C., & Chen, G. (2019). Improved plasticity of inconel 718 superalloy fabricated by selective laser melting through a novel heat treatment process. *Materials & Design*, *180*, 107915.
- Li, Z., Chen, J., Sui, S., Zhong, C., Lu, X., & Lin, X. (2020). The microstructure evolution and tensile properties of inconel 718 fabricated by high-deposition-rate laser directed energy deposition. *Additive Manufacturing*, *31*, 100941.
- Lindstrom, A. (2020). *Remembering one of ut's great inventors.* Retrieved from [shorturl.at/giqs6](https://shorturl.at/giqs6) (The University of Texas at Austin, Accessed August 26, 2020)
- Lippold, J. C., Kiser, S. D., & DuPont, J. N. (2011). *Welding metallurgy and weldability of nickel-base alloys.* John Wiley & Sons.
- Liu, F., Lyu, F., Liu, F., Lin, X., & Huang, C. (2020). Laves phase control of inconel 718 superalloy fabricated by laser direct energy deposition via  $\delta$  aging and solution treatment. *Journal of Materials Research and Technology*, *9*(5), 9753–9765.
- Löhnert, K., & Pyczak, F. (2010). Microstructure evolution in the nickel base superalloy allvac 718plus. In *7th international symposium on superalloy 718 and derivatives* (p. 877).
- Ma, M., Wang, Z., & Zeng, X. (2015). Effect of energy input on microstructural evolution of direct laser fabricated in718 alloy. *Materials Characterization*, *106*, 420–427.
- Malara, C., & Radavich, J. (2005). Alloy 718 large ingots studies. *Superalloys*, *718*(625.706), 25.
- Marchese, G., Parizia, S., Rashidi, M., Saboori, A., Manfredi, D., Ugues, D., ... Biamino, S. (2020). The role of texturing and microstructure evolution on the tensile behavior of heat-treated inconel 625 produced via laser powder bed fusion. *Materials Science and Engineering: A*, *769*, 138500.
- Megahed, M., Mindt, H.-W., Willems, J., Dionne, P., Jacquemetton, L., Craig, J., ... Peralta, A. (2019). Lpbf right the first time—the right mix between modeling and experiments. *Integrating Materials and Manufacturing Innovation*, *8*(2), 194–216.
- Metelkova, J., Kinds, Y., Kempen, K., de Formanoir, C., Witvrouw, A., & Van Hooreweder, B. (2018). On the influence of laser defocusing in selective laser melting of 316l. *Additive Manufacturing*, *23*, 161–169.
- Mignanelli, P., Jones, N., Hardy, M., & Stone, H. (2018). On the time-temperature-transformation behavior of a new dual-superlattice nickel-based superalloy. *Metallurgical and Materials Transactions A*, *49*(3), 699–707.
- Mignanelli, P., Jones, N., Pickering, E., Messé, O., Rae, C., Hardy, M., & Stone, H. (2017). Gamma-gamma prime-gamma double prime dual-superlattice superalloys. *Scripta Materialia*, *136*, 136–140.
- National institute of health.* (2021). Retrieved from <https://imagej.nih.gov/> (National Institute of Health, Accessed January 16, 2021)
- Nguyen, Q., Luu, D., Nai, S., Zhu, Z., Chen, Z., & Wei, J. (2018). The role of powder layer

- thickness on the quality of slm printed parts. *Archives of Civil and Mechanical Engineering*, 18, 948–955.
- Oradei-Basile, A., & Radavich, J. F. (1991). A current ttt diagram for wrought alloy 718. *Superalloys, 718(625)*, 325–335.
- Ott, E., Liu, X., Andersson, J., Bi, Z., Bockenstedt, K., Dempster, I., . . . others (2018). *Proceedings of the 9th international symposium on superalloy 718 & derivatives: Energy, aerospace, and industrial applications*. Springer.
- Ou, M., Ma, Y., Ge, H., Xing, W., Zhou, Y., Zheng, S., & Liu, K. (2018). Microstructure evolution and mechanical properties of a new cast ni-base superalloy with various ti contents. *Journal of Alloys and Compounds, 735*, 193–201.
- Ou, M., Ma, Y., Xing, W., Hao, X., Chen, B., Ding, L., & Liu, K. (2019). Stress rupture properties and deformation mechanisms of k4750 alloy at the range of 650° c to 800° c. *Journal of Materials Science & Technology, 35(7)*, 1270–1277.
- Pei, W., Zhengying, W., Zhen, C., Junfeng, L., Shuzhe, Z., & Jun, D. (2017). Numerical simulation and parametric analysis of selective laser melting process of als10mg powder. *Applied Physics A, 123(8)*, 540.
- Pereira, T., Kennedy, J. V., & Potgieter, J. (2019). A comparison of traditional manufacturing vs additive manufacturing, the best method for the job. *Procedia Manufacturing, 30*, 11–18.
- Perevoshchikova, N., Rigaud, J., Sha, Y., Heilmaier, M., Finnin, B., Labelle, E., & Wu, X. (2017). Optimisation of selective laser melting parameters for the ni-based superalloy in-738 lc using doehlert’s design. *Rapid Prototyping Journal*.
- Perrut, M., Caron, P., Thomas, M., & Couret, A. (2018). High temperature materials for aerospace applications: Ni-based superalloys and  $\gamma$ -tial alloys. *Comptes Rendus Physique, 19(8)*, 657–671.
- Pickering, E., Mathur, H., Bhowmik, A., Messé, O., Barnard, J., Hardy, M., . . . Rae, C. (2012). Grain-boundary precipitation in allvac 718plus. *Acta Materialia, 60(6-7)*, 2757–2769.
- Qi, H., Azer, M., & Ritter, A. (2009). Studies of standard heat treatment effects on microstructure and mechanical properties of laser net shape manufactured inconel 718. *Metallurgical and Materials Transactions A, 40(10)*, 2410–2422.
- Radi, B., & El Hami, A. (2016). *Material forming processes: Simulation, drawing, hydroforming and additive manufacturing*. John Wiley & Sons.
- Raghavan, S., Zhang, B., Wang, P., Sun, C.-N., Nai, M. L. S., Li, T., & Wei, J. (2017). Effect of different heat treatments on the microstructure and mechanical properties in selective laser melted inconel 718 alloy. *Materials and Manufacturing Processes, 32(14)*, 1588–1595.
- Rajendran, V. R., Mamidi, K., Ravichander, B., Farhang, B., Amerinatanzi, A., & Moghaddam, N. S. (2020). Determination of residual stress for inconel 718 samples fabricated through different scanning strategies in selective laser melting. In *Behavior and mechanics of multi-functional materials ix* (Vol. 11377, p. 1137719).
- Rathee, S., Srivastava, M., Maheshwari, S., Kundra, T., & Siddiquee, A. N. (2018). *Friction based additive manufacturing technologies: Principles for building in solid state, benefits, limitations, and applications*. CRC Press.
- Rickenbacher, L., Etter, T., Hövel, S., & Wegener, K. (2013). High temperature material properties of in738lc processed by selective laser melting (slm) technology. *Rapid Prototyping Journal*.
- Rösler, J., Hentrich, T., & Gehrmann, B. (2019). On the development concept for a new 718-type superalloy with improved temperature capability. *Metals, 9(10)*, 1130.
- Saboori, A., Marchese, G., Aversa, A., Bassini, E., Mazzucato, F., Valente, A., . . . Fino, P. (2020). Effect of heat treatment on microstructural evolution of additively manufactured inconel 718 and cast alloy.

- Sae international ams.*. (2020). Retrieved from [shorturl.at/isSU1](http://shorturl.at/isSU1) (Aerospace Material Specifications, Accessed December 12, 2020)
- Schirra, J. J., Caless, R. H., & Hatala, R. W. (1991). The effect of laves phase on the mechanical properties of wrought and cast+ hip inconel 718. *Superalloys*, 718(625), 375–388.
- ScienceVio. (2018). *In situ x-ray imaging of defect and molten pool dynamics in laser additive manufacturing*. Retrieved from [shorturl.at/gmuQ4](http://shorturl.at/gmuQ4) (Accessed March 1, 2021)
- Shao, Y.-l., Xu, J., Wang, H., Zhang, Y.-w., Jia, J., Liu, J.-t., ... others (2019). Effect of ti and al on microstructure and partitioning behavior of alloying elements in ni-based powder metallurgy superalloys. *International Journal of Minerals, Metallurgy, and Materials*, 26(4), 500–506.
- Shi, X., Ma, S., Liu, C., Chen, C., Wu, Q., Chen, X., & Lu, J. (2016). Performance of high layer thickness in selective laser melting of ti6al4v. *Materials*, 9(12), 975.
- Shiple, H., McDonnell, D., Culleton, M., Coull, R., Lupoi, R., O'Donnell, G., & Trimble, D. (2018). Optimisation of process parameters to address fundamental challenges during selective laser melting of ti-6al-4v: A review. *International Journal of Machine Tools and Manufacture*, 128, 1–20.
- Shoemaker, L. E. (2005). Alloys 625 and 725: trends in properties and applications. *Superalloys*, 718(625), 409–418.
- Simonelli, M., Aboulkhair, N. T., Cohen, P., Murray, J. W., Clare, A. T., Tuck, C., & Hague, R. J. (2018). A comparison of ti-6al-4v in-situ alloying in selective laser melting using simply-mixed and satellited powder blend feedstocks. *Materials Characterization*, 143, 118–126.
- Standard, A. (2012). F2792-12a. *Standard terminology for additive manufacturing technologies ASTM International, West Conshohocken*.
- STANDARD, B., & ISO, B. (2006). Metallic materials—brinell hardness test—.
- Sun, S., Brandt, M., & Easton, M. (2017). Powder bed fusion processes: An overview. In *Laser additive manufacturing* (pp. 55–77). Elsevier.
- Systems, D. (2020). *Our story*. Retrieved from [shorturl.at/JRX68](http://shorturl.at/JRX68) (3D Systems website, Accessed August 26, 2020)
- Tang, Y. T., Ghossoub, J. N., Panwisawas, C., Collins, D. M., Amirkhanlou, S., Clark, J. W., ... Reed, R. C. (2020). The effect of heat treatment on tensile yielding response of the new superalloy abd-900am for additive manufacturing. In *Superalloys 2020* (pp. 1055–1065). Springer.
- Teplyo, N., Huang, X., & Patnaik, P. C. (2019). Laser-based additive manufacturing technologies for aerospace applications. *Advanced Engineering Materials*, 21(11), 1900617.
- Tsang, J., Kearsey, R., Au, P., Seo, D., Oppenheimer, S., & Cao, W. (2010). Effect of composition and microstructure on the fatigue and creep-fatigue behaviour of allvac 718plus alloy. *Materials at High Temperatures*, 27(1), 79–88.
- Tucho, W. M., Cuvillier, P., Sjolyst-Kverneland, A., & Hansen, V. (2017). Microstructure and hardness studies of inconel 718 manufactured by selective laser melting before and after solution heat treatment. *Materials Science and Engineering: A*, 689, 220–232.
- Tucho, W. M., & Hansen, V. (2019). Characterization of slm-fabricated inconel 718 after solid solution and precipitation hardening heat treatments. *Journal of Materials Science*, 54(1), 823–839.
- Uhl, W. (2020). *Microhardness tester vmht*. Retrieved from [shorturl.at/ipBQ2](http://shorturl.at/ipBQ2) (UHL Technische Mikroskopie GmbH, Accessed November 05, 2020)
- Uriondo, A., Esperon-Miguez, M., & Perinpanayagam, S. (2015). The present and future of additive manufacturing in the aerospace sector: A review of important aspects (edited in the

- text). *Proceedings of the Institution of Mechanical Engineers, Part G: Journal of Aerospace Engineering*, 229(11), 2132–2147.
- Vora, P., Mumtaz, K., Todd, I., & Hopkinson, N. (2015). Alsi12 in-situ alloy formation and residual stress reduction using anchorless selective laser melting. *Additive manufacturing*, 7, 12–19.
- Wanderka, N., Naundorf, V., Banhart, J., Mukherji, D., Genovesse, D. D., & Rösler, J. (2004). Microstructural characterization of inconel 706 alloy. *Surface and Interface Analysis: An International Journal devoted to the development and application of techniques for the analysis of surfaces, interfaces and thin films*, 36(5-6), 546–551.
- Wang, X., Carter, L. N., Pang, B., Attallah, M. M., & Loretto, M. H. (2017). Microstructure and yield strength of slm-fabricated cm247lc ni-superalloy. *Acta Materialia*, 128, 87–95.
- Wang, Z., Guan, K., Gao, M., Li, X., Chen, X., & Zeng, X. (2012). The microstructure and mechanical properties of deposited-in718 by selective laser melting. *Journal of alloys and compounds*, 513, 518–523.
- Welker, R. W. (2012). Size analysis and identification of particles. In *Developments in surface contamination and cleaning* (pp. 179–213). Elsevier.
- Wong, H., Dawson, K., Ravi, G., Howlett, L., Jones, R., & Sutcliffe, C. (2019). Multi-laser powder bed fusion benchmarking—initial trials with inconel 625. *The International Journal of Advanced Manufacturing Technology*, 105(7-8), 2891–2906.
- Xie, J., Ma, Y., Xing, W., Ou, M., Zhang, L., & Liu, K. (2019). Microstructure and mechanical properties of a new cast nickel-based superalloy k4750 joint produced by gas tungsten arc welding process. *Journal of Materials Science*, 54(4), 3558–3571.
- Yadroitsev, I., Krakhmalev, P., & Yadroitsava, I. (2017). Titanium alloys manufactured by in situ alloying during laser powder bed fusion. *JOM*, 69(12), 2725–2730.
- Yin, Y., Stecke, K. E., & Li, D. (2018). The evolution of production systems from industry 2.0 through industry 4.0. *International Journal of Production Research*, 56(1-2), 848–861.
- Zhu, D., Yu, L., & Zhang, R. (2018). Dissolution effects with different microstructures of inconel 718 on surface integrity in electrochemical machining. *Journal of the Electrochemical Society*, 165(16), E872.

